



## D3.3

### Position Estimation and Environment Learning

<b>Project number:</b>	101013425
<b>Project acronym:</b>	<b>REINDEER</b>
<b>Project title:</b>	REsilient INteractive applications through hyper Diversity in Energy Efficient RadioWeaves technology
<b>Project Start Date:</b>	1 <sup>st</sup> January, 2021
<b>Duration:</b>	42 months
<b>Programme:</b>	H2020-ICT-52-2020
<b>Deliverable Type:</b>	Report
<b>Reference Number:</b>	ICT-52-2020 / D3.3 / 1.0
<b>Workpackage:</b>	WP 3
<b>Due Date:</b>	31 <sup>st</sup> March, 2023
<b>Actual Submission Date:</b>	5 <sup>th</sup> June, 2023
<b>Responsible Organisation:</b>	TUGraz
<b>Editor:</b>	Thomas Wilding
<b>Dissemination Level:</b>	PU
<b>Revision:</b>	1.0
<b>Abstract:</b>	Position estimation and environment learning. Report on fundamental performance limits for positioning, algorithm design and analysis for system calibration, positioning and synchronization as well as data fusion of information from radio infrastructure. An algorithm for environment sensing and learning exploits MIMO radar to infer mirror source locations.
<b>Keywords:</b>	Positioning, calibration, synchronization, environment learning, data fusion, algorithms



The REINDEER project has received funding from the European Union's Horizon 2020 research and innovation programme under grant agreement No 101013425.

## **Editor**

Thomas Wilding (TU GRAZ)

## **Contributors (ordered according to beneficiary numbers)**

Sai Subramanyam Thoota, Unnikrishnan Kunnath Ganesan, Erik G. Larsson (LIU)

Xuhong Li, Fredrik Tufvesson (ULUND)

Joao Vieira (EAB)

Benjamin J. B. Deutschmann, Maximilian Graber, Thomas Wilding, Klaus Witrissal (TU GRAZ)

## **Internal reviewers**

Liesbet van der Perre (KUL), Thanh Tung Vu (LIU)

## **Disclaimer**

*The information in this document is provided as is, and no guarantee or warranty is given that the information is fit for any particular purpose. The content of this document reflects only the author's view – the European Commission is not responsible for any use that may be made of the information it contains. The users use the information at their sole risk and liability.*

## Executive Summary

This deliverable reports on results obtained in the course of Task 3.4 and presents a system design analysis of candidate algorithms for positioning, reciprocity calibration in distributed multiple-input multiple-output (MIMO) systems, and environment sensing. As a step towards the data fusion of multiple Contact Service Points (CSPs) we modify a graph-based channel tracking algorithm tracking. For means of system performance analysis we investigate the achievable positioning performance in terms of the Cramér-Rao lower bound (CRLB).

The results presented in this deliverable serve the goal of investigating the performance of selected algorithms that will be applicable to specific use case scenarios. The algorithms are strong candidates for deployment and implementation in the final stage of the project. The analysis in terms of the CRLB allows to find tuning points in the system design and for deployment of actual systems in realistic environments, allowing to quantify achievable performance metrics such as positioning accuracy, or for the development of optimum CSP placement strategies for target scenarios. With position-information serving as an important input to various applications, we analyze the performance of algorithms that improve the overall system robustness for communication and positioning, being able to deal with calibration and synchronization offsets that are likely to occur in deployed systems. Environment learning is shown to support the robustness aspect by estimation of environment information that can be collected and fed back into the system to overcome difficult channel conditions, such as non-line-of-sight (NLOS), or to allow exploiting the full propagation channel in parametric position-based transmissions.

The performance characterization based on simulations of each of the employed algorithms shows the feasibility of the application in realistic scenarios. The algorithms of interest are seen as capable of working with systems of varying topology or size (in terms of user equipment (UE) devices as well as CSPs), while also allowing the flexibility to adapt to environment changes from the time of deployment onward during operation. This is seen as a key ingredient to keep the system performance of the RadioWeaves (RW) infrastructure at a high level and enable to ultimately meet target requirements set in previous deliverables.

# Contents

<b>1</b>	<b>Introduction and Overview</b>	<b>3</b>
<b>2</b>	<b>System Model</b>	<b>5</b>
2.1	Multipath-based Model . . . . .	5
2.1.1	Signal Model . . . . .	5
2.1.2	CSP Subarray Model . . . . .	7
2.1.3	Summary of Parameters of Interest . . . . .	8
2.2	Calibration Model . . . . .	9
2.3	Synchronization Model . . . . .	9
<b>3</b>	<b>Fundamental Performance Limits</b>	<b>11</b>
3.1	CRLB for joint Positioning and Synchronization . . . . .	11
3.1.1	Cramér-Rao Lower Bound . . . . .	12
3.1.2	Fundamental Error Bounds . . . . .	15
3.2	Numerical Analysis and Performance Evaluation . . . . .	16
3.2.1	Positioning and Synchronization Performance . . . . .	17
3.2.2	Performance in an Exemplary Environment . . . . .	18
3.3	Conclusion . . . . .	21
<b>4</b>	<b>Algorithms for Calibration, Synchronization and Positioning</b>	<b>25</b>
4.1	Reciprocity Calibration in Distributed Massive MIMO for Coherent Operation . . . . .	25
4.1.1	Problem Description . . . . .	26
4.1.2	Calibration Signal Model . . . . .	28
4.1.3	Numerical Results . . . . .	31
4.2	Graph-based Subarray Fusion for Channel Estimation . . . . .	33
4.3	EKF-based Position Tracking and Clock-synchronization . . . . .	36
4.3.1	UE Motion Model . . . . .	36
4.3.2	Clock Offset Model . . . . .	37
4.3.3	Measurement Configurations . . . . .	37
4.3.4	Extended Kalman Filter (EKF) . . . . .	38
4.3.5	Simulation Scenario . . . . .	38
4.3.6	Simulation Results . . . . .	40
4.3.7	Conclusion and Discussion . . . . .	43
<b>5</b>	<b>Joint Positioning, Learning and Sensing</b>	<b>45</b>
5.1	MIMO Radar-based Environment Sensing . . . . .	45
5.1.1	Channel Model . . . . .	45
5.1.2	Radar Imaging . . . . .	47

5.1.3	Edge Detection and Surface Estimation . . . . .	47
5.1.4	Synthetic Aperture Measurements . . . . .	48
5.2	Application Examples . . . . .	49
5.2.1	Geometry-based Beamforming . . . . .	49
5.2.2	Beam Phase Optimization for WPT . . . . .	49
5.2.3	Dual-band Operation . . . . .	50
5.2.4	Multipath-based positioning . . . . .	51
<b>6</b>	<b>Summary</b>	<b>53</b>
<b>A</b>	<b>Fisher Information Matrix for Channel Parameters</b>	<b>55</b>
	<b>Bibliography</b>	<b>60</b>

# List of Figures

2.1	Overview of system scenario. (a) Environment floor plan including the most important aspects and outlining multipath propagation encompassing diffuse multipath component (DMC) and specular multipath components (SMCs). An exemplary mirror source $\mathbf{a}_{k=2}^{(1)}$ is shown. (b) Coordinate system and array definitions for a subarray at location $\mathbf{a}_k^{(j)}$ with array elements $\mathbf{a}_{k,m}^{(j)}$ including an exemplary component direction of arrival (DOA) $\mathbf{u}(\varphi, \vartheta)$ and corresponding unit vectors in Cartesian and spherical coordinates. . . . .	6
3.1	PEB (a), CEB (b) and PHEB (c) evaluated for varying system bandwidth $B$ values for system configurations (I-a) to (I-e) from Table 3.1. . . . .	19
3.2	PEB distribution for configurations (II-a) in (a)-(c), (II-b) in (d)-(f) and (II-d) in (g)-(i) specified in Table 3.1. . . . .	22
3.3	PEB distribution for configurations (II-e) in (a)-(c), (III-b) in (d)-(f) and (IV-b) in (g)-(i) from Table 3.1. . . . .	23
3.4	CDF curves for the different system configurations outlined in Tab. 3.1, as well as for different the synchronization states. In (a) there are $J = 4$ CSPs, in (b) $J = 2$ CSPs, and in (c) a single CSP is used ( $J = 1$ ). Note that the total number of antennas remains fixed as $N_{\text{total}} = 1024$ . . . . .	24
4.1	Alignment Error metric versus signal-to-noise ratio (SNR) for the case of calibrating using 3 distinct measurements sets. . . . .	32
4.2	(a) 3D model demonstrating the simulation environment. The 75 subarrays of the RW are denoted with markers highlighted with different colors. The red square marker represents the static UE. (b) Subarrays are indexed in top-to-bottom “zigzag” order. . . . .	34
4.3	Results for fully synthetic measurements with the BP-based algorithm given SNR = 18 dB and subarray dimension $4 \times 4$ . Estimates of (a) distance, (b) component SNR, (c) azimuth angle-of-arrival (AOA) and (d) elevation AOA. The black solid lines denote the true SMC parameters. The gray dots denote the false alarm measurements. The estimates of different SMCs are denoted with densely-dashed lines with square markers in different colors. . . . .	35
4.4	Results for fully synthetic measurements with the proposed algorithm given SNR = {18, 30} dB and subarray dimensions of $4 \times 4$ and $8 \times 8$ , respectively. MOSPA errors of the estimated (a) distances, (b) azimuth AOAs, (c) elevation AOAs, (d) input component SNRs, and (e) the averaged number of detected SMCs. . . . .	35
4.5	Setup with the trajectory of the agent and antenna array positions used in simulations.	40

4.6	Comparison of error metrics for different measurement setups (only angular measurements versus angular and range measurements as well as one used array versus two CSPs). . . . .	41
4.7	Comparison of error metrics for different measurement setups where a clock offset has been introduced (only angular measurements versus angular and range measurements as well as one used array versus two CSPs). . . . .	42
4.8	Offsets for the first 5 sub-arrays compared with the corresponding tracked values.	42
4.9	Comparison of error metrics for different measurement setups where an additional clock offset with skew is introduced (only angular measurements versus angular and range measurements as well as one CSP versus two CSPs). . . . .	43
4.10	Comparison between the root-mean-square error (RMSE) obtained for high, medium and low range and angle accuracy, showing the simulation results for different algorithm scenarios denoted as no correction (NC), angle-only (AO), with correction (WC), baseline case (BL). . . . .	44
5.1	3D model of the environment sensing measurement scenario. . . . .	46
5.2	Bistatic MIMO radar imaging and environment sensing. . . . .	48
5.3	Phasor optimization in a simultaneous multibeam transmission. . . . .	50
5.4	Measured path gain distributions. . . . .	51
5.5	Bistatic MIMO radar imaging and environment sensing (dual band). . . . .	52
5.6	Phasor optimization in a simultaneous multibeam transmission (dual-band). . . . .	52

# List of Tables

3.1	System configurations investigated in different sections. . . . .	17
4.1	Color scheme used in the result plots. . . . .	40

# List of Abbreviations

**2D** two-dimensional. 46

**3D** three-dimensional. 45

**AOA** angle-of-arrival. 11, 17, 32, 34, 36, 40, V

**AWGN** additive white Gaussian noise. 11

**CDF** cumulative distribution function. 40–42

**CEB** clock error bound. 14, 15

**CRLB** Cramér-Rao lower bound. 3, 11, 14, 15, 38, II

**CSI** channel state information. 2, 48

**CSP** Contact Service Point. 2–5, 7–17, 19, 20, 23–28, 30, 31, 33, 35–37, 39–42, 44, 46, 50, 52–54, II, V, VI

**DL** downlink. 4

**DMC** diffuse multipath component. 4, 5, 10, 11, 15–17, V

**DNR** diffuse-signal-to-noise ratio. 15

**DOA** direction of arrival. 5, 6, V

**EFIM** equivalent Fisher information matrix (FIM). 14

**EKF** extended Kalman filter. 35, 37, 39, 41, 42, 52, 53

**EN** energy neutral. 45, 48

**END** energy neutral device. 2, 4, 48

**FIM** Fisher information matrix. 11, 12, 14, 54

**LOS** line-of-sight. 8, 10–12, 17, 32, 35, 44, 46, 48

**MIMO** multiple-input multiple-output. 3, 8, 20, 24, 25, 27, 30, 32, 44, 47, 51, 53, II

**MISO** multiple-input single-output. 44, 47, 48

**MPC** multipath component. 2, 5, 52

- MRT** maximum ratio transmission. 46, 48, 53
- NLOS** non-line-of-sight. 24, 50, 52, 53, II
- PDP** power delay profile. 10
- PEB** position error bound. 14–17, 19, 20
- PHEB** phase error bound. 14, 15
- RF** radio frequency. 8, 24
- RMSE** root-mean-square error. 39–43, VI
- RW** RadioWeaves. 2–5, 9–11, 20, 24, 32, 33, 35, 36, 44, 49, 52, 53, II
- SA** synchronization anchor. 45, 47
- SEB** synchronization error bound. 14
- SIMO** single-input multiple-output. 10
- SINR** signal-to-interference-plus-noise ratio. 16, 17
- SMC** specular multipath component. 5–8, 20, 24, 32–34, 44, 45, 47–49, V
- SNR** signal-to-noise ratio. 2, 15, 17, 30–32, 34, 52, V
- TOA** time-of-arrival. 36
- UE** user equipment. 2, 4–8, 11, 12, 15, 16, 25, 26, 35, 39, 40, 42, 44, 46, 48, 49, 52, 53, II
- UL** uplink. 4
- ULA** uniform linear array. 11, 46, 47
- URA** uniform rectangular array. 15, 46–48, 50
- VNA** vector network analyzer. 47
- WPT** wireless power transfer. 2, 49, 50

# Chapter 1

## Introduction and Overview

RadioWeaves (RW) infrastructure is characterized by the extremely large system aperture and a wide distribution in the environment. While a large aperture is in general highly sought after in positioning applications, the wide distribution is an additional positive factor, allowing to expect high performance in idealized conditions. On the downside, while the maximum system bandwidth in RW is limited [1], one can expect a higher computational complexity due to the massive amount of data, i.e., in the context of this deliverable being the received and sampled transmit signals or the estimated channel state information (CSI), that are passed to the dedicated, task specific algorithms. To this end, apart from the investigation of algorithms working on an optimum system, it will also be of interest to investigate algorithmic "trade-offs". For example, position information is contained in specular multipath components (MPCs), which can be estimated with high accuracy by super-resolution algorithms, but it may be computationally prohibitive to apply these algorithms to the data of the full system aperture. A subarray approach, as already used in D1.2 [2], can be seen as a well-suited trade-off, to overcome both of these problems: it allows to balance estimation accuracy with computational and system design complexity. The results from D1.2 [2] have shown that, over the full aperture, the propagation conditions will be non-stationary, which needs to be included correctly captured and treated by algorithms. Finally, another important factor from an algorithm perspective is any additional information that can be extracted and passed on to different parts of the RW system, e.g., leveraging environment information for wireless power transfer (WPT) [3] or for positioning [4]. This could be, for example, MPC visibility regions along a Contact Service Point (CSP), but also the estimated MPC signal-to-noise ratio (SNR) values to quantify the link reliability in different regions of the environment.

The RW system [5, 1] consists of widely distributed base stations, termed CSPs, which enable signal exchange with the user equipment (UE) devices in the system. These UE devices can belong to the different classes introduced in D1.1 [5], e.g., energy neutral device (END) (Class 1) or devices with sufficient power storage to perform active tasks (Class 5). From a positioning perspective, a CSP is termed an anchor and is used to perform positioning in a global frame of reference, while a UE is a device to localize and commonly termed the agent.

In this deliverable, we discuss algorithmic approaches to enable positioning, synchronization, and calibration by means of the distributed RW infrastructure in realistic environments. In addition to these, it also investigates possible approaches for learning or estimation of site-specific properties that might even change after deployment, e.g., due to large moving objects. The algorithmic approaches are designed to be highly flexible and adapted to the specifications from WP1 and capable of exploiting the architectures developed in WP2. While the algorithms are described

and evaluated in the following chapters, it is important to note that the following project phase(s) dealing with the experimental validation and proof-of-concept can require adaption of specific aspects of algorithms, or motivate algorithmic extensions. We include a condensed version of the system model from D1.2 [2] to allow for intuitive relation to the previous analysis.

This deliverable is closely linked to the work performed in Task 3.4, while exploiting the system design given in previous deliverables, e.g., D2.1 [1] introducing the terminology and federations, as well as the results for the channel model for RW from D1.2 [2]. The structure of this deliverable is as follows: Chapter 2 revisits the system model and introduces the used notations. Chapter 3 describes the system performance analysis in terms of the Cramér-Rao lower bound (CRLB) as a fundamental performance bound for positioning in different synchronization states. Chapter 4 presents the investigated algorithms for positioning, calibration, and CSP data-fusion. Chapter 5 contains an algorithm for radar-based multiple-input multiple-output (MIMO) sensing. Chapter 6 summarizes and connects the results from the previous chapters and gives an outlook on future work.

# Chapter 2

## System Model

This chapter is a brief recap of the model outlined in D1.2 [2]. It generalizes the system description to fit the specific topics that are dealt with. This will encompass adapting it to allow intuitive computation and derivation of performance bounds and algorithms for positioning and parameter estimation, while also highlighting the connection regarding different forms of calibration and synchronization.

### 2.1 Multipath-based Model

A RW infrastructure consist of multiple CSPs representing access points with the propagation medium, located at positions  $\mathbf{a}^{(j)} = [a_x^{(j)}, a_y^{(j)}, a_z^{(j)}]^\top$  for  $j = \{1, \dots, J\}$ , each equipped antenna arrays consisting of  $M^{(j)}$  array elements in arbitrary geometric configurations at positions  $\mathbf{a}_m^{(j)} = [a_{x,m}^{(j)}, a_{y,m}^{(j)}, a_{z,m}^{(j)}]^\top$  with  $m = \{1, \dots, M^{(j)}\}$ . While different array geometries are well investigated [6, 7] the main point of interest is seen on the general scaling capabilities of RW, with different spatial distributions of CSPs equipped with varying sizes of antenna arrays being of special interest. An arbitrary number  $L$  of mobile device, representing UEs, ENDS or other, are distributed at positions  $\mathbf{p}_l = [p_{x,l}, p_{y,l}, p_{z,l}]^\top$  in the system/environment and interact with the RW infrastructure. This interaction between UEs and RW infrastructure is performed in uplink (UL) or downlink (DL), giving received signals at either CSPs or the UEs. The following section describes the signal(s) at a CSP and the corresponding array elements, at the example of UL transmission from  $L$  UEs.

#### 2.1.1 Signal Model

The signal vector  $\mathbf{r}^{(j)}(f) = [r_1^{(j)}(f), \dots, r_M^{(j)}(f)]^\top$  for all antenna element signals at a CSP  $j$  for a baseband frequency  $f$  is given as

$$\mathbf{r}^{(j)}(f) = \sum_{k=1}^{K^{(j)}} \mathbf{H}_k^{(j)}(f) \tilde{\mathbf{s}}(f) + \mathbf{w}_s^{(j)}(f) + \mathbf{w}^{(j)}(f) \quad (2.1)$$

$$= \mathbf{H}^{(j)}(f) \mathbf{s}(f) + \mathbf{n}^{(j)}(f) \quad (2.2)$$

with the noise term in  $\mathbf{n}^{(j)}(f)$  contains stochastic signal components attributable to scattering or diffuse multipath component (DMC) and (complex) AWGN  $\mathbf{w}^{(j)}$  modeling receiver noise, and  $\tilde{\mathbf{s}}(f) = [s_1(f), \dots, s_M(f)]^\top$  being the transmit waveform at each array element.

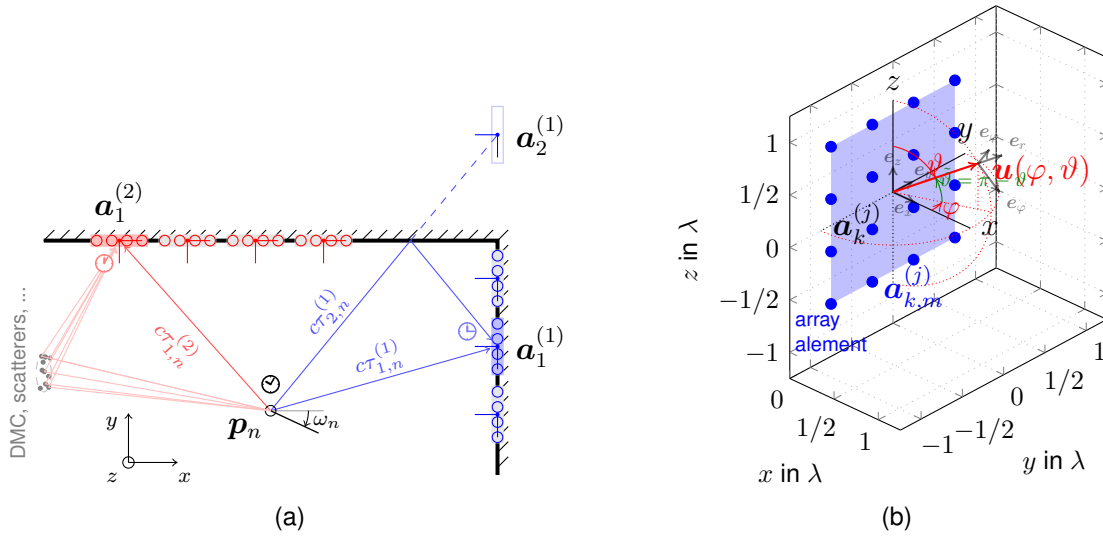


Figure 2.1: Overview of system scenario. (a) Environment floor plan including the most important aspects and outlining multipath propagation encompassing DMC and SMCs. An exemplary mirror source  $\mathbf{a}_{k=2}^{(1)}$  is shown. (b) Coordinate system and array definitions for a subarray at location  $\mathbf{a}_k^{(j)}$  with array elements  $\mathbf{a}_{k,m}^{(j)}$  including an exemplary component direction of arrival (DOA)  $\mathbf{u}(\varphi, \vartheta)$  and corresponding unit vectors in Cartesian and spherical coordinates.

The channel matrix entry from UE  $l$  to antenna  $m$  of the  $j$ th CSP defined as

$$[\mathbf{H}_k^{(j)}(f)]_{m,l} = \alpha_{k,m,l}^{(j)} \exp(j\phi_{k,m,l}^{(j)}) \exp(-j2\pi(f + f_c)\tau_{k,m,l}^{(j)}) \quad (2.3)$$

representing the propagation conditions experienced by the specular multipath component (SMC)  $k \in \{1, \dots, K^{(j)}\}$ , where  $K^{(j)}$  is the number of MPCs per CSP. The SMC amplitude  $\alpha_{k,m,l}^{(j)}$  and phase  $\phi_{k,m,l}^{(j)}$  as well as propagation delay  $\tau_{k,m,l}^{(j)}$  define the medium effects of the signal propagating between the UE at position  $\mathbf{p}_l$  and the CSP antenna (array element) at position  $\mathbf{a}_{k,m}^{(j)}$  with the former two describing path loss and phase shift [2], and the latter defined as the propagation distance

$$c\tau_{k,m,l}^{(j)} = \|\mathbf{p}_l - \mathbf{a}_{k,m}^{(j)}\| \quad (2.4)$$

where  $\mathbf{a}_{k,m}^{(j)}$  is the location of a mirror source representing the  $k$ th SMC and with  $c$  being the speed of light. The operator  $\|\cdot\|$  denotes the vector norm.

For joint processing of different bandwidth signals, we stack all frequency samples of each array element as  $\mathbf{r}_m^{(j)} = [r_m(f_1), \dots, r_m(f_N)]^T$ . When following the direction of a subarray-based processing approach as already outlined in D1.2 [2], applying standard array processing assumptions becomes possible, supported by the fact that the envisioned RW subarrays will be small compared to the full RW aperture. This separation of one large(r) CSP into subarrays is illustrated at the example of a generic environment floor plan (shown in 2D for simplicity) in Figure 2.1a. In addition to algorithmic benefits by allowing application of high resolution algorithms, this also allows an efficient use of resources when dealing with high mobility of multiple devices and partially dynamic federations. Note that the differentiation between a CSP and the corresponding subarrays can often be relaxed for simplicity, e.g., when processing capabilities are not of interest to the performance analysis.

## 2.1.2 CSP Subarray Model

To arrive at a tractable subarray model we first apply the far-field plane-wave assumption per subarray and add a clock offset parameter to allow modeling a realistic system that includes synchronization inaccuracies.

Standard approximations in array processing are the plane-wave far field assumption as well as negligible propagation attenuation for waves propagating along the (sub)array aperture [6]. This allows to relax the definition of (2.4) (omitting the UE index  $l$  for simplicity) by

$$c\tau_{k,m}^{(s)} \approx c\tau_k^{(s)} + (\mathbf{u}_k^{(s)})^\top \mathbf{a}_{k,m}^{(s)} \quad (2.5)$$

with

$$c\tau_k^{(s)} = \|\mathbf{p} - \mathbf{a}_k^{(s)}\| = \begin{bmatrix} x_k^{(s)} \\ y_k^{(s)} \\ z_k^{(s)} \end{bmatrix} \quad (2.6)$$

and  $\mathbf{u}_k^{(j)} = \mathbf{u}(\varphi_k^{(j)}, \vartheta_k^{(j)})$  representing the direction vector of the  $k$ th SMC. The arrival angles at subarray  $s$  for component  $k$  are defined as

$$\varphi_k^{(s)} = \text{atan} \left( \frac{y_k^{(s)}}{x_k^{(s)}} \right) - \bar{\varphi}_{\text{az}}^{(s)} \quad (2.7)$$

$$\vartheta_k^{(s)} = \text{atan} \left( \frac{\sqrt{(x_k^{(s)})^2 + (y_k^{(s)})^2}}{z_k^{(s)}} \right) - \bar{\vartheta}_{\text{el}}^{(s)} \quad (2.8)$$

where  $\bar{\vartheta}_{\text{az}}^{(s)}$  and  $\bar{\vartheta}_{\text{el}}^{(s)}$  are defining the orientation of subarray  $s$  w.r.t. the  $x$  and  $z$  axis and  $\text{atan}(\cdot)$  denotes the corresponding arc tangent function giving unambiguous angles<sup>1</sup> (also known as the four-quadrant inverse tangent). The DOA vector is defined for azimuth angle  $\varphi \in [0, 2\pi]$  and elevation angle  $\vartheta \in [0, \pi]$  as

$$\mathbf{u}(\varphi, \vartheta) = \begin{bmatrix} \cos \varphi \sin \vartheta \\ \sin \varphi \sin \vartheta \\ \cos \vartheta \end{bmatrix} \quad (2.9)$$

with  $\varphi$  representing the azimuth angle from the  $x$ -axis on,  $\vartheta$  the elevation angle from the  $xy$ -axis upwards positive. An illustration of all quantities for an exemplary SMC is given in Figure 2.1b. The corresponding vectors  $\mathbf{e}_\varphi$  and  $\mathbf{e}_\vartheta$  are unit vectors (see Figure 2.1b) that are defined as

$$\mathbf{e}_r = \cos \varphi \sin \vartheta \mathbf{e}_x + \sin \varphi \sin \vartheta \mathbf{e}_y + \cos \vartheta \mathbf{e}_z = \mathbf{u}(\varphi, \vartheta) \quad (2.10)$$

$$\mathbf{e}_\vartheta = \cos \varphi \cos \vartheta \mathbf{e}_x + \sin \varphi \cos \vartheta \mathbf{e}_y - \sin \vartheta \mathbf{e}_z = \begin{bmatrix} \cos \varphi \cos \vartheta \\ \sin \varphi \cos \vartheta \\ \sin \vartheta \end{bmatrix} \quad (2.11)$$

$$\mathbf{e}_\varphi = -\sin \varphi \mathbf{e}_x + \cos \varphi \mathbf{e}_y = \begin{bmatrix} -\sin \varphi \\ \cos \varphi \\ 0 \end{bmatrix} \quad (2.12)$$

<sup>1</sup>Note that this is obtained by simply using the function `atan2(...)` in Matlab or `numpy.arctan2(...)` python.

with

$$\mathbf{e}_x = \begin{bmatrix} 1 \\ 0 \\ 0 \end{bmatrix} \quad \mathbf{e}_y = \begin{bmatrix} 0 \\ 1 \\ 0 \end{bmatrix} \quad \mathbf{e}_z = \begin{bmatrix} 0 \\ 0 \\ 1 \end{bmatrix} \quad (2.13)$$

being unit vectors in Cartesian coordinates.

The amplitudes of each SMC  $k$  at array element  $m$  are approximated as constant per subarray  $s = \{1, \dots, S^{(j)}\}$  of CSP  $j$ , i.e., defined according to

$$\alpha_{k,m}^{(s)} \approx \alpha_k^{(s)}. \quad (2.14)$$

To model timing imperfections, at each subarray a clock offset  $\epsilon^{(s)}$  of the local clock at subarray  $s$  is included, assumed to be independent of the system layout. This represents the offset towards a common reference clock, with the effect of this offset on the system performance analyzed in the chapter dealing with fundamental performance bounds.

Inserting the above approximations into (2.3) and taking the clock parameter into account results in the received signal at array element  $m$  as

$$\mathbf{r}_m^{(s)} = \sum_{k=1}^{K^{(s)}} \alpha_k^{(s)} \underbrace{\exp(-j2\pi f_c(\tau_k^{(s)} + \epsilon^{(s)} + j\psi_k^{(s)}))}_{\exp(i\phi_k^{(s)})} \exp(-j2\pi f_c(\mathbf{u}_k^{(s)})^\top \mathbf{a}_m^{(s)}) \mathbf{x}_m(\boldsymbol{\theta}_k^{(s)}) + \mathbf{n}_m^{(s)} \quad (2.15)$$

where  $\boldsymbol{\theta}_k^{(s)} = [\tau_k^{(s)}, (\mathbf{u}_k^{(s)})^\top]^\top$  denotes the position-related parameter vector for the  $k$ th SMC and  $\mathbf{x}_m(\cdot)$  represents the parameterized transmit baseband signal atom defined as

$$\mathbf{x}_m(\boldsymbol{\theta}) = \mathbf{b}(\tau) \circ \mathbf{g}_m(\mathbf{u}) \circ \mathbf{c}(\epsilon) \circ \mathbf{s} = \mathbf{b}(\tau) \circ \mathbf{g}_m(\varphi, \vartheta) \circ \mathbf{c}(\epsilon) \circ \mathbf{s} \quad (2.16)$$

where the operator  $\circ$  denotes the Hadamard product (element-wise multiplication). The steering vectors are defined using the baseband frequencies  $f_n$  as

$$[\mathbf{b}(\tau)]_n = \exp(-j2\pi f_n \tau) \quad \text{phase shift due to delay} \quad (2.17)$$

$$[\mathbf{g}_m(\varphi, \vartheta)]_n = \exp(-j2\pi f_n \mathbf{u}(\varphi, \vartheta)^\top \mathbf{a}_m / c) \quad \text{phase shift due to array geometry} \quad (2.18)$$

$$[\mathbf{c}(\epsilon)]_n = \exp(-j2\pi f_n \epsilon) \quad \text{phase shift due to clock offset} \quad (2.19)$$

$$\mathbf{s} = [s_b(f_1), \dots, s_b(f_N)]^\top \quad \text{baseband signal (vector)}. \quad (2.20)$$

Note that  $\tau_k^{(s)}$  and  $\epsilon^{(s)}$  are not separable on the level of the channel parameters, but in the position domain, i.e.,  $\tau_{k,l}^{(s)}$  is a function of the UE position, whereas  $\epsilon_l^{(s)}$  is not (according to the model). Different parameter transformations are briefly discussed in the following section.

### 2.1.3 Summary of Parameters of Interest

By performing array processing, the received complex baseband signal can be decomposed into different SMC by means of a beamformer, a parametric super-resolution estimator or similar [8]. The corresponding parameters to estimate are then delays  $\tau \in \mathbb{R}$ , directions  $\mathbf{u}(\varphi, \vartheta) \in \mathbb{R}^3$  and

complex amplitudes  $\alpha \in \mathbb{C}$  as well as the number of components to estimate, termed the channel parameters.

$$\tau_{k,m}^{(j)} \in \mathbb{R}, \alpha_{k,m}^{(j)} \in \mathbb{C} \quad \text{SISO channel parameters} \quad (2.21)$$

↓

*array processing*

$$(\tau_k^{(j)}, \mathbf{u}_k^{(j)}) \in \mathbb{R}, \alpha_k^{(j)} \in \mathbb{R}, \phi_k^{(j)} \in \mathbb{R} \quad \text{channel parameters} \quad (2.22)$$

↓

*position estimation*

$$\underbrace{\mathbf{p} \in \mathbb{R}^3}_{\text{position}}, \underbrace{\xi^{(j)} \in \mathbb{R}, \epsilon^{(j)} \in \mathbb{R}}_{\text{synchronization}}, \underbrace{\alpha_k^{(j)} \in \mathbb{R}, \tilde{\phi}_k^{(j)} \in \mathbb{R}}_{\text{nuisance}} \quad \text{position parameters} \quad (2.23)$$

where the separate component phases are defined according to

$$\phi_k^{(j)} = [\phi_1^{(j)}, \dots, \phi_K^{(j)}]^\top = [\xi^{(j)}, \phi_2^{(j)}, \dots, \phi_K^{(j)}]^\top = [\varphi^{(j)}, \tilde{\phi}^{(j)\top}]^\top. \quad (2.24)$$

Parameters of interest are then the UE position and phase and clock synchronization parameters for each subarray  $\theta = \{\mathbf{p}, \{\epsilon^{(j)}\}, \{\xi^{(j)}\}\}$  with  $\xi^{(j)} = \phi_1^{(j)}$  being the line-of-sight (LOS) phase, corresponding to the phase offset between subarrays, and  $\epsilon^{(j)}$  the clock offset between subarrays.

## 2.2 Calibration Model

While the propagation channel is reciprocal, under imperfect calibration of transmitter and receiver this reciprocity will usually not hold. With respect to distributed MIMO systems studied in Chapter 4, the corresponding channel matrix can be related with the model given in (2.1) by comparing it with the deterministic part containing a finite number of SMCs and the stochastic part  $\mathbf{w}_s(f)$  representing scattering or diffuse components

$$\mathbf{H}^{(j)}(f)\mathbf{s}(f) + \mathbf{w}_s^{(j)}(f) = \sum_{k=1}^{K^{(j)}} \mathbf{H}_k^{(j)}(f)\mathbf{s}(f) + \mathbf{w}_s^{(j)}(f) \leftrightarrow \begin{cases} \mathbf{H}_{\text{UL}} = \mathbf{R}_{\text{CSP}}\mathbf{H}\mathbf{T}_{\text{UE}} & \text{uplink} \\ \mathbf{H}_{\text{DL}} = \mathbf{R}_{\text{UE}}\mathbf{H}\mathbf{T}_{\text{CSP}} & \text{downlink} \end{cases}$$

that remaining differences lie in the assumed perfect calibration of all antennas, arrays, and radio frequency (RF) transmit and receive chains alike. These are captured in the matrices  $\mathbf{R}_{\text{CSP}}$  and  $\mathbf{T}_{\text{CSP}}$  containing the complex gains of transmit and receive chain at the CSP-side, and the matrices  $\mathbf{R}_{\text{UE}}$  and  $\mathbf{T}_{\text{UE}}$  at the UE-side respectively, which is the topic of Section 4.1.

## 2.3 Synchronization Model

We assume two levels of synchronization. A general clock offset exists between all devices, and a phase offset between all devices, both w.r.t. a reference device that is used as time and phase reference. The clock offset represents coarse synchronization of the separate device clocks, whereas the phase synchronization represents carrier phase synchronization. Knowledge of both results in a fully coherent system, e.g., all CSPs can be used together as a large coherent array. A summary of these different states is

General clock synchronization models and performance are analyzed in [9], with a model similar to the employed in [10] for a distributed MIMO system seen as a good candidate for the positioning

unsynchronized	unsync. (UN)	$\epsilon^{(j)}$ unknown, $\xi^{(j)}$ unknown
clock synchronized	clk. sync. (CLK)	$\epsilon^{(j)}$ known, $\xi^{(j)}$ unknown
fully coherent	coh. (COH)	$\epsilon^{(j)}$ known, $\xi^{(j)}$ known

aspect of the RW infrastructure. When it is necessary to consider a time varying clock offset, it is seen sufficient to assume a linear drift over time [10], according to

$$\epsilon^{(j)}(t) = \epsilon^{(j)} + t \cdot \delta^{(j)} \quad (2.25)$$

where  $t$  represents the global time,  $\delta^{(j)}$  is the clock skew of CSP/subarray  $j$ , and  $\epsilon^{(j)}$  is the initial clock offset.

# Chapter 3

## Fundamental Performance Limits

This chapter introduces and analyzes the fundamental performance limits for positioning and synchronization for a RW system consisting of multiple CSPs in configurations consisting of multiple subarrays each. The main point of interest is the achievable performance for positioning for different system configurations, e.g., number of subarrays, number of array elements per subarray, number of CSPs, as well as the dependency on system parameters such as bandwidth. This will give valuable insights into hardware requirements to achieve different levels of performance and allows quantifying losses due to system restrictions.

### 3.1 CRLB for joint Positioning and Synchronization

Based on the signal model described in Sections 2.1.1 and 2.1.2, we employ a simplified signal model consisting only of the LOS and DMC in a single-input multiple-output (SIMO) scenario, where the corresponding received signal at the CSP becomes

$$\mathbf{r}_m^{(j)} = \alpha^{(j)} \exp(-j2\pi f_c(\mathbf{u}_k^{(s)})^\top \mathbf{a}_m^{(s)} + j\phi_k^{(j)}) \mathbf{x}_m(\boldsymbol{\theta}_{\text{ch}}^{(j)}) + \mathbf{w}_{\text{s},m}^{(j)} + \mathbf{w}_m^{(j)} \quad (3.1)$$

with the deterministic component defined for later use as

$$\boldsymbol{\mu}_m^{(j)} = \alpha^{(j)} \exp(-j2\pi f_c(\mathbf{u}_k^{(s)})^\top \mathbf{a}_m^{(s)} + j\phi_k^{(j)}) \mathbf{x}_m(\boldsymbol{\theta}_{\text{ch}}^{(j)}) \quad (3.2)$$

where  $\boldsymbol{\theta}_{\text{ch}}^{(j)}$  are the channel parameters for the  $j$ th CSP. This allows us to investigate fundamental performance limits that allow a more intuitive interpretation due to the simpler scenario, while still keeping important aspects of the model. For the DMC, we rely on a general stochastic model, modeling the stochastic part  $\mathbf{w}_{\text{s},m}^{(j)}$  to exhibit an exponential power delay profile (PDP) [11, 12] with DMC parameters of total power  $P_{\text{dmc}}$ , decay time constant  $T_{\text{dmc}}$  and onset time  $\tau_{\text{dmc}}$ , chosen to reasonable values for the corresponding environment under consideration. When necessary, these can be stacked into the DMC parameter vector  $[P_{\text{dmc}}, \tau_{\text{dmc}}, T_{\text{dmc}}]^\top$ . For simplicity, the DMC parameters are assumed known, e.g., due to calibration measurements in actual deployment.

#### Covariance Matrix of the Diffuse Component

For simplicity, we assume the DMC  $\mathbf{w}_{\text{s},m}^{(j)}$  to be statistically independent between different array elements, which allows the use of the Kronecker and Hadamard products. The covariance matrix of the noise terms of all array element signals of DMC  $\mathbf{w}_s^{(j)} = [\mathbf{w}_s^{(j)}(f_1), \dots, \mathbf{w}_s^{(j)}(f_N)]^\top$  and

additive white Gaussian noise (AWGN)  $\mathbf{w}^{(j)} = [\mathbf{w}^{(j)}(f_1), \dots, \mathbf{w}^{(j)}(f_N)]^T$  for an arbitrary CSP  $j$  (neglecting the index for brevity) is defined as [13]

$$\mathbf{C}(\boldsymbol{\theta}_{\text{dmc}}) = \mathbb{E}[(\mathbf{w}_s + \mathbf{w})(\mathbf{w}_s + \mathbf{w})^H] \quad (3.3)$$

$$= (\mathbf{C}_m(\boldsymbol{\theta}_{\text{dmc}}) \otimes \mathbf{I}_M) \circ (\mathbf{s}\mathbf{s}^H \otimes \mathbf{1}_M \mathbf{1}_M^T) + \sigma^2 \mathbf{I}_{MK} \quad (3.4)$$

$$= (\mathbf{C}_m(\boldsymbol{\theta}_{\text{dmc}}) \circ \mathbf{s}\mathbf{s}^H) \otimes \mathbf{I}_M + \sigma^2 \mathbf{I}_{MN} \quad (3.5)$$

with a per-array-element covariance matrix

$$\mathbf{C}_m(\boldsymbol{\theta}_{\text{dmc}}) = \text{toep}[\boldsymbol{\kappa}(\boldsymbol{\theta}_{\text{dmc}}), \boldsymbol{\kappa}(\boldsymbol{\theta}_{\text{dmc}})^H] \quad (3.6)$$

where  $\boldsymbol{\kappa}(\boldsymbol{\theta}_{\text{dmc}})$  is the sampled DMC power spectral density defined as [11, Eq. (2.61)]

$$\psi_{\text{dmc}}(f) = \frac{P_{\text{dmc}}}{1/(BT_{\text{dmc}}) + j2\pi f} \exp(-j2\pi f \tau_{\text{dmc}}) \quad (3.7)$$

where  $P_{\text{dmc}}$ ,  $\tau_{\text{dmc}}$ , and  $T_{\text{dmc}}$ , are the power, onset delay, and the decay constant of the DMC, respectively.

### 3.1.1 Cramér-Rao Lower Bound

In this section, we formulate and derive the CRLB to investigate the achievable accuracy in terms of joint positioning and synchronization. To this end we extend the bounds derived for a single CSP in [14] and for a distributed system of uniform linear arrays (ULAs) [13] and incorporate imperfect synchronization of the overall system. The CRLB for the variance of any unbiased estimator is defined as [15]

$$\mathbb{E}_{\boldsymbol{\theta}} [(\hat{\boldsymbol{\theta}} - \boldsymbol{\theta})(\hat{\boldsymbol{\theta}} - \boldsymbol{\theta})^T] \succeq \mathbf{J}_{\text{pos}}^{-1} \quad (3.8)$$

where  $\mathbf{J}_{\text{pos}}$  is the FIM for the parameter vector  $\boldsymbol{\theta} = [\mathbf{p}^T, \boldsymbol{\theta}_{\text{sync}}^T, \boldsymbol{\alpha}^T]^T$  containing the UE position, the synchronization parameters clock and phase offset in  $\boldsymbol{\theta}_{\text{sync}} = [\{\epsilon^{(j)}\}, \{\varphi^{(j)}\}]^T \in \mathbb{R}^{N_{\text{syn}}}$  in suitable configurations, discussed below in detail, as well as nuisance parameters in form of LOS amplitudes for each CSP-UE link  $\boldsymbol{\alpha} = [\alpha^{(1)}, \dots, \alpha^{(J)}]^T$ .  $N_{\text{syn}}$  is used to denote the number of synchronization parameters. We assume that each CSP  $j$  contributes independent information on  $\boldsymbol{\theta}$ , i.e., we assume DMC and noise to be identical distributed and independent for each CSP. The FIM for the joint positioning and synchronization problem thus becomes the sum over the FIM for each CSP according to

$$\mathbf{J}_{\text{pos}} = \sum_{j=1}^J \mathbf{J}_{\text{pos}}^{(j)} = \sum_{j=1}^J \mathbf{T}^{(j)} \mathbf{J}_{\text{ch}}^{(j)} (\mathbf{T}^{(j)})^T \quad (3.9)$$

where  $\mathbf{J}_{\text{pos}}^{(j)}$  represents the FIM contribution provided by the  $j$ th CSP, which is related to the channel parameter FIM  $\mathbf{J}_{\text{ch}}^{(n)}$  of each CSP via the corresponding Jacobian matrix  $\mathbf{T}^{(j)}$ . The channel parameter vector of the  $n$ th RW is defined as

$$\boldsymbol{\theta}_{\text{ch}}^{(j)} = [\varphi^{(j)}, \vartheta^{(j)}, \tau^{(j)}, \phi^{(j)}, \alpha^{(j)}]^T \in \mathbb{R}^{5 \times 1} \quad (3.10)$$

containing the delay  $\tau^{(j)}$ , the angle-of-arrival (AOA) in azimuth  $\varphi^{(j)}$  and elevation  $\vartheta^{(j)}$ , the amplitude  $\alpha^{(j)}$  and phase  $\phi^{(j)}$  for the corresponding LOS path of the  $j$ th CSP. The elements of the FIM  $\mathbf{J}_{\text{ch}}^{(j)}$  in (3.9) are defined as [15, Sec. 15.7]

$$[\mathbf{J}_{\text{ch}}^{(j)}]_{m,n} = 2\Re \left[ \frac{\partial(\boldsymbol{\mu}^{(j)})^H}{\partial[\boldsymbol{\theta}_{\text{ch}}^{(j)}]_m} \mathbf{C}^{-1} \frac{\partial\boldsymbol{\mu}^{(j)}}{\partial[\boldsymbol{\theta}_{\text{ch}}^{(j)}]_n} \right] \quad (3.11)$$

where  $\boldsymbol{\mu}^{(j)} = \alpha^{(j)} \exp(\dots) \mathbf{x}(\boldsymbol{\theta}_{\text{ch}}^{(j)})$  as defined in (3.2) where  $\mathbf{x}(\boldsymbol{\theta}_{\text{ch}}^{(j)})$  contains all frequency samples of the  $M^{(j)}$  array element signals for the  $j$ th CSP in suitable stacking order. The derivation of the elements of the channel FIM is given in more detail in Appendix A.

To gain insight into the achievable performance, we investigate the three levels of synchronization outlined in Section 2.3, thus requiring a different Jacobian matrix  $\mathbf{T}^{(j)}$  for each CSP, due to the different number of parameters that need to be estimated. We consider the case of a fully coherent system (all subarrays of all CSPs are clock and phase synchronized), the case of all CSPs and corresponding subarrays exhibiting a phase offset w.r.t. some arbitrarily chosen reference phase while being fully clock synchronized, and the case of unknown phase and clock offsets for all CSP subarrays. While a fully coherent system is expected to give the highest accuracy due to the extremely large aperture and consequently resolution, it is not considered to be a realistic scenario in actual deployment, but included as the theoretically possible optimum baseline.

The general Jacobian matrix  $\mathbf{T}^{(j)}$  can be summarized as a block matrix

$$\mathbf{T}^{(j)} = \frac{\partial(\boldsymbol{\theta}_{\text{ch}}^{(j)})^T}{\partial\boldsymbol{\theta}} = \begin{bmatrix} \mathbf{P}_{\varphi}^{(j)} & \mathbf{P}_{\vartheta} & \mathbf{P}_{\tau}^{(j)} & \mathbf{P}_{\phi}^{(j)} & \mathbf{0} \\ \mathbf{0} & \mathbf{0} & \mathbf{C}_{\tau}^{(j)} & \mathbf{0} & \mathbf{0} \\ \mathbf{0} & \mathbf{0} & \mathbf{0} & \mathbf{C}_{\phi}^{(j)} & \mathbf{0} \\ \mathbf{0} & \mathbf{0} & \mathbf{0} & \mathbf{0} & \mathbf{1}_J^{(j)} \end{bmatrix} \in \mathbb{R}^{(3+N_{\text{syn}}+J) \times 5} \quad (3.12)$$

transforming the channel parameters  $\boldsymbol{\theta}_{\text{ch}}^{(j)}$  with  $j = 1, \dots, J$  into the (common) position parameters  $\boldsymbol{\theta}$  through

$$\boldsymbol{\theta}_{\text{ch}}^{(j)} \in \mathbb{R}^{5 \times 1} \xrightarrow{\mathbf{T}^{(j)}} \boldsymbol{\theta} = \begin{cases} \boldsymbol{\theta}_{\text{coh}} = [\mathbf{p}^T, \boldsymbol{\alpha}^T]^T \in \mathbb{R}^{(3+J) \times 1} & \text{coherent} \\ \boldsymbol{\theta}_{\text{clk}} = [\mathbf{p}^T, \boldsymbol{\phi}^T, \boldsymbol{\alpha}^T]^T \in \mathbb{R}^{(3+2J) \times 1} & \text{clock synchronized} \\ \boldsymbol{\theta}_{\text{un}} = [\mathbf{p}^T, \boldsymbol{\epsilon}^T, \boldsymbol{\phi}^T, \boldsymbol{\alpha}^T]^T \in \mathbb{R}^{3(J+1) \times 1} & \text{unsynchronized} \end{cases} \quad (3.13)$$

where the clock and phase offset parameters are  $\boldsymbol{\epsilon} = [\epsilon^{(1)}, \dots, \epsilon^{(J)}]^T$  and  $\boldsymbol{\phi} = [\phi^{(1)}, \dots, \phi^{(J)}]^T$ , and the LOS amplitudes for each CSP-UE link  $\boldsymbol{\alpha} = [\alpha^{(1)}, \dots, \alpha^{(J)}]^T$ . The unit vector  $\mathbf{1}_J^{(j)}$  is defined as a length  $J$  zero vector with 1 at the  $j$ th element  $\mathbf{1}_J^{(j)} = [0, \dots, 0, 1, 0, \dots, 0]^T$ . It assigns the amplitude  $\alpha^{(j)}$  in  $\boldsymbol{\theta}_{\text{ch}}^{(j)}$  to the corresponding amplitude in  $\boldsymbol{\alpha}$  in the parameter vectors for positioning as defined in (3.12).

The block matrices relating channel parameters to the position are common to all of the scenarios outlined in (3.13). These are defined for mapping the delay to the position as

$$\mathbf{P}_{\tau}^{(j)} = \frac{\mathbf{p} - \mathbf{a}^{(j)}}{\|\mathbf{p} - \mathbf{a}^{(j)}\|} = \frac{\mathbf{p} - \mathbf{a}^{(j)}}{c\tau^{(j)}} = \frac{1}{c\tau^{(j)}} \begin{bmatrix} \cos(\varphi^{(j)} + \bar{\varphi}_{\text{az}}^{(j)}) \sin(\vartheta^{(j)} + \bar{\vartheta}_{\text{el}}^{(j)}) \\ \sin(\varphi^{(j)} + \bar{\varphi}_{\text{az}}^{(j)}) \sin(\vartheta^{(j)} + \bar{\vartheta}_{\text{el}}^{(j)}) \\ \cos(\vartheta^{(j)} + \bar{\vartheta}_{\text{el}}^{(j)}) \end{bmatrix} \in \mathbb{R}^{3 \times 1} \quad (3.14)$$

from the derivative of  $\tau^{(j)} = \tau_{k=1}^{(j)}$  in (2.5) w.r.t. the position. The mapping of the component phase  $\phi^{(j)} = \phi_{k=1}^{(j)}$  to the position is found as

$$\mathbf{P}_{\phi}^{(j)} = \frac{-2\pi(\mathbf{p} - \mathbf{a}^{(j)})}{\lambda \|\mathbf{p} - \mathbf{a}^{(j)}\|} = \frac{-2\pi(\mathbf{p} - \mathbf{a}^{(j)})}{\lambda c\tau^{(j)}} \in \mathbb{R}^{3 \times 1} \quad (3.15)$$

from the derivative of (2.5) w.r.t. position. Note that this term will only provide information when the general phase term  $\phi_k^{(j)}$  is known, i.e., in a fully coherent system, as it would otherwise need to be estimated as a nuisance parameter.

The Jacobian matrix block for the azimuth angle  $\mathbf{P}_{\varphi}^{(j)}$  is given as

$$\mathbf{P}_{\varphi}^{(j)} = \frac{1}{c\tau^{(j)}} \begin{bmatrix} -\frac{\sin(\varphi^{(j)} + \bar{\varphi}_{\text{az}}^{(j)})}{\sin(\vartheta^{(j)} + \bar{\vartheta}_{\text{el}}^{(j)})} \\ \frac{\cos(\varphi^{(j)} + \bar{\varphi}_{\text{az}}^{(j)})}{\sin(\vartheta^{(j)} + \bar{\vartheta}_{\text{el}}^{(j)})} \\ 0 \end{bmatrix} \quad (3.16)$$

and for the elevation angle as

$$\mathbf{P}_{\vartheta}^{(j)} = \frac{1}{c\tau^{(j)}} \begin{bmatrix} \cos(\varphi^{(j)} + \bar{\varphi}_{\text{az}}^{(j)}) \cos(\vartheta^{(j)} + \bar{\vartheta}_{\text{el}}^{(j)}) \\ \sin(\varphi^{(j)} + \bar{\varphi}_{\text{az}}^{(j)}) \cos(\vartheta^{(j)} + \bar{\vartheta}_{\text{el}}^{(j)}) \\ -\sin(\vartheta^{(j)} + \bar{\vartheta}_{\text{el}}^{(j)}) \end{bmatrix} \quad (3.17)$$

by calculating the derivatives of (2.7) and (2.8), respectively, w.r.t. the position, i.e.,  $x$ -,  $y$ - and  $z$ -coordinates of  $\mathbf{p}$ . While these remain the same for all scenarios (coherent, clock synchronized and unsynchronized), the matrix blocks for the synchronization parameters vary and are described in the following.

**Coherent system:** For the coherent case, no synchronization parameters need to be estimated and the carrier phase can be exploited for positioning. Consequently, the resulting Jacobian matrix for each CSP maps to the same synchronization parameters and becomes

$$\mathbf{T}_{\text{coh}}^{(j)} = \begin{bmatrix} \mathbf{P}_{\varphi}^{(j)} & \mathbf{P}_{\vartheta}^{(j)} & \mathbf{P}_{\tau}^{(j)} & \mathbf{P}_{\phi}^{(j)} & \mathbf{0} \\ \mathbf{0} & \mathbf{0} & \mathbf{0} & \mathbf{0} & \mathbf{1}_J^{(j)} \end{bmatrix} \in \mathbb{R}^{(3+J) \times 5}. \quad (3.18)$$

This Jacobian matrix performs the transformation from  $J$  channel parameter vectors  $\boldsymbol{\theta}_{\text{ch}}^{(j)}$  to the coherent positioning parameter vector  $\boldsymbol{\theta}_{\text{coh}}$ .

**Clock synchronized system:** For the clock synchronized case, the carrier phase cannot be exploited for positioning and one needs to estimate the clock offset between different sub-rays/CSPs. Each of the phase offset parameters is mapped to its own phase offset parameter in the resulting position domain parameter vector  $\boldsymbol{\theta}_{\text{clk}}$ . Consequently, the corresponding matrix block mapping between phase offsets becomes

$$\mathbf{C}_{\phi}^{(j)} = \mathbf{1}_J^{(j)} = [0, \dots, 0, 1, 0, \dots, 0]^T \quad (3.19)$$

$\begin{matrix} \uparrow & \uparrow & \uparrow & \uparrow \\ \tau & \varphi & \varphi & \tau \end{matrix}$

and the full Jacobian matrix for this scenario becomes

$$\mathbf{T}_{\text{clk}}^{(j)} = \begin{bmatrix} \mathbf{P}_{\varphi}^{(j)} & \mathbf{P}_{\vartheta}^{(j)} & \mathbf{P}_{\tau}^{(j)} & \mathbf{P}_{\phi}^{(j)} & \mathbf{0} \\ \mathbf{0} & \mathbf{0} & \mathbf{0} & \mathbf{1}_J^{(j)} & \mathbf{0} \\ \mathbf{0} & \mathbf{0} & \mathbf{0} & \mathbf{0} & \mathbf{1}_J^{(j)} \end{bmatrix} \in \mathbb{R}^{(3+2J) \times 5}. \quad (3.20)$$

**Unsynchronized system:** For the completely unsynchronized system both the phase offset and time offset need to be estimated as nuisance parameters, e.g., they are unknown, and cannot be exploited for positioning directly, but are estimated for each subarray/CSP. Note that this scenario corresponds to the common model of complex component amplitudes encountered in complex baseband notation [4, 16, 14]. Each of the phase offset parameters is mapped to its own phase offset parameter in the resulting position domain parameter vector  $\theta_{\text{clk}}$ . Consequently, the corresponding matrix block mapping between phase offset parameters and clock offset parameters are identical according to

$$\mathbf{C}_{\phi}^{(j)} = \mathbf{C}_{\tau}^{(j)} = \mathbf{1}_J^{(j)} \quad (3.21)$$

and the full Jacobian matrix for this scenario becomes

$$\mathbf{T}_{\text{un}}^{(j)} = \begin{bmatrix} \mathbf{P}_{\varphi}^{(j)} & \mathbf{P}_{\vartheta}^{(j)} & \mathbf{P}_{\tau}^{(j)} & \mathbf{P}_{\phi}^{(j)} & \mathbf{0} \\ \mathbf{0} & \mathbf{0} & \mathbf{1}_J^{(j)} & \mathbf{0} & \mathbf{0} \\ \mathbf{0} & \mathbf{0} & \mathbf{0} & \mathbf{1}_J^{(j)} & \mathbf{0} \\ \mathbf{0} & \mathbf{0} & \mathbf{0} & \mathbf{0} & \mathbf{1}_J^{(j)} \end{bmatrix} \in \mathbb{R}^{3(J+1) \times 5}. \quad (3.22)$$

### 3.1.2 Fundamental Error Bounds

To compute the position error bound (PEB) and synchronization error bound (SEB) from the FIM  $\mathbf{J}_{\theta}$  in (3.9), we partition the parameter vector  $\theta = [\theta_w^T, \theta_u^T]^T$  for the different scenarios into (“wanted”) parameters of interest  $\theta_w = [\mathbf{p}^T, \theta_{\text{sync}}^T]$  consisting of the position and synchronization parameters, and into the (“unwanted”) nuisance parameters  $\theta_u = \alpha$  in terms of the component amplitudes [7]. The FIM is partitioned correspondingly as

$$\mathbf{J}_{\theta} = \begin{bmatrix} \mathbf{J}_{\theta_w \theta_w} & \mathbf{J}_{\theta_w \theta_u} \\ \mathbf{J}_{\theta_w \theta_u}^T & \mathbf{J}_{\theta_u \theta_u} \end{bmatrix} \in \mathbb{R}^{(3+N_{\text{sync}}+J) \times (3+N_{\text{sync}}+J)}. \quad (3.23)$$

To extract the bounds for the parameters of interest, one can either directly invert  $\mathbf{J}_{\theta}$  and investigate the corresponding entries, or compute the equivalent FIM (EFIM) [7, 17, 18] according to

$$\mathbf{J}_{\text{pos}} = \mathbf{J}_{\theta_w \theta_w} - \mathbf{J}_{\theta_w \theta_u} \mathbf{J}_{\theta_u \theta_u}^{-1} \mathbf{J}_{\theta_w \theta_u}^T \in \mathbb{R}^{5 \times 5}. \quad (3.24)$$

Through (3.8), the CRLB for the parameters is then given as

$$\mathbb{E} \left[ (\hat{\theta}_w - \theta_w)(\hat{\theta}_w - \theta_w)^T \right] \succeq \mathbf{J}_{\text{pos}}^{-1} \quad (3.25)$$

which can have computational advantages, while also allowing to obtain closed-form solutions for small setups, i.e., small matrices. Independently, we employ the definition in (3.25) to define the PEB and the SEB in terms of the clock error bound (CEB) and phase error bound (PHEB).

#### Position Error Bound (PEB)

We define the PEB as the trace of the accuracy in  $x$ -,  $y$ - and  $z$ -directions according to [13]

$$\text{PEB} = \sqrt{\text{tr} \left[ [\mathbf{J}_{\text{pos}}^{-1}]_{1:3,1:3} \right]}. \quad (3.26)$$

While this does not allow to get insight into the distribution of the error along the different coordinates, it allows for a single value comparison of the performance.

### Synchronization Error Bounds (SEB)

For the synchronization bounds, we employ a similar definition as for the PEB. As there are  $J$  clock and phase offset parameters to estimate, we define the CEB as the average clock offset estimation error and the PHEB as the average phase offset estimation error according to

$$\text{CEB} = \frac{1}{J} \sum_{\ell=4}^{J+4} \sqrt{[\mathbf{J}_{\text{pos}}^{-1}]_{\ell,\ell}} \quad (3.27)$$

$$\text{PHEB} = \frac{1}{J} \sum_{\ell=J+5}^{2J+5} \sqrt{[\mathbf{J}_{\text{pos}}^{-1}]_{\ell,\ell}} \quad (3.28)$$

## 3.2 Numerical Analysis and Performance Evaluation

In this section, we investigate the theoretical performance limits for localization and synchronization by means of numerical analysis of the CRLB. To this end, we perform a numerical analysis of the results presented in the previous section, investigating parameters of interest. These are most importantly the effect of the signal bandwidth  $B$  on the positioning performance and the effect the size and distribution of the CSPs have on the spatial distribution of PEB. While simulations can be extensive when changing many system parameters, we will focus on varying system parameters while keeping channel and propagation parameters constant, i.e., the DMC parameters are assumed constant and known, discussed in the following section.

### Common Simulation Parameters

The most important propagation parameter settings are outlined in the following paragraph, with specific values added when necessary. The channel amplitudes are generated as  $\alpha_n^{(j)} \propto \sqrt{P_{\text{tx}}} \cdot \text{PL}$  where  $P_{\text{tx}}$  denotes the UE transmit power and path loss PL is set according to free space, i.e.,  $\text{PL} = \lambda / (4\pi \|\mathbf{p} - \mathbf{a}_n^{(j)}\|)$ , whereas the noise power is set to unity, i.e.,  $\sigma_w^2 = 1$  without loss of generality<sup>1</sup>. For the DMC, the normalized coherence bandwidth is set to  $\beta_{\text{dmc}} = 1 / (T_{\text{dmc}} B)$  with  $T_{\text{dmc}} = 10/c$  decay time set to a distance of 10 m, the normalized onset time to  $\tau_{\text{dmc}} = \frac{B}{K} (\tau_{k=0,n}^{(j)} + 1/c)$ , i.e., the DMC onset is delayed by 1 m w.r.t. the LoS, and the peak power  $P_{\text{dmc}}$  is chosen to yield a specific diffuse-signal-to-noise ratio (DNR) defined as  $\text{DNR} = \alpha_{\text{dmc}} / \sigma_w^2 = 20$  dB, which is kept constant over the whole environment. Note that while this selection of the DNR most certainly is not accurate in realistic environments, it nonetheless removes a degree of freedom and allows for controlled simulations, and can furthermore be taken into account in the analysis. For the SNR we use  $\text{SNR}_{1\text{m}} = 30$  dB, defined for a reference distance of 1 m in all simulations.

### Investigated System Configurations

The considered scenario consists of a network of  $N = \{1, 2, 4\}$  CSPs in a medium, with the UE placed at suitable locations  $\mathbf{p} = [x, y, z]^T$  to investigate the positioning performance. The CSPs consist of a varying number of uniform rectangular arrays (URAs) subarrays, each with  $M^{(j)}$  antennas spaced at  $d = \lambda/2$ . The UE transmits some signal, e.g., an OFDM pilot, at a carrier frequency  $f_c = 6.95$  GHz. The signal bandwidth is denote as  $B$  containing  $N$  frequency bins, with  $N$  selected to ensure correct sampling of all signals and  $B$  varied as system parameter to investigate.

<sup>1</sup>Note that the propagation parameters are defined as ratios w.r.t. the noise variance to ensure proper relations.

Table 3.1: System configurations investigated in different sections.

id	antennas per subarray		subarrays per CSP		CSPs	antennas
	geometry	spacing	layout	spacing	$J$	$N_{\text{total}}$
(I-a)	$4 \times 4$	$\lambda/2$	1	–	4	64
(I-b)	$8 \times 8$	$\lambda/2$	1	–	4	256
(I-c)	$4 \times 4$	$\lambda/2$	$2 \times 2$	$\lambda/2$	4	256
(I-d)	$8 \times 8$	$\lambda/2$	$4 \times 4$	$\lambda/2$	4	4096
(I-e)	1	–	$16 \times 16$	$\lambda/2$	4	1024
(II-a)	$4 \times 4$	$\lambda/2$	$4 \times 4$	$\lambda/2$	4	1024
(II-b)	$4 \times 4$	$\lambda/2$	$4 \times 4$	$5\lambda/2$	4	1024
(II-c)	$8 \times 8$	$\lambda/2$	$2 \times 2$	$\lambda/2$	4	1024
(II-d)	$8 \times 8$	$\lambda/2$	$2 \times 2$	$10\lambda/2$	4	1024
(II-e)	$4 \times 4$	$\lambda/2$	$16 \times 1$	$5\lambda/2$	4	1024
(III-a)	$4 \times 4$	$\lambda/2$	$8 \times 4$	$\lambda/2$	2	1024
(III-b)	$4 \times 4$	$\lambda/2$	$8 \times 4$	$5\lambda/2$	2	1024
(III-c)	$8 \times 8$	$\lambda/2$	$4 \times 2$	$\lambda/2$	2	1024
(III-d)	$8 \times 8$	$\lambda/2$	$4 \times 2$	$10\lambda/2$	2	1024
(III-e)	$4 \times 4$	$\lambda/2$	$16 \times 2$	$5\lambda/2$	2	1024
(IV-a)	$4 \times 4$	$\lambda/2$	$8 \times 8$	$\lambda/2$	1	1024
(IV-b)	$4 \times 4$	$\lambda/2$	$8 \times 8$	$5\lambda/2$	1	1024
(IV-c)	$8 \times 8$	$\lambda/2$	$4 \times 4$	$\lambda/2$	1	1024
(IV-d)	$8 \times 8$	$\lambda/2$	$4 \times 4$	$10\lambda/2$	1	1024

The system setup considered in the performance analysis is described in Table 3.1. It indicates the number of antennas per subarray and the subarray geometry, as well as the geometric layout of the subarrays for each CSP, i.e., the number of rows and columns of subarrays and the corresponding spacing. When using different bandwidth values, only a single UE is localized, giving the PEB for the UE at that specific location. In that case, the number of antennas per CSP is varied, first increasing the array itself (I-a, I-b), and next by employing subarrays of varying size (I-c, I-d) and lastly by investigating spherical wave positioning in (I-e). Note that the spacing is varied between-subarrays, while keeping the spacing between subarray elements constant at  $\lambda/2$  for the selected carrier frequency. E.g., spacing subarrays at  $\lambda/2$  gives a continuous CSP are covered with antennas, while a spacing of  $10\lambda/2$  between subarrays yields gaps of  $5\lambda$  between the outermost array elements of adjacent subarrays.

When analyzing the spatial distribution of the PEB for different geometric configurations of CSP in terms of size and layout of subarrays, the bandwidth is kept fixed at  $B = 100$  MHz. Additionally, the total number of antennas is fixed at  $N_{\text{total}} = 1024$ , effectively increasing the aperture per CSP when reducing the number of CSPs.

### 3.2.1 Positioning and Synchronization Performance

We start by numerically analyzing the PEB outlined in Section 3.1 to investigate how the number of antennas  $M$  per CSP and bandwidth  $B$  impact the ultimate positioning accuracy. Fig. 3.1 shows the bounds evaluated for all three synchronization scenarios of coherent (COH, dotted), clock synchronized (CLK, dashed), and unsynchronized (UN, solid).

The PEB shown in Fig. 3.1a shows the characteristic bandwidth dependency of DMC channels, where the stronger overlap at lower bandwidth values results in a decrease of the effective signal-to-interference-plus-noise ratio (SINR), which represents the ratio of signal power to diffuse and noise power. This SINR decrease is attributable to the increasing overlap between DMC and

the LOS component that contains position information. At large bandwidth values, the PEB approaches first a linear trend representing the PEB for the AWGN-only case, where the DMC and the LOS are well separated and the SINR becomes identical to the SNR, followed by a constant value. Showing the scaling behavior in terms of the system layout, the different configurations outlined in Table 3.1 as (I-a) to (I-e), gradually increasing the number of antenna elements per subarray, as well as the number of subarrays per CSP. Starting from the unsynchronized system (UN), an increase of the array size of the CSP yields the expected improvement due to the increased aperture (compare I-a to I-b). The split of the larger CSP into four subarrays with equal aperture and number of array elements exhibits a slight performance decrease, due to the need to estimate the clock offset between subarrays (compare I-b to I-c). To achieve a similar performance with  $4 \times 4$  subarrays as with a single  $8 \times 8$  array, one needs 2 times the aperture in both horizontal and vertical directions (compare I-d to I-b). Lastly, a SIMO receiver (I-e), as expected, achieves the performance of similar sized arrays when clock-synchronized or coherent. For the coherent case, (I-e) represents the case of spherical wavefront positioning with an antenna array, which shows identical performance to the coherent subarrays with the same aperture, i.e. I-d and I-e show identical curves. This is due to the rather small size of the array, where the plane wave model is still a valid approximation. This shows that for the case of coherent subarrays, arrays with the same aperture, i.e., geometric size, exhibit the same performance.

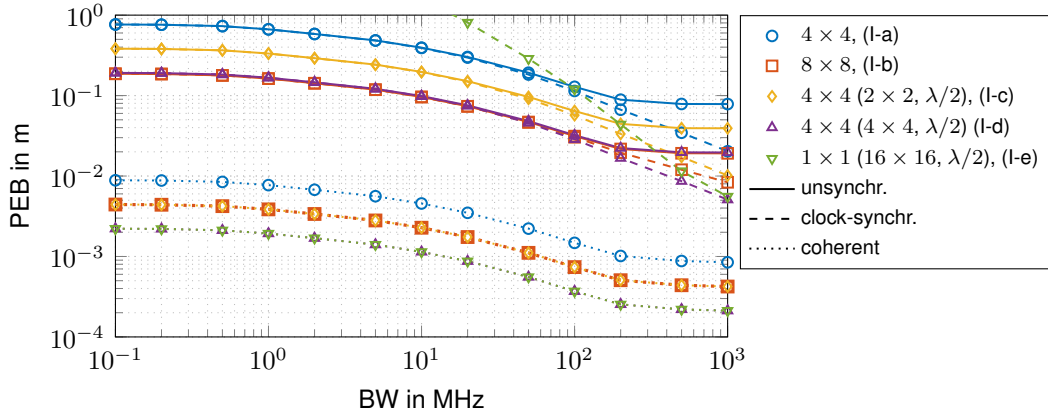
Regarding the achievable gain due to being clock-synchronized, it is interesting to note that only at large bandwidth values, a performance gain can be achieved. This can be attributed to the fact that at large bandwidth values, first the information provided by the range measurements starts to dominate, and second the overlap between DMC and LOS is reduced and the estimation of the clock offset improves. This improvement can be seen in Figure 3.1a at bandwidth values above 100 MHz, where the PEB again approaches the linear trend of the AWGN-only bounds, before approaching a constant value.

Comparing all three bounds curves in Fig. 3.1, one observes that the points where the synchronization configurations CLK deviate noticeably from UN occur at roughly  $B = 100$  MHz. The location of this point can be linked to the definition of the DMC, which was modeled to have a delayed onset of 1 m w.r.t. the LOS, which will be a similar delay as the duration of the transmit pulse/signal at 100 MHz. Consequently, the reducing overlap of DMC and LOS allows for a better estimate of the LOS phase, which is modeled to correspond to the phase offset. A similar effect can also be observed when analyzing AOA estimation in DMC environments (c.f., [14]).

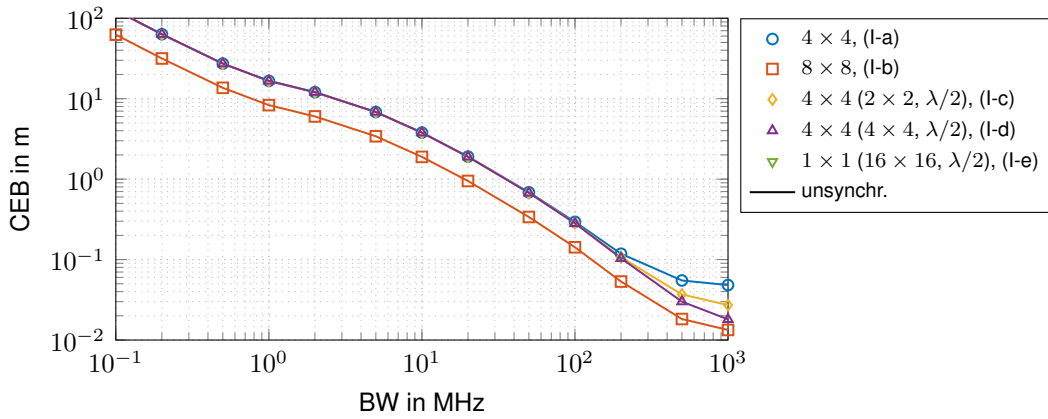
### 3.2.2 Performance in an Exemplary Environment

Next, we examine the system performance when keeping the number of total antennas fixed, but distributing them in different geometric configurations and varying separations into subarrays. The corresponding layouts are summarized in Table 3.1 as (II-a) to (IV-d), for a total number of CSPs  $J = \{1, 2, 4\}$ . The results are shown in Fig. 3.2 and 3.3. To highlight the resulting effect on the achievable accuracy, we plot the PEB evaluated over a spatial grid in an exemplary environment represented as a rectangular room of dimensions  $5 \text{ m} \times 9 \text{ m} \times 3.6 \text{ m}$ . Note that while walls are indicated, we solely model DMC with the same statistical properties as before. Furthermore, note that the colorbar scaling varies to allow for easier visualization. In addition to the PEB also the configuration at the corresponding CSPs is plotted.

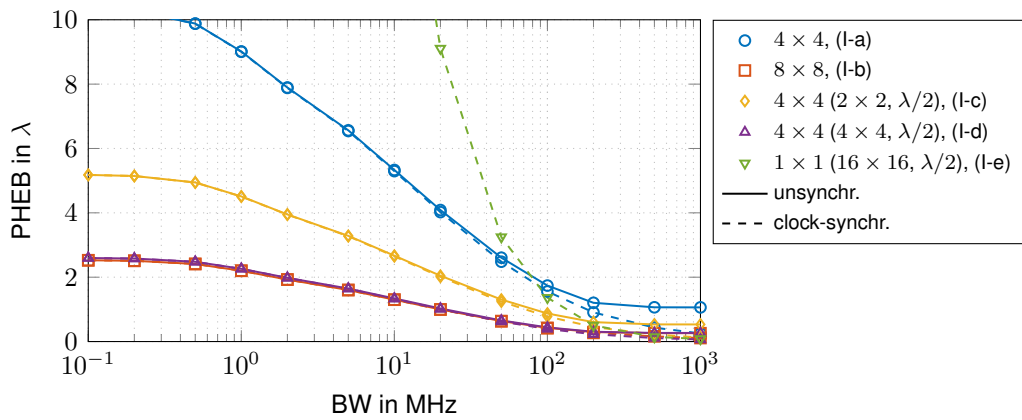
Figure 3.2 shows the spatial distribution when employing  $J = 4$  CSPs, positioned in the center of the corresponding walls of the environment. The top row (Fig. 3.2a-3.2c) shows all three synchronization levels for configuration (II-a), the middle row (Fig. 3.2d-3.2f) for configuration (II-b)



(a)



(b)



(c)

Figure 3.1: PEB (a), CEB (b) and PHEB (c) evaluated for varying system bandwidth  $B$  values for system configurations (I-a) to (I-e) from Table 3.1.

with the subarrays spaced farther than  $\lambda/2$  apart and the bottom for (Fig. 3.2g-3.2i) for configuration (II-e). The resulting distribution of the PEB depends on the distance to the corresponding CSP/subarray due to distance dependency of the angle estimation accuracy [18, 14], in addition to the direction dependency relative to each subarray, i.e., the estimation accuracy is worst from “endfire” direction. The latter manifests in the reduced performance in the corners of the investigated environment, where the PEB increases above 10 cm for the UN case. The increased spacing between subarrays results in general in a performance increase, due to the increased aperture. By considering the full system to be clock synchronized (CLK) the performance is again increased, with little change to the general shape of the PEB distribution. For the coherent case (COH) the large aperture results in a PEB well below 5 mm, which is, while unrealistic in an actually deployed system, still the ideal performance. When keeping the increased subarray spacing but trading the number of subarrays for the larger ( $8 \times 8$ ) subarrays, the PEB drops below 5 cm for most of the environment. A byproduct of the fewer and larger subarrays is the fact that the clock estimation cost is reduced, with noticeably less improvement achievable when assuming CLK. With the large aperture in COH, the improvement is limited, as the large spatial distribution outweighs the rather small increase in terms of the subarray aperture.

An improvement of the spatial distribution while keeping the smaller ( $4 \times 4$ ) subarrays can be achieved by increasing the per-CSP aperture, stacking all subarrays side by side (horizontally), see Figure 3.3a-3.3a, or when using  $J = 2$  by increasing the horizontal aperture, see Figure 3.3d-3.3f. While this gives the most desirable distribution in the horizontal plane that was evaluated, the vertical performance will be worse. Depending on the target use case, different configurations should be considered for specific scenarios, e.g., when positioning mobile robots that will mostly move along the horizontal axis, or for localizing goods in high shelves, which would require higher resolution along the vertical axis.

Lastly, the performance in terms of the PEB for a single CSP will drastically reduce with increasing distance, as the angle contribution that provides the highest position information in close proximity decays fast, with the lower distance resolution dominating the positioning performance in the “array far field” of the CSP. In contrast to the scenarios encompassing more than one CSP, the improvement in CLK state is much larger, showing that accurate synchronization will be a key ingredient to achieve a high long-range positioning accuracy. As before, considering this effect can be important in system design, e.g., in use cases where “close” proximity to CSPs cannot always be guaranteed, or is not possible due to structural characteristics.

An alternative illustration of the PEB is given in Fig. 3.4, showing CDF plots of the PEB distributions for the scenarios for (II-a) to (IV-d) from Table 3.1. Note that the abscissa in the subplots show different range for improved illustration. Comparing the simulation results obtained for different numbers of CSPs shows that even though the number of antennas is fixed to  $N_{\text{total}} = 1024$ , the governing factor for the performance is the geometric distribution of the CSPs as well as the configuration of the subarrays. While the COH state again shows the high performance seen in Figures 3.2 and 3.3, it clearly shows that the subarray spacing can serve as an important factor to increase the performance. What is commonly termed *spatial* aliasing, i.e., spacing array elements farther apart than  $\lambda/2$ , introduces ambiguities in the array response when working with a single array [14]. As the subarrays themselves still employ an inter-element spacing of  $\lambda/2$ , the increased aperture gives a performance increase (e.g., compare (II-a) and (II-b) in Figure 3.4a) without the undesirable side effect of ambiguities, while the use of smaller subarrays still poses to be a limiting factor (e.g., compare (II-a) and (II-c) in Figure 3.4a). It is furthermore important to note, that the effect of the clock offset reduces the performance when the total system aperture, i.e., meaning the aperture of the CSPs, decreases. This can be seen when comparing Figure 3.4a

( $J = 4$ ) and 3.4c ( $J = 1$ ), where for (IV-a) only 20% of the PEB values are below 10 cm, whereas for (II-a) approx. 90% are, with the former employing all subarrays at a single CSP. Nonetheless, the performance increase in terms of a reduction of the PEB is much stronger when employing all subarrays at a single CSP location. When assuming all subarrays to be clock synchronized (CLK), the spacing of the subarrays has hardly any influence, with 70% for  $4 \times 4$  subarrays (IV-a) of the analyzed grid points showing a PEB below 10 cm, and 90% for  $8 \times 8$  subarrays (IV-a).

### 3.3 Conclusion

The numerical analysis of the bounds has shown the trade-offs that can be expected from the RW infrastructure, focusing on a subarray-based configuration of each of the CSPs. This approach has already been employed in D1.2 [2] for channel modeling, shown that it is feasible to capture the SMC visibility over an array with a large aperture, i.e., covering a large surface area, by processing subarrays separately with super-resolution algorithms that achieve a high accuracy. In addition, small subarrays allow for efficient implementation of said algorithms and allows to efficiently distribute computation resources.

This is further analyzed in in Chapter 4, where two candidate algorithms suitable for positioning based on subarrays are described. An EKF-based algorithm aims to perform joint clock offset estimation and positioning (Section 4.3) and a graph-based algorithm is used to perform data fusion of (simulated) measurements, using measurements modeled to correspond to what can be obtained from a multipath super-resolution channel estimation algorithm applied to subarrays (Section 4.2). In addition to these, the reciprocity calibration performance is analyzed in the context of a distributed MIMO system (Section 4.1).

Regarding the formation and performance of federations (see D2.1 [1]) as well as regarding the processing distribution, a subarray-based approach is also favorable as it increases the flexibility of CSPs, e.g., by having variable coverage regions, or by improving power consumption by employing only subsets of the available subarrays for positioning or communication.

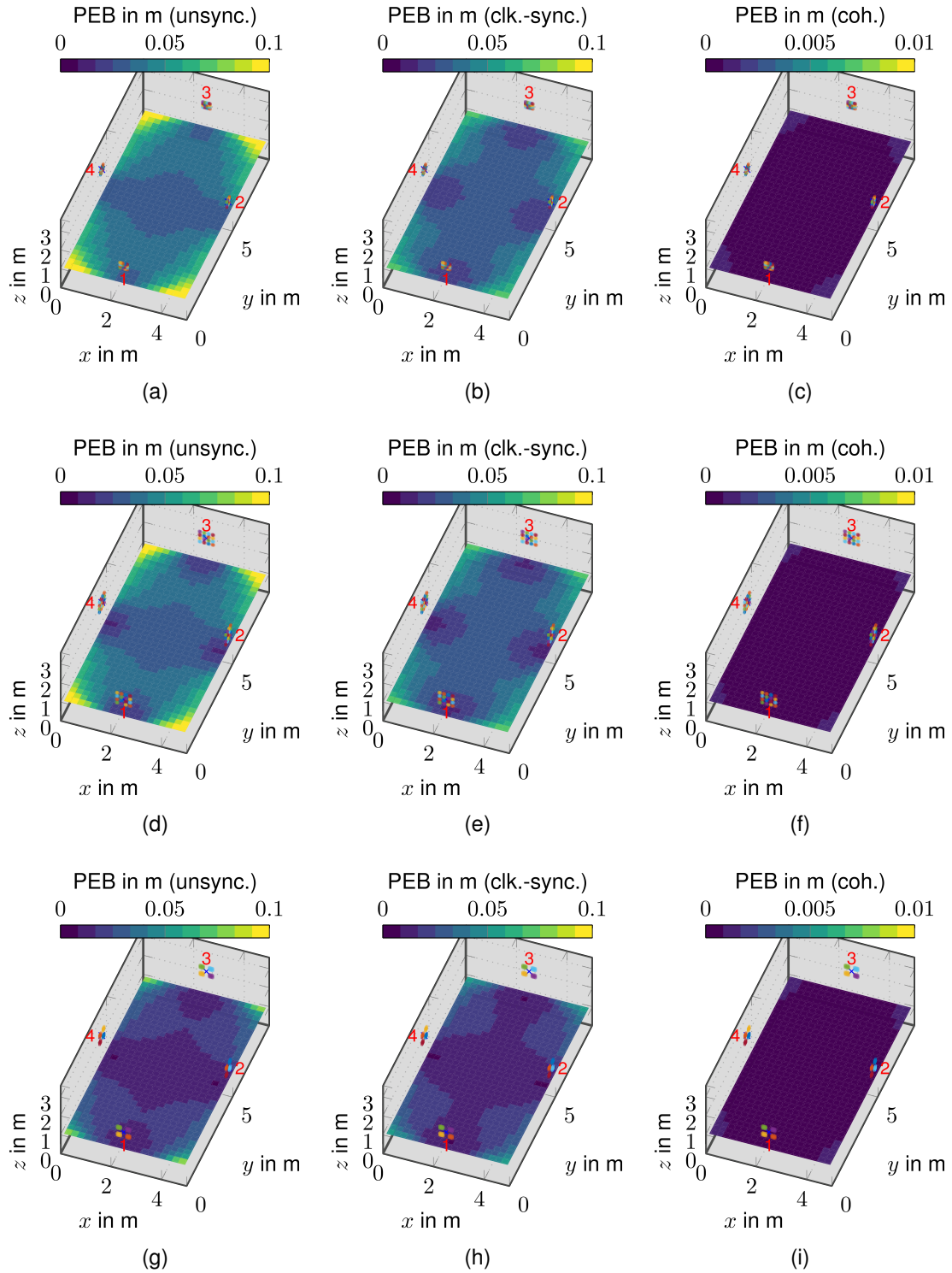


Figure 3.2: PEB distribution for configurations (II-a) in (a)-(c), (II-b) in (d)-(f) and (II-d) in (g)-(i) specified in Table 3.1.

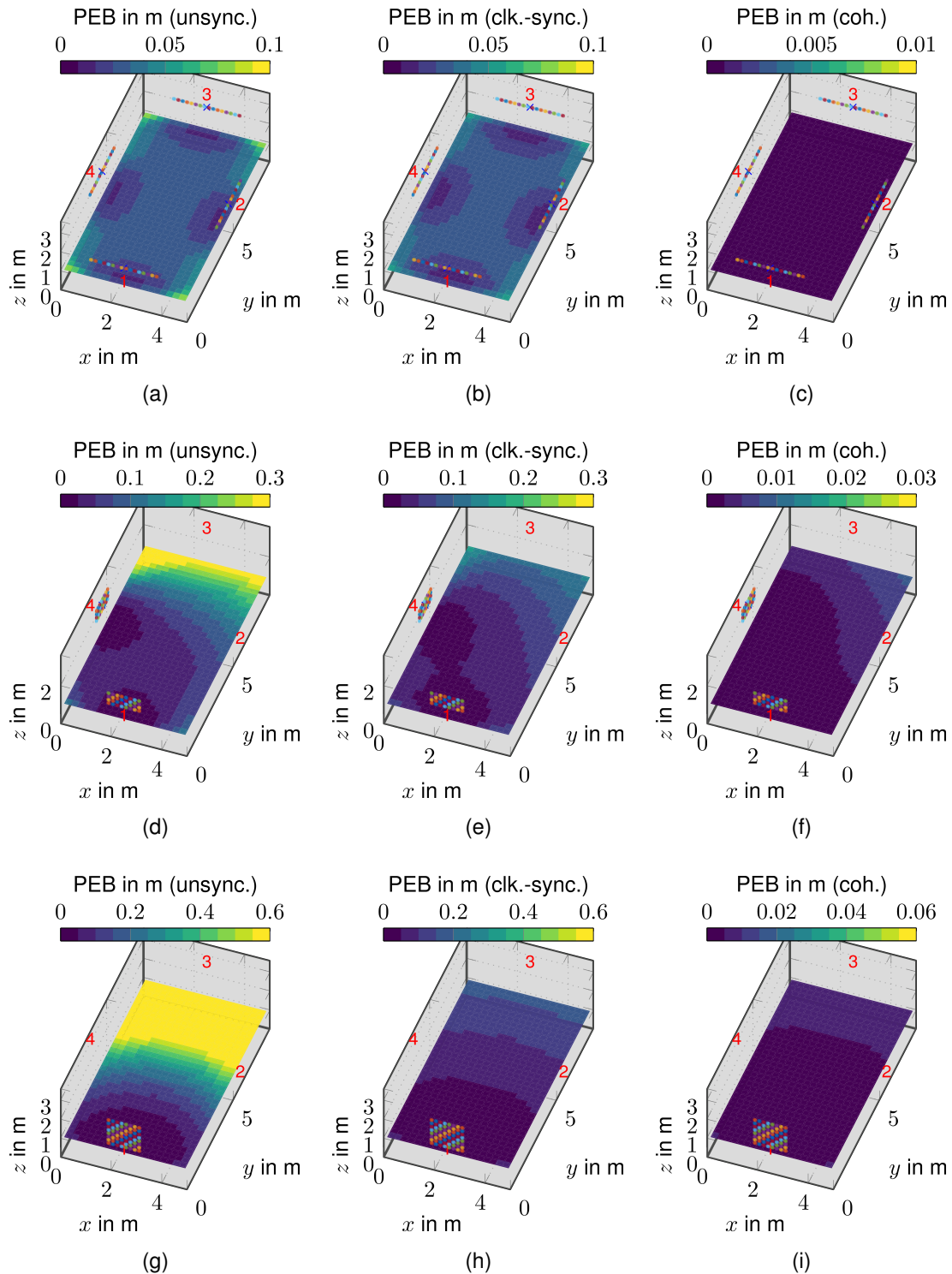
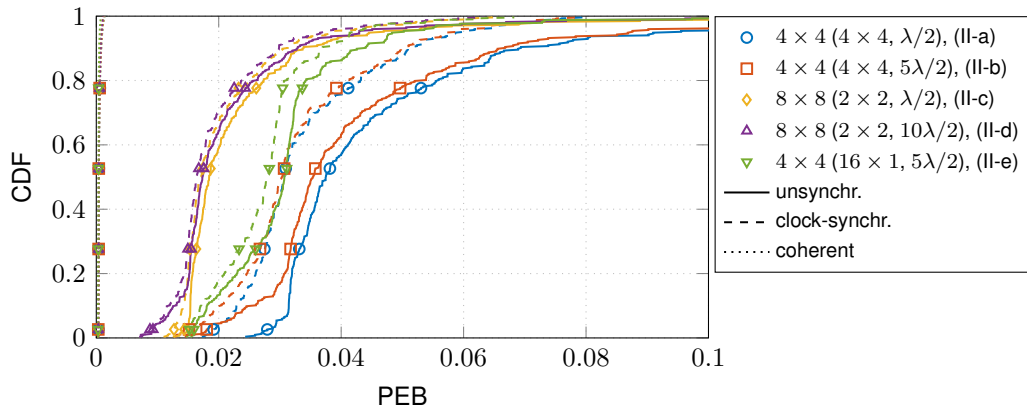
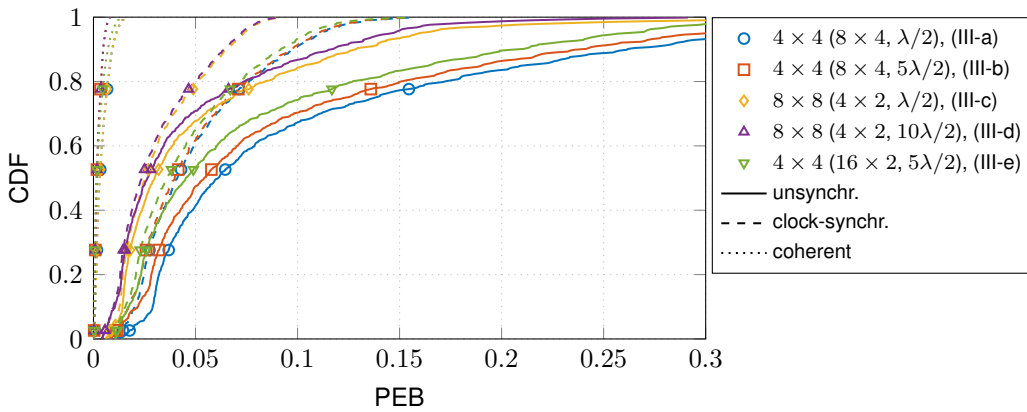


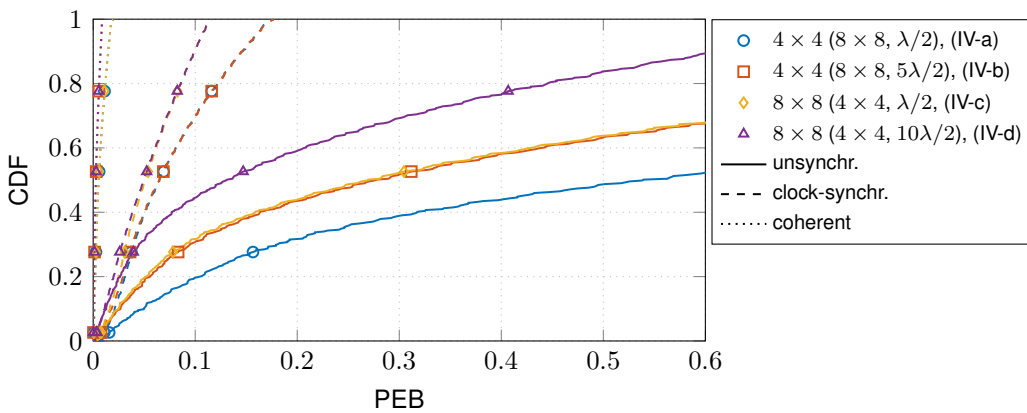
Figure 3.3: PEB distribution for configurations (II-e) in (a)-(c), (III-b) in (d)-(f) and (IV-b) in (g)-(i) from Table 3.1.



(a)



(b)



(c)

Figure 3.4: CDF curves for the different system configurations outlined in Tab. 3.1, as well as for different the synchronization states. In (a) there are  $J = 4$  CSPs, in (b)  $J = 2$  CSPs, and in (c) a single CSP is used ( $J = 1$ ). Note that the total number of antennas remains fixed as  $N_{\text{total}} = 1024$ .

## Chapter 4

# Algorithms for Calibration, Synchronization and Positioning

This chapter introduces candidate algorithms covering the topics of reciprocity calibration, synchronization and positioning important for various fields of application and use-cases of the RW infrastructure.

Reciprocity calibration is important to enable coherent operation of distributed MIMO systems. An algorithm taking non-reciprocal RF chains into account is discussed in Section 4.1. In Section 4.3, an EKF-based positioning and synchronization algorithm is adapted from an existing algorithm proposed in [10] to work on the subarray level, as it can cope with a (slowly) time varying clock offset between subarrays. To work in non-stationary propagation scenarios, e.g., in non-line-of-sight (NLOS) condition, it is extended with a simple ray tracer that allows to employ environment information, aiming to increase the robustness. In Section 4.2, a graph-based algorithm for channel tracking proposed in [19], is adapted to perform data fusion of (reasonably closely-spaced) subarrays of a single CSP, allowing to estimate SMCs and considering the limited visibility of components for the separate subarrays for which the measurements are fused.

### 4.1 Reciprocity Calibration in Distributed Massive MIMO for Coherent Operation

Distributed Massive MIMOs, also known as cell-free massive MIMOs, is an emerging technology and a candidate for 6G multi-antenna systems [20]. It relies on phase-coherent operation of large numbers of antenna panels, which are distributed over a larger area. Two important implementations are RadioStripes (with antennas along a cable) and large intelligent surfaces, e.g. RadioWeaves [21] (with antennas integrated into walls and other objects). It is foreseen that practical distributed massive systems will be built of CSPs, and that each CSP comprise multiple antennas elements (creating a, so-called, antenna panel), and where the CSPs are interconnected with one another via a central processing unit (CPU). The preferred operation is in time-division duplexing mode, where uplink-downlink reciprocity of the radio channel can be exploited in order to estimate the downlink channels using uplink pilots, much like in conventional massive MIMOs. This operation mode is typically referred to as reciprocity-based operation.

However, the assumption of uplink-downlink radio channel reciprocity is only true in practice to a certain extent. More specifically, even though it is well known that the propagation channel

is reciprocal, the transceiver radio frequency (RF) units sitting at both ends of the radio link are generally not. Thus, transceiver calibration is required in order to be possible for the system to operate in the reciprocity-based mode. There exist different types of calibration approaches in the literature that restore some degree of reciprocity of a wireless link. Some approaches rely on 1) bi-directional signaling between UEs and the CSP, other approaches rely on 2) internal calibration cable networks at the CSP end of the link, and other approaches rely on 3) over-the-air signaling between pairs of antennas of the CSP. However, for the setup of a distributed massive MIMO system, only the third approach is suitable since the system should typically not rely on the quality of the link to UEs for calibration, nor is it suitable to install cables between distributed CSPs with the sole purpose of system calibration. Similar problems are covered in literature in [22, 23].

However, the calibration approaches in the literature address system setups where each transceiver to be calibrated is associated with a single antenna element, i.e. they address calibration of fully-digital systems. In addition, it is foreseen that practical distributed massive MIMO systems will be built of multiple CSPs, and that each CSP comprises multiple antenna elements. Such CSP's multiple antennas are controlled via (tunable) analog beamforming, mainly implemented in the RF stage of the radio. The key insight for distributed massive MIMO calibration is that the possibility of properly tuning, and hence sweeping, such beamformers provide extra degrees of freedom to the system which can be exploited to obtain a multitude of over-the-air measurements for calibration purposes.

We study reciprocity calibration of distributed massive MIMO systems [24]. In particular, we write a model for the calibration setup, where a joint beam scanning procedure is executed by all CSPs of the network in order to collect measurements for calibration. We lay out the maximum-likelihood (ML) cost function for the calibration problem at hand, and propose a computationally-efficient alternating optimization procedure. We show that the optimization procedure is guaranteed to converge. Via Monte-Carlo simulations, we verify performance enhancements of the proposed method, compared to straightforward applications of state-of-the-art calibration schemes in the context of distributed massive MIMO.

#### 4.1.1 Problem Description

For illustrative but non-limiting purposes, assume a narrowband distributed massive MIMO link with  $L$  single-antenna UEs on the other end, and  $M$  transceiver chains at the other end, e.g., assume that each antenna chain is associated with a distinct CSP. Assuming a noiseless channel for the moment, the  $M \times L$  uplink narrowband radio channel  $\mathbf{H}_{UL}$ , representing e.g. an orthogonal frequency division multiplexing (OFDM) subcarrier, is modelled as

$$\mathbf{H}_{UL} = \mathbf{R}_{CSP} \mathbf{H} \mathbf{T}_{UE}, \quad (4.1)$$

where  $\mathbf{H}$  is a matrix comprising all channels effects occurring between the transmitter and receiver chains. For example, in fully-digital beamforming systems, the channel matrix  $\mathbf{H}$  typically denotes the propagation channel [22]. The matrix  $\mathbf{T}_{UE} = \text{diag}(t_1^{UE}, \dots, t_L^{UE})$  is a diagonal matrix where each diagonal entry models the complex gain of each UE's transmitter chain, and  $\mathbf{R}_{CSP} = \text{diag}(r_1^{CSP}, \dots, r_M^{CSP})$  is a diagonal matrix where each diagonal entry models the complex gain of each CSP's receiver chain.

Within the same time/frequency coherence interval, the associated downlink channel is given by

$$\mathbf{H}_{DL} = \mathbf{R}_{UE} \mathbf{H} \mathbf{T}_{CSP}, \quad (4.2)$$

where  $\mathbf{T}_{\text{CSP}} = \text{diag}(t_1^{\text{CSP}}, \dots, t_M^{\text{CSP}})$  and  $\mathbf{R}_{\text{UE}} = \text{diag}(r_1^{\text{UE}}, \dots, r_L^{\text{UE}})$  model the associated transmitter and receiver gains of each UE and each CSP, respectively.

Note that the channel matrix  $\mathbf{H}$  is assumed to be reciprocal. However, the end-to-end radio channel is not reciprocal, i.e.,  $\mathbf{H}_{\text{UL}} \neq \mathbf{H}_{\text{DL}}^{\text{T}}$ , where  $(\cdot)^{\text{T}}$  denotes the transpose operator. This is because the gains of the transceiver circuitries are not reciprocal (e.g.,  $\mathbf{T}_{\text{CSP}} \neq \mathbf{T}_{\text{UE}}$ ). Due to this non-reciprocity aspect, it is not immediately obvious how downlink transmission can be performed based on channel estimates obtained from uplink pilot signals.

To indicate how to address the challenge with the non-reciprocal transceiver terms, let's assume for now that the CSP side of the link has knowledge of the following matrix

$$\mathbf{C} = \text{diag}(c_1, \dots, c_M) = \mathbf{T}_{\text{CSP}} (\mathbf{R}_{\text{CSP}})^{-1}, \quad (4.3)$$

up to an a non-zero complex-valued unknown scaling term  $\alpha$ .

Via uplink pilot signals, the CSP can estimate  $\mathbf{H}_{\text{UL}}$ . If the CSPs wants to jointly perform, e.g. ZF transmission to the UEs, they do so by the computing the Moore–Penrose inverse of  $\mathbf{H}_{\text{UL}}^{\text{T}}$ , namely

$$\mathbf{P} = \mathbf{H}_{\text{UL}}^* \left( \mathbf{H}_{\text{UL}}^{\text{T}} \mathbf{H}_{\text{UL}}^* \right)^{-1}, \quad (4.4)$$

where  $(\cdot)^*$  denotes element-wise complex conjugation. However, since the matrix  $\mathbf{P}$  was computed via uplink signals, it cannot be directly used as a downlink precoder since it is not matched to the (non-reciprocal) downlink channel  $\mathbf{H}_{\text{DL}}$ . To solve this, each CSP multiplies its pre-coded signals with its associated entry of  $(\alpha \mathbf{C})^{-1}$ . More specifically, the pre-coded signal at transceiver  $m$  is multiplied with  $c_m$ , with  $1 \leq m \leq M$ . With that, the effective downlink channel  $\mathbf{H}'_{\text{DL}}$  is written as

$$\begin{aligned} \mathbf{H}'_{\text{DL}} &= \mathbf{H}_{\text{DL}} \alpha^{-1} \mathbf{C}^{-1} \mathbf{P} \\ &= \mathbf{H}_{\text{DL}} \alpha^{-1} \mathbf{C}^{-1} \mathbf{H}_{\text{UL}}^* \left( \mathbf{H}_{\text{UL}}^{\text{T}} \mathbf{H}_{\text{UL}}^* \right)^{-1} \\ &= \mathbf{H}_{\text{DL}} \alpha^{-1} \mathbf{C}^{-1} \mathbf{R}_{\text{CSP}}^* \mathbf{H}^* \mathbf{T}_{\text{UE}}^* \left( \mathbf{T}_{\text{UE}} \mathbf{H}^{\text{T}} |\mathbf{R}_{\text{CSP}}|^2 \mathbf{H}^* \mathbf{T}_{\text{UE}}^* \right)^{-1} \\ &= \mathbf{H}_{\text{DL}} \alpha^{-1} \mathbf{T}_{\text{CSP}}^{-1} |\mathbf{R}_{\text{CSP}}|^2 \mathbf{H}^* \mathbf{T}_{\text{UE}}^* \left( \mathbf{T}_{\text{UE}} \mathbf{H}^{\text{T}} |\mathbf{R}_{\text{CSP}}|^2 \mathbf{H}^* \mathbf{T}_{\text{UE}}^* \right)^{-1} \\ &= \mathbf{H}_{\text{DL}} \alpha^{-1} \left( \mathbf{T}_{\text{CSP}} \right)^{-1} \left( \mathbf{H}^{\text{T}} \right)^{\dagger} \left( \mathbf{T}_{\text{UE}} \right)^{-1} \\ &= \alpha^{-1} \mathbf{R}_{\text{UE}} \mathbf{H}^{\text{T}} \mathbf{T}_{\text{CSP}} \left( \mathbf{T}_{\text{CSP}} \right)^{-1} \left( \mathbf{H}^{\text{T}} \right)^{\dagger} \left( \mathbf{T}_{\text{UE}} \right)^{-1} \\ &= \alpha^{-1} \mathbf{R}_{\text{UE}} \left( \mathbf{T}_{\text{UE}} \right)^{-1}, \end{aligned} \quad (4.5)$$

which is a diagonal channel matrix with unknown diagonal entries. The operator  $(\cdot)^{\dagger}$  denotes the Moore–Penrose inverse, and  $|\cdot|^2$  denotes element-wise squared absolute value.

Such unknown diagonal entries can be obtained using only one downlink reference signal, which is beamformed in the downlink towards all UEs, using the calibrated channels. Thus,  $N_p$  uplink pilot signals plus one downlink reference signal are sufficient to conduct all training needed for this type of calibrated reciprocity-based transmissions. This results in much less training overhead compared to explicit downlink channel estimation.

In conclusion, the knowledge of the matrix  $\mathbf{C}$  allows coherent transmissions, e.g. ZF downlink transmissions, with no inter-user interference over what is effectively a calibrated uplink/downlink channel setup. The diagonal matrix  $\mathbf{C}$  can thus be interpreted as a calibration matrix, and thus we are interested to estimate its diagonal elements.

### 4.1.2 Calibration Signal Model

In this section we propose our method to estimate the calibration matrix  $\mathbf{C}$ . We note that the novelty of our proposal lies in the fact that the effective channel  $\mathbf{H}$  in (4.1) is not only made of the propagation channel, as in prior calibration works in massive MIMOs, but is also comprised by a beamforming matrix  $\mathbf{W}$ . More specifically

$$\mathbf{H} = \mathbf{W}\mathbf{H}_p, \quad (4.6)$$

where  $\mathbf{H}_p$  models the propagation uplink channel and each CSP's beamformer is given by each row of  $\mathbf{W}$ . The possibility of steering such beamformers provides extra degrees of freedom to the system which can be exploited to obtain a multitude of measurements for calibration purposes. We elaborate on this concept in the current and next sub-sections.

Our measurement procedure relies on a joint beam sweep by all network CSPs. That is, a CSP acts as a transmitter and scans each of its  $N_b$  beams while the other  $J - 1$  CSPs act as receivers and scan each of their  $N_b$  beams as well. (For simplicity, assume that all transmitters and receivers are capable of grid-of-beams beamforming, and that  $N_b$  denotes the number of transmit and receive beams at all CSPs). This process is repeated with another CSP acting as transmitter, and it stops when all CSPs have transmitted. The number of measurements resulting from this extensive beam sweeping procedure is therefore  $JN_b^2$ . (We note that other sub-cases where a partial beam scanning is done are also possible, but we keep the formulation to be that of a full-beam scanning in the chapter since it represents the general case.)

Set  $r_i \triangleq r_i^{\text{CSP}}$  and  $t_i \triangleq t_i^{\text{CSP}}$  for notation convenience. With that, the signals collected by a receiving CSP, say CSP  $j$  with  $1 \leq j \leq J$ , after another CSP, say CSP  $i$  with  $1 \leq i \leq J$  and  $i \neq j$ , scanned its beam, can be written as

$$\mathbf{Y}_{i,j} = r_i \mathbf{F}_i^T \mathbf{H}_p^{i,j} \mathbf{B}_j t_j + \mathbf{N}_{i,j}, \quad (4.7)$$

where  $\mathbf{N}_{i,j}$  is a matrix modelling receive noise and its entries are independent and identically distributed zero-mean circularly symmetric complex-valued Gaussian variables with variance  $\sigma^2$ , and the symmetric matrix  $\mathbf{H}_p^{i,j}$  denotes the reciprocal propagation channel from all antenna elements of CSP  $j$  to all antenna elements of CSP  $i$ . The matrix  $\mathbf{B}_j = [\mathbf{b}_j(1) \dots \mathbf{b}_j(N_b)]$  denotes the transmit codebook matrix at CSP  $j$  and contains all possible  $N_b$  beams of the transmit beamformer. Similarly,  $\mathbf{F}_i = [\mathbf{f}_i(1) \dots \mathbf{f}_i(N_b)]$  denotes the receive codebook matrix which contains all possible beams of the receive beamformer. (Note the relation between  $\mathbf{W}$  in (4.6), and the codebook matrices in (4.7), e.g.  $\mathbf{B}_j$ . To explain, the  $j$ -th row of  $\mathbf{W}$  consists of the beam being used by the  $j$ -th CSP for downlink data transmission, which is a given column of the transmit grid-of-beams matrix  $\mathbf{B}_j$ ). The matrix  $\mathbf{Y}_{i,j}$  contains the measurements resulting from all combinations of beam pairs.

Based on (4.7), the vectorized signal model is

$$\begin{aligned} \text{vec}(\mathbf{Y}_{i,j}) &= \text{vec}(r_i \mathbf{F}_i^T \mathbf{H}_p^{i,j} \mathbf{B}_j t_j) + \text{vec}(\mathbf{N}_{i,j}) \\ &= \text{vec}\left(r_i r_j \mathbf{F}_i^T \mathbf{H}_p^{i,j} \mathbf{B}_j \frac{t_j}{r_j}\right) + \text{vec}(\mathbf{N}_{i,j}) \\ &= r_i r_j \text{vec}(\mathbf{F}_i^T \mathbf{H}_p^{i,j} \mathbf{B}_j) c_j + \text{vec}(\mathbf{N}_{i,j}) \\ &= r_i r_j \begin{bmatrix} \mathbf{F}_i^T \mathbf{H}_p^{i,j} & \mathbf{0} & \mathbf{0} \\ \mathbf{0} & \ddots & \mathbf{0} \\ \mathbf{0} & \mathbf{0} & \mathbf{F}_i^T \mathbf{H}_p^{i,j} \end{bmatrix} \text{vec}(\mathbf{B}_j) c_j + \text{vec}(\mathbf{N}_{i,j}), \end{aligned} \quad (4.8)$$

where the operator  $\text{vec}(\cdot)$  stacks the columns of its matrix input. Each CSP uses the same beams for transmission and reception, e.g.,  $\mathbf{B}_i = \mathbf{F}_i$  and  $\mathbf{B}_j = \mathbf{F}_j$ , this assumption is motivated later on. We also write the reciprocal propagation matrix as  $\mathbf{H}_p \triangleq \mathbf{H}_p^{i,j} = (\mathbf{H}_p^{j,i})^\top$  for simplicity. With that, it follows that the double-directional signal model between CSP  $i$  and CSP  $j$ , can be written as

$$\begin{aligned}
\bar{\mathbf{Y}}_{i,j}^* &= \begin{bmatrix} \text{vec}(\mathbf{Y}_{i,j}) \\ \text{vec}(\mathbf{Y}_{j,i}^\top) \end{bmatrix} \\
&= \begin{bmatrix} r_i r_j \begin{bmatrix} \mathbf{F}_i^\top \mathbf{H}_p^{i,j} & \mathbf{0} & \mathbf{0} \\ \mathbf{0} & \ddots & \mathbf{0} \\ \mathbf{0} & \mathbf{0} & \mathbf{F}_i^\top \mathbf{H}_p^{i,j} \end{bmatrix} \text{vec}(\mathbf{B}_j) c_j \\ r_j r_i \begin{bmatrix} \mathbf{F}_i^\top \mathbf{H}_p^{i,j} & \mathbf{0} & \mathbf{0} \\ \mathbf{0} & \ddots & \mathbf{0} \\ \mathbf{0} & \mathbf{0} & \mathbf{F}_i^\top \mathbf{H}_p^{i,j} \end{bmatrix} \text{vec}(\mathbf{B}_j) c_i \end{bmatrix} + \begin{bmatrix} \text{vec}(\mathbf{N}_{i,j}) \\ \text{vec}(\mathbf{N}_{j,i}^\top) \end{bmatrix} \\
&= \begin{bmatrix} \mathbf{e}_{i,j} & \mathbf{0} \\ \mathbf{0} & \mathbf{e}_{i,j} \end{bmatrix} \begin{bmatrix} c_j \\ c_i \end{bmatrix} + \begin{bmatrix} \text{vec}(\mathbf{N}_{i,j}) \\ \text{vec}(\mathbf{N}_{j,i}^\top) \end{bmatrix} \\
&= \begin{bmatrix} \mathbf{e}_{i,j} & \mathbf{0} \\ \mathbf{0} & \mathbf{e}_{i,j} \end{bmatrix} \begin{bmatrix} c_j \\ c_i \end{bmatrix} + \bar{\mathbf{N}}_{i,j} \tag{4.9}
\end{aligned}$$

Based on the bi-directional model obtained in (4.9), reciprocity calibration of a multiple CSPs can be carried out.

We note that the transmit and receive codebooks, namely  $\mathbf{B}_j$  and  $\mathbf{F}_i$ , may be tall matrices (i.e. with more rows than columns) or square matrices (e.g. DFT matrices). The exact setting of such codebooks is not needed to be known by the system to perform calibration. The only assumption required is that the same CSP beams are used for transmission and reception (i.e.,  $\mathbf{B}_i = \mathbf{F}_i$ ), otherwise  $\mathbf{e}_{i,j} \neq \mathbf{e}_{j,i}$  and (4.9) may not be identifiable.

### Maximum-Likelihood Calibration of a 3-CSP Network

Next, we exemplify the case where  $J = 3$  CSPs are being jointly calibrated for reciprocity – the generality of the approach scales for any number of CSPs. With that, the joint bi-directional signal model may be written as

$$\bar{\mathbf{Y}} = \mathbf{C}_{\text{eq}} \begin{bmatrix} \mathbf{e}_{1,2} \\ \mathbf{e}_{1,3} \\ \mathbf{e}_{2,3} \end{bmatrix} + \bar{\mathbf{N}} \tag{4.10}$$

or

$$\bar{\mathbf{Y}} = \mathbf{E}_{\text{eq}} \mathbf{c} + \bar{\mathbf{N}}, \tag{4.11}$$

where  $\bar{\mathbf{Y}} = [\bar{\mathbf{Y}}_{1,2}^\top \bar{\mathbf{Y}}_{1,3}^\top \bar{\mathbf{Y}}_{2,3}^\top]^\top$ ,  $\bar{\mathbf{N}} = [\bar{\mathbf{N}}_{1,2}^\top \bar{\mathbf{N}}_{1,3}^\top \bar{\mathbf{N}}_{2,3}^\top]^\top$ ,  $\mathbf{c} = [c_1 \ c_2 \ c_3]^\top$ , and

$$\mathbf{E}_{\text{eq}} = \begin{bmatrix} \mathbf{e}_{1,2} & \mathbf{0} & \mathbf{0} \\ \mathbf{e}_{1,3} & \mathbf{0} & \mathbf{0} \\ \mathbf{0} & \mathbf{e}_{1,2} & \mathbf{0} \\ \mathbf{0} & \mathbf{e}_{2,3} & \mathbf{0} \\ \mathbf{0} & \mathbf{0} & \mathbf{e}_{1,3} \\ \mathbf{0} & \mathbf{0} & \mathbf{e}_{2,3} \end{bmatrix}, \tag{4.12}$$

and

$$\mathbf{C}_{\text{eq}} = \begin{bmatrix} \text{diag}(c_1, \dots, c_1) & \mathbf{0} & \mathbf{0} \\ \text{diag}(c_2, \dots, c_2) & \mathbf{0} & \mathbf{0} \\ \mathbf{0} & \text{diag}(c_1, \dots, c_1) & \mathbf{0} \\ \mathbf{0} & \text{diag}(c_3, \dots, c_3) & \mathbf{0} \\ \mathbf{0} & \mathbf{0} & \text{diag}(c_2, \dots, c_2) \\ \mathbf{0} & \mathbf{0} & \text{diag}(c_3, \dots, c_3) \end{bmatrix}. \quad (4.13)$$

Note that  $\bar{\mathbf{Y}}$  and  $\bar{\mathbf{N}}$  are matrices with the same dimensions of  $\bar{\mathbf{Y}}$  and  $\bar{\mathbf{N}}$ , but with elements re-ordered. The re-ordering can be inferred from the structure of  $\mathbf{E}_{\text{eq}}$  and  $\mathbf{c}$  in (4.11).

To estimate the calibration coefficients  $\mathbf{c}$ , a maximum likelihood cost function can be written. From an optimization point of view, it is equivalent to minimizing the squared residuals, namely,

$$J_{\text{ML}}(\mathbf{E}_{\text{eq}}, \mathbf{c}) = \|\bar{\mathbf{Y}} - \mathbf{E}_{\text{eq}}\mathbf{c}\|^2, \quad (4.14)$$

where the operator  $\|\mathbf{A}\|^2$  denotes the squared Frobenius norm of matrix  $\mathbf{A}$ .

### An Alternating Optimization Procedure

Our task now is to find the values of the calibration coefficients  $\mathbf{c}$  and the nuisance matrix  $\mathbf{E}_{\text{eq}}$  that minimize  $J_{\text{ML}}(\mathbf{E}_{\text{eq}}, \mathbf{c})$ . Note that there is no obvious closed-form solution for  $\mathbf{E}_{\text{eq}}$  and  $\mathbf{c}$  since the cost function is not quadratic on the joint parameter space. However, by fixing one part of the parameter space, e.g.  $\mathbf{E}_{\text{eq}}$ , a closed-form solution exists for the remaining part of the parameter space, e.g.,  $\mathbf{c}$ , and it can trivially be obtained via

$$\hat{\mathbf{c}} = \mathbf{E}_{\text{eq}}^\dagger \bar{\mathbf{Y}}, \quad (4.15)$$

where  $\mathbf{A}^\dagger$  denotes the Moore–Penrose inverse of  $\mathbf{A}$ . With that, one can use alternative optimization techniques to find suitable estimates for  $\mathbf{E}_{\text{eq}}$  and  $\mathbf{c}$ . More specifically, letting the estimates obtained at the  $n$ -th iteration of said alternating procedure be given by  $\hat{\mathbf{c}}^{(n)}$  and  $\hat{\mathbf{E}}_{\text{eq}}^{(n)}$ , the estimates at iteration  $n + 1$  may be obtained via the 2 consecutive steps

$$\hat{\mathbf{c}}^{(n+1)} = \left(\hat{\mathbf{E}}_{\text{eq}}^{(n)}\right)^\dagger \bar{\mathbf{Y}}, \quad (4.16)$$

and

$$\hat{\mathbf{E}}_{\text{eq}}^{(n+1)} = \hat{\mathbf{C}}_{\text{eq}}^{(n+1)} \bar{\mathbf{Y}}. \quad (4.17)$$

where  $\hat{\mathbf{C}}_{\text{eq}}^{(n+1)}$  consist of the matrix  $\mathbf{C}_{\text{eq}}$  with the estimates  $\hat{\mathbf{c}}^{(n+1)}$  in its entries.

### Convergence of the Optimization Procedure

The main aspect to highlight is that the optimization procedure described above is guaranteed to converge either to the global optimum, a local optimum or a saddle point of  $J_{\text{ML}}(\mathbf{E}_{\text{eq}}, \mathbf{c})$ . A simple proof follows.

Prior to iteration  $n + 1$ , inserting the current estimates  $\hat{\mathbf{c}}^{(n)}$  and  $\hat{\mathbf{E}}_{\text{eq}}^{(n)}$  in the cost function, will yield an associated cost of, say,  $C_{(n, n)}$ . Mathematically,

$$J_{\text{ML}}\left(\hat{\mathbf{E}}_{\text{eq}}^{(n)}, \hat{\mathbf{c}}^{(n)}\right) = C_{(n, n)}. \quad (4.18)$$

Note that, in general,  $\hat{\mathbf{c}}^{(n)}$  is not optimized for the current value of  $\hat{\mathbf{E}}_{\text{eq}}^{(n)}$ . This is true if, e.g., both  $\hat{\mathbf{c}}^{(n)}$  and  $\hat{\mathbf{E}}_{\text{eq}}^{(n)}$  are randomly initialized which can be the case when  $n = 0$ , or if  $\hat{\mathbf{c}}^{(n)}$  and  $\hat{\mathbf{E}}_{\text{eq}}^{(n)}$  are obtained via iteration  $n$  the proposed alternating optimization procedure.

The first step of iteration  $n + 1$  of the proposed procedure, optimizes  $\hat{\mathbf{c}}$  while having  $\hat{\mathbf{E}}_{\text{eq}}$  fixed, namely, fixed to its current value is  $\hat{\mathbf{E}}_{\text{eq}}^{(n)}$ . Since this optimization exists in closed form, we are guaranteed to find the optimum (i.e. minimum) value of  $\hat{\mathbf{c}}$  for that particular  $\hat{\mathbf{E}}_{\text{eq}}^{(n)}$ . More specifically,

$$J_{\text{ML}}\left(\hat{\mathbf{E}}_{\text{eq}}^{(n)}, \hat{\mathbf{c}}^{(n+1)}\right) \leq J_{\text{ML}}\left(\hat{\mathbf{E}}_{\text{eq}}^{(n)}, \hat{\mathbf{c}}\right), \quad \forall \hat{\mathbf{c}}, \quad (4.19)$$

and thus the associated cost function value does not increase compared to (4.14). With that, we have

$$J_{\text{ML}}\left(\hat{\mathbf{E}}_{\text{eq}}^{(n)}, \hat{\mathbf{c}}^{(n)}\right) \geq J_{\text{ML}}\left(\hat{\mathbf{E}}_{\text{eq}}^{(n)}, \hat{\mathbf{c}}^{(n+1)}\right). \quad (4.20)$$

The similar holds true when optimizing  $\hat{\mathbf{E}}_{\text{eq}}$  based on  $\hat{\mathbf{c}}^{(n+1)}$ . Namely, since the optimization of  $\hat{\mathbf{E}}_{\text{eq}}$  is available in closed-form, we are guaranteed to find the optimum value of  $\hat{\mathbf{E}}_{\text{eq}}$  for that particular  $\hat{\mathbf{c}}^{(n+1)}$ . With that we have

$$J_{\text{ML}}\left(\hat{\mathbf{E}}_{\text{eq}}^{(n)}, \hat{\mathbf{c}}^{(n+1)}\right) \geq J_{\text{ML}}\left(\hat{\mathbf{E}}_{\text{eq}}^{(n+1)}, \hat{\mathbf{c}}^{(n+1)}\right) \quad (4.21)$$

By comparing (4.18) with (4.21), we see that each iteration of the alternating optimization method either decreases or maintains the associated value in the cost function. This guarantees the convergence of the method, either to the global optimum, a local optimum or a saddle point of  $J_{\text{ML}}(\mathbf{E}_{\text{eq}}, \mathbf{c})$ .

### 4.1.3 Numerical Results

Here we show some simulation results that motivate the use of the proposed ML estimator to process distributed massive MIMO measurements sets of the nature of (4.7). We simulate the case of jointly calibrating three CSPs, each CSP having 32 antennas and 3 possible DFT beams. Moreover, the transmit and receive beamforming codebooks are DFT matrices of size  $32 \times 32$  and all CSPs share such codebooks for transmission and reception.

We define gains of the transmitters chains, namely  $t_1$ ,  $t_2$ , and  $t_3$ , and the gains of the receivers chains, namely  $r_1$ ,  $r_2$ , and  $r_3$ , as i.i.d. (unit-length) phasors with uniform phase distribution across  $[0, 2\pi[$ . The non-diagonal entries of the symmetric propagation channel matrix  $\mathbf{H}_p^{i,j} \forall i, j$ , are i.i.d. zero-mean unit-variance circularly symmetric complex-valued Gaussian variables, and the non-diagonal entries of the additive receiver noise matrices,  $\mathbf{N}_{i,j}$  and  $\mathbf{N}_{j,i}$ , are i.i.d. zero-mean circularly symmetric complex-valued Gaussian variables with variance  $\sigma^2$ . (The diagonal entries are undefined as previously mentioned.) The calibration SNR is here defined as  $\sigma^{-2}$ . We use the ML-based alternating algorithm proposed above to post process the measurements and estimate the calibration matrix  $\mathbf{C} = \text{diag}\{\mathbf{c}\}$ , where  $\mathbf{c} = [c_1, \dots, c_M]^T$ .

Since the main application for the calibration weights is in the context of (reciprocity-based) beamforming (and beamforming is only concerned with complex amplitude differences between antenna elements, and not with their absolute values), any scaled version of a calibration vector is equally good in terms of beamforming performance, i.e., the vector estimate  $\hat{\mathbf{c}}$  is as good as the vector  $\alpha\hat{\mathbf{c}}$ , for  $\alpha$  being any non-zero complex number. Thus, one calibration performance error metric that takes this into account is one minus the squared cosine of the principal angle between

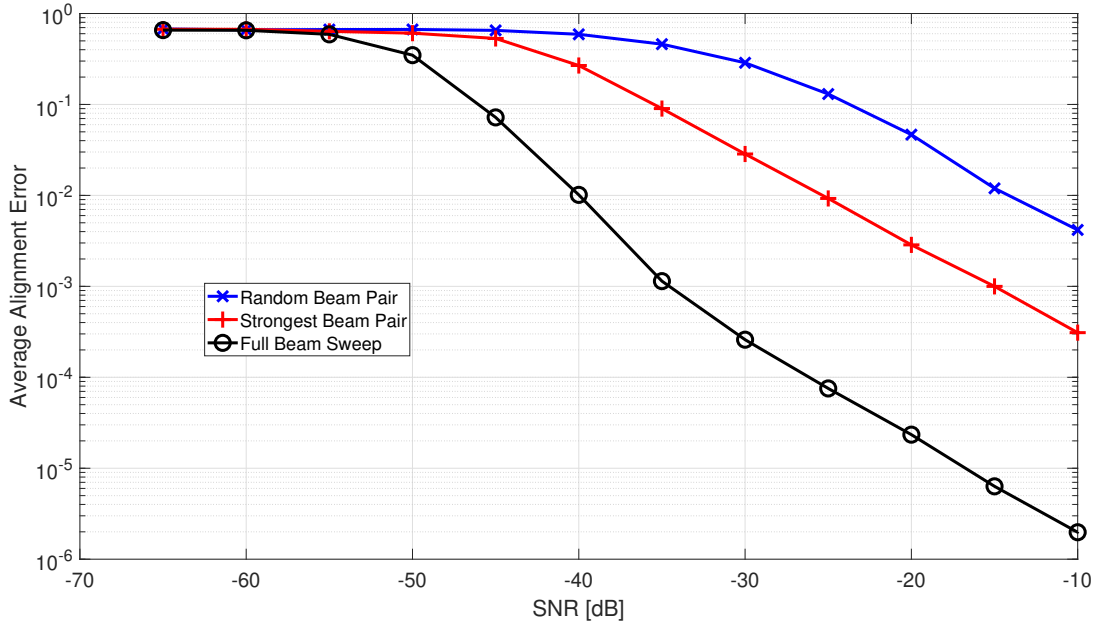


Figure 4.1: Alignment Error metric versus SNR for the case of calibrating using 3 distinct measurements sets.

the subspace spanned by the true coefficient vector  $c$  and the subspace spanned by the vector estimate  $\hat{c}$ . For example, when the estimate is perfect and the subspace of  $c$  is perfectly aligned with the subspace of  $\hat{c}$ , the error metric equals to zero. This error metric can be written as

$$\text{Average Alignment Error} = \mathbb{E} \left[ 1 - \frac{|c^H \hat{c}|^2}{c^H c \hat{c}^H \hat{c}} \right], \quad (4.22)$$

where the expectation operator  $\mathbb{E}[\cdot]$  acts jointly over the random sources of the signal model.

Figure 4.1 depicts the Average Alignment Error metric versus SNR for the case of calibrating with three distinct measurements sets. Two of the three measurement sets use only one double-directional measurement between each pair of CSPs in order to compute the calibration coefficients. In this case, state-of-the-art calibration schemes originally designed for fully-digital systems, can be used straightforwardly to post-process the measurement sets. The third measurement set consists of the case of performing a full-beam sweep for each CSP pair, and post-processing the resulting entire measurement with the proposed algorithm (since state-of-the-art methods cannot be used here).

The blue curve represents the case of using only one double directional measurement between each pair of CSPs, where each beamformer pair (i.e. the transmit and receive beams) is picked at random with equal probability among all possible beamforming pairs. The red curve represents the case of using one double-directional measurement between each pair of CSPs, where each measured is associated with the beamformer pair that maximizes the energy of the effective channel gain. Finally, the black curve represents the case of combining the measurements from all beam pair combinations, according to the estimator proposed above.

The gap between the blue and red curves is justified by the strongest measurement of the set always yielding equal for greater calibration SNR compared to using an arbitrary beam pair. Finally, the gap between the red and black curves, shows how measurements associated with

beam pairs, other than the beam pair yielding the highest link budget, contribute for enhancing the calibration quality. Thus, if measurements other than the measurements associated with the strongest beam pair are available, they should be also post-processed and used for calibration purposes. This motivates the usage of neat signal processing methods, as the proposed algorithm, which is able to post-process multi-beam measurements for calibration – a feature not existing in state-of-the-art massive MIMOs calibration literature.

## 4.2 Graph-based Subarray Fusion for Channel Estimation

Due to the large aperture of RWs and near-field propagation, the RW channel shows non-stationary spatial properties which have been clearly shown in the previous study [2, 25, 26] with real measurements. In this section, we investigate the potential of using subarray data fusion for RW channel estimation. We apply a belief propagation (BP)-based algorithm [19] to sequentially detect and estimate SMC parameters based on radio signals at each subarray. The joint detection and estimation problem is formulated as a Bayesian model and then represented by a factor graph enabling the use of BP for efficient computation of the marginal posterior distributions. At each subarray, a snapshot-based parametric channel estimator provides parameter estimates of a set of SMCs, e.g., distances, angles and SNRs, which are used as noisy measurements by the BP-based algorithm. It performs joint probabilistic data association, estimation of the time-varying SMC parameters, and the mean number of false alarm measurements by means of the sum-product algorithm rules. The algorithm further exploits amplitude information to improve the detection of “weak” SMCs with very low SNRs.

As a preliminary study, fully synthetic measurements were used without involving the snapshot-based channel estimator. The simulation environment is shown in Fig.4.2, where the RW is segmented into 75 subarrays with each consisting of  $4 \times 4$  or  $8 \times 8$  antenna elements. For simplicity, we consider only the LOS propagation path and four 1st order reflected SMCs with varying visibility across subarrays and overlapping in the delay and angular subspace. In each simulation run, SMC-oriented measurements of each subarray were generated by adding Gaussian noises to the true SMC parameters, where the noise variances were state-dependent and determined based on the Fisher information given the signal bandwidth of 100 MHz and  $\text{SNR} \in \{18, 30\}$  dB. Note that frequency sample gain and array gain are included in the formulation of SNRs. In addition, false alarm measurements were also generated. In total, we performed 50 simulation runs for each SNR and each subarray dimension, respectively. The BP-based algorithm was performed according to the order of the subarray indices shown in Fig. 4.2b.

Fig. 4.3 shows the results of an exemplary simulation run for a challenging setup with  $\text{SNR} = 18$  dB and subarray dimension  $4 \times 4$ . It is seen that the algorithm excellently copes with intersecting MPCs and exhibits high detection and estimation accuracy for medium and high SNR SMCs. The “weakest” SMC that is mostly below the false alarm SNR level is also stably detected shortly after the beginning. Fig. 4.4 further presents the MOSPA errors<sup>1</sup> of SMC parameters, the averaged number of detected SMCs. Given high SNR value, the number of SMCs is accurately estimated. For distance, AOA and component SNR, the MOSPA errors are mostly below 0.15 m, 2 degree and  $-35$  dB, respectively. Given  $\text{SNR} = 18$  dB, the MOSPA errors remain on the mean posterior error bound levels mostly, despite a few peaks due to the underestimated number of

<sup>1</sup>The performance is measured using the optimal subpattern assignment (OSPA) metric [27], which can efficiently capture the estimation errors of the model order and MPC states when comparing with the true MPC states at each time or step. The mean OSPA (MOSPA) errors are obtained at each time by averaging over all simulation runs.

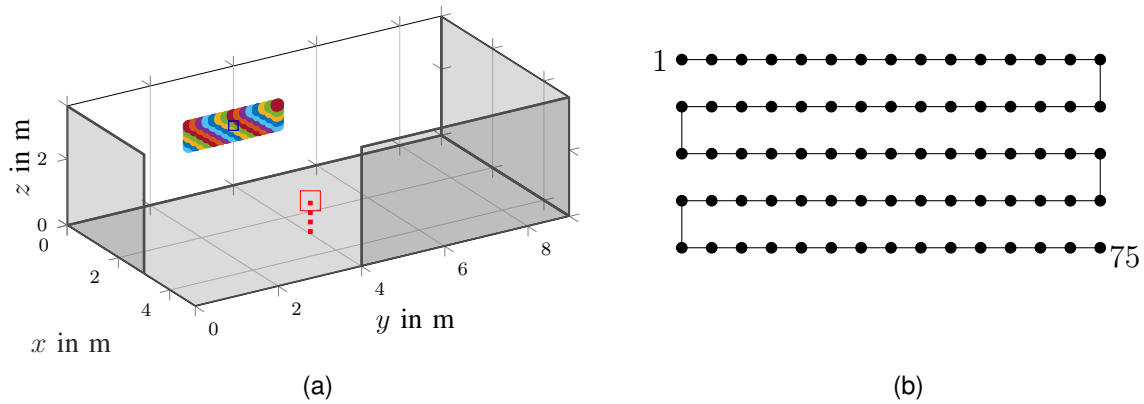


Figure 4.2: (a) 3D model demonstrating the simulation environment. The 75 subarrays of the RW are denoted with markers highlighted with different colors. The red square marker represents the static UE. (b) Subarrays are indexed in top-to-bottom “zigzag” order.

SMCs and overlap between SMC.

In conclusion, the BP-based algorithm is capable of capturing the non-stationary properties of the RW channel by processing subarray radio signals sequentially. In addition, small subarrays allow for efficient implementation of the considered algorithms and allows to efficiently distribute computation resources. Having the capability of fusing the measurements of the CSPs on a subarray basis enables an efficient use of resources, by performing separate processing using super-resolution channel estimation algorithms. The obtained fused estimates can be used in positioning applications, for example in the EKF-based approach outlined in the following section, Section 4.3. In addition, the component estimates can be used as input for

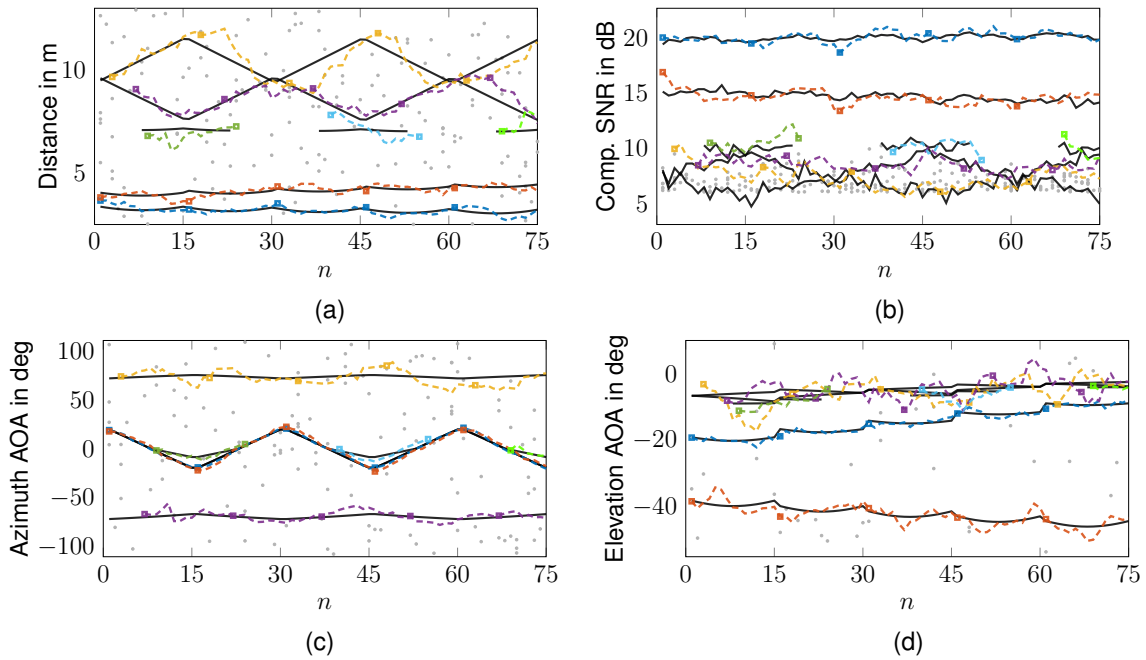


Figure 4.3: Results for fully synthetic measurements with the BP-based algorithm given  $\text{SNR} = 18 \text{ dB}$  and subarray dimension  $4 \times 4$ . Estimates of (a) distance, (b) component SNR, (c) azimuth AOA and (d) elevation AOA. The black solid lines denote the true SMC parameters. The gray dots denote the false alarm measurements. The estimates of different SMCs are denoted with densely-dashed lines with square markers in different colors.

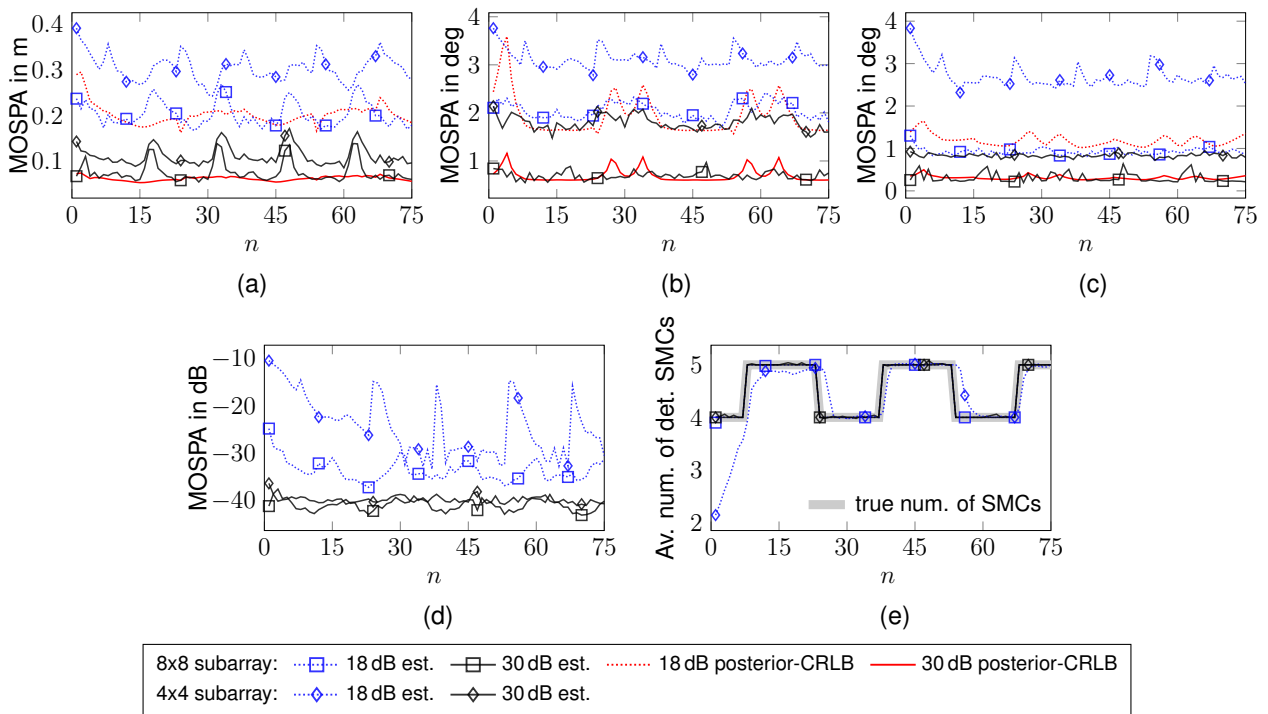


Figure 4.4: Results for fully synthetic measurements with the proposed algorithm given  $\text{SNR} = \{18, 30\} \text{ dB}$  and subarray dimensions of  $4 \times 4$  and  $8 \times 8$ , respectively. MOSPA errors of the estimated (a) distances, (b) azimuth AOAs, (c) elevation AOAs, (d) input component SNRs, and (e) the averaged number of detected SMCs.

## 4.3 EKF-based Position Tracking and Clock-synchronization

This section investigates the application of [10] to the RW infrastructure as baseline algorithm for joint synchronization and positioning, which can be applied either to tracking of a dynamic UE or to measurement fusion of a static UE. For positioning, we exploit the LOS path in a similar fashion as in the analysis of the fundamental performance limits in Chapter 3, relying on a LOS-only model as simplest baseline case. While this will be a limitation that needs to be addressed during algorithm validation with measurement data, either a simple pre-selection step from multiple measurements obtained per CSP (subarray) can be performed, e.g., using the algorithms obtained with the graph-based algorithm discussed in Section 4.2. Nonetheless, the extension to a general multipath model will be addressed in the final stage of the project.

### 4.3.1 UE Motion Model

For the motion of the UE, we assume a standard linear state-space model. The UE state at time step  $k + 1$  depends linearly on the previous state according to

$$\mathbf{x}_{k+1} = \mathbf{A}\mathbf{x}_k + \mathbf{w}_k \quad (4.23)$$

$$\mathbf{y}_k = \mathbf{g}(\mathbf{x}_k) + \mathbf{n}_k, \quad (4.24)$$

with the state  $\mathbf{x}_k \in \mathbb{R}^N$ , with  $\mathbf{A} \in \mathbb{R}^{N \times N}$  denoting the state transition matrix. The measurement  $\mathbf{y}_k \in \mathbb{R}^P$  contains measurements at time step  $k$ , with  $\mathbf{g}(\cdot) \in \mathbb{R}^P$ , denoting the measurement function depending on the current state. In addition, white process noise  $\mathbf{w}_k \in \mathbb{R}^N \sim \mathcal{N}(\mathbf{0}, \mathbf{W})$  and measurement noise  $\mathbf{n}_k \in \mathbb{R}^P \sim \mathcal{N}(\mathbf{0}, \mathbf{V})$  are introduced.  $P$  denotes the number of available measurements.

Assuming the UE moves with a constant velocity for simplicity, the state vector  $\mathbf{x}_k \in \mathbb{R}^6$  consists of the current position  $\mathbf{p}_k \in \mathbb{R}^3$  and velocity  $\mathbf{v}_k \in \mathbb{R}^3$  according to

$$\mathbf{x}_k = [p_{k,x}, p_{k,y}, p_{k,z}, v_{k,x}, v_{k,y}, v_{k,z}]^T = [\mathbf{p}_k^T, \mathbf{v}_k^T]^T. \quad (4.25)$$

The corresponding state transition matrix is then found as

$$\mathbf{A} = \begin{bmatrix} \mathbf{I}_{3 \times 3} & T_d \mathbf{I}_{3 \times 3} \\ \mathbf{0}_{3 \times 3} & \mathbf{I}_{3 \times 3} \end{bmatrix}, \quad (4.26)$$

where  $\mathbf{0}_{N \times M}$  denotes a  $(N \times M)$  zero matrix and  $\mathbf{I}_{N \times M}$  is a  $(N \times M)$  identity matrix, and  $T_d$  denotes the time between consecutive time steps. The measurements are performed using antenna arrays which provide distance and angle measurements [28, 29], the measurement vector at time step  $k$  becomes

$$\mathbf{y}_k = \begin{bmatrix} \text{atan}(p_{k,y} - a_y, p_{k,x} - a_x) + \bar{\varphi}_{\text{az}} \\ \arccos\left(\frac{p_{k,z} - a_z}{\sqrt{(p_{k,x} - a_x)^2 + (p_{k,y} - a_y)^2 + (p_{k,z} - a_z)^2}}\right) + \bar{\vartheta}_{\text{el}} \end{bmatrix} = \begin{bmatrix} \varphi_k \\ \vartheta_k \\ r_k \end{bmatrix} = \mathbf{g}(\mathbf{x}_k). \quad (4.27)$$

with the array position<sup>2</sup> defined as  $\mathbf{a} = [a_x, a_y, a_z]^T$  and  $r_k$  denoting the range relative to the array, and  $\varphi_k$  the azimuth and  $\vartheta_k$  the elevation angles. To apply the extended Kalman filter (EKF) [30],

<sup>2</sup>To improve the readability the notation of the positions of CSP and UE was adapted slightly from the one used in Section 2.1.

the nonlinear system is linearized using a Taylor approximation, with the resulting (linearized) measurement matrix, converting the agent state to distance and angle measurements, found as

$$\mathbf{H}_k^{\text{meas}} = \frac{\partial \mathbf{g}}{\partial \mathbf{x}} \Big|_{\tilde{\mathbf{x}}_k} = \begin{bmatrix} -\frac{p_{k,y}}{p_{k,x}^2 + p_{k,y}^2} & \frac{p_{k,x}}{p_{k,x}^2 + p_{k,y}^2} & 0 & \vdots \\ -\frac{p_{k,x}p_{k,z}}{\sqrt{p_{k,x}^2 + p_{k,y}^2}(p_{k,x}^2 + p_{k,y}^2 + p_{k,z}^2)} & -\frac{p_{k,y}p_{k,z}}{\sqrt{p_{k,x}^2 + p_{k,y}^2}(p_{k,x}^2 + p_{k,y}^2 + p_{k,z}^2)} & \frac{\sqrt{p_{k,x}^2 + p_{k,y}^2}}{(p_{k,x}^2 + p_{k,y}^2 + p_{k,z}^2)} & \mathbf{0}_{3 \times 3} \\ \frac{p_{k,x}}{\sqrt{p_{k,x}^2 + p_{k,y}^2 + p_{k,z}^2}} & \frac{p_{k,y}}{\sqrt{p_{k,x}^2 + p_{k,y}^2 + p_{k,z}^2}} & \frac{p_{k,z}}{\sqrt{p_{k,x}^2 + p_{k,y}^2 + p_{k,z}^2}} & \vdots \end{bmatrix}. \quad (4.28)$$

### 4.3.2 Clock Offset Model

As synchronization plays a key role in the distributed RW infrastructure, we include clock offset between subarrays as described in Chapter 2, which is similar to the model used in [10]. The corresponding unknown delay from each CSP to the agent is introduced into the state space model. The clock offset  $\epsilon_k \in \mathbb{R}$  at time  $k$  is modeled as an autoregressive process [29] as used in (2.25)

$$\epsilon_{k+1} = \epsilon_k + \delta_k T_d, \quad (4.29)$$

where the clock drift  $\delta_k \in \mathbb{R}$  is modeled as

$$\delta_{k+1} = \beta \delta_k + \eta_k \quad (4.30)$$

with  $|\beta| \leq 1$  and a white Gaussian process noise with zero-mean  $\eta_k \sim \mathcal{N}(0, \sigma_\eta) \in \mathbb{R}$ . In a more compact form, this becomes

$$\boldsymbol{\theta}_{\text{clk},k} = \begin{bmatrix} \epsilon_k \\ \delta_k \end{bmatrix} = \begin{bmatrix} 1 & T_s \\ 0 & \beta \end{bmatrix} \begin{bmatrix} \epsilon_{k-1} \\ \delta_{k-1} \end{bmatrix}. \quad (4.31)$$

For simplicity, we assume a constant clock drift with  $\beta = 1$ . By including the clock offset  $\epsilon_k$  in the measurement model one obtains

$$\mathbf{y}_k = \tilde{\mathbf{g}}(\mathbf{x}_k, \boldsymbol{\theta}_{\text{clk},k}) = \begin{bmatrix} \text{atan}(p_{k,y} - a_y, p_{k,x} - a_x) + \bar{\varphi}_{\text{az}} \\ \arccos\left(\frac{p_{k,z} - a_z}{\sqrt{(p_{k,x} - a_x)^2 + (p_{k,y} - a_y)^2 + (p_{k,z} - a_z)^2}}\right) + \bar{\vartheta}_{\text{el}} \\ \|\mathbf{p}_k - \mathbf{a}\| + \epsilon_k \end{bmatrix} = \begin{bmatrix} \varphi_k \\ \vartheta_k \\ r_k + \epsilon_k \end{bmatrix} \quad (4.32)$$

from which the linearized measurement matrix is obtained according to

$$\tilde{\mathbf{H}}_k^{\text{meas}} = \begin{bmatrix} \mathbf{H}_k^{\text{meas}} & | & | & 0 & 0 \\ \mathbf{0}_{3 \times 3} & | & | & 0 & 0 \\ & & & 1 & 0 \end{bmatrix}. \quad (4.33)$$

### 4.3.3 Measurement Configurations

This section describes two types of measurement configurations for which the positioning performance is analyzed. These configurations are *full* measurements consisting of AOA and time-of-arrival (TOA) measurements, and *AOA-only* measurements, where no range measurements, i.e., distance/delay estimates, are available. This allows to investigate performance in challenging scenarios, especially at a lower system bandwidth or when the clock offset is too large, resulting in the distance measurements being inaccurate to the point of being considered outliers, or being obtained by a channel estimation algorithm that only provides angle measurements.

**TOA-AOA measurements** Assuming all measurements to be available, one can simply stack the corresponding measurements per subarray resulting in a measurement vector  $\check{\mathbf{y}}_k$  of dimensions  $(3Q \times 1)$  with  $Q$  being the number of subarrays.

$$\check{\mathbf{y}}_k = [\mathbf{y}_{1,k}, \dots, \mathbf{y}_{Q,k}]^T \in \mathbb{R}^{3Q}. \quad (4.34)$$

**AOA-only measurements** When only angular measurements are used, the range measurements in the measurement vector are not considered for  $\hat{\mathbf{g}}(x)$  and completely removed. The resulting measurement vector becomes

$$\check{\mathbf{y}}_k = [\varphi_{1,k}, \vartheta_{1,k}, \dots, \varphi_{Q,k}, \vartheta_{Q,k}]^T \in \mathbb{R}^{2Q}. \quad (4.35)$$

#### 4.3.4 Extended Kalman Filter (EKF)

The Kalman filter is the solution to the optimal state estimation problem given noisy measurement data from a state-space system as described in Section 4.3.1 [15, 30]. Based on the state and measurement models, the optimal Kalman gain  $\mathbf{K}_k$  is computed to minimize the estimation covariance of the error  $e_k = \mathbf{x}_k - \hat{\mathbf{x}}_k^+$  at each sampling time step  $k \in \{0, 1, \dots\}$ . Based on an a-priori state estimate  $\hat{\mathbf{x}}_{k+1}^-$  one commonly obtains a state prediction

$$\hat{\mathbf{x}}_{k+1}^- = \mathbf{A}\mathbf{x}_k^+ \quad (4.36)$$

which is then updated to obtain a-posteriori estimate  $\hat{\mathbf{x}}_{k+1}^+$  by fusing the measurements via the Kalman gain. To this end

$$\mathbf{P}_{k+1}^- = \mathbf{A}\mathbf{P}_k^+ \mathbf{A}^T + \mathbf{W} \in \mathbb{R}^{N \times N} \quad (4.37)$$

where  $\mathbf{P}_{k+1}^-$  is the predicted state covariance matrix. With the current measurement  $\mathbf{y}_{k+1}$  available, the posterior state estimate is obtained as

$$\hat{\mathbf{x}}_{k+1}^+ = \hat{\mathbf{x}}_{k+1}^- + \mathbf{K}_{k+1}(\mathbf{y}_{k+1} - (\mathbf{H}_k^{\text{meas}})^T \hat{\mathbf{x}}_{k+1}^-), \quad (4.38)$$

where the Kalman gain defined as

$$\mathbf{K}_{k+1} = \mathbf{P}_{k+1}^- (\mathbf{H}_k^{\text{meas}})^T (\mathbf{H}_k^{\text{meas}} \mathbf{P}_{k+1}^- (\mathbf{H}_k^{\text{meas}})^T + \mathbf{V})^{-1} \quad (4.39)$$

and with  $\mathbf{V} \in \mathbb{R}^{N \times N}$  representing the measurement noise covariance matrix. The necessary steps of the EKF are summarized in Algorithm 1.

#### 4.3.5 Simulation Scenario

In this section, the simulation environment used to evaluate the performance of the EKF algorithm is described, including various scenarios for comparison. First, the simulation setup and parameters are introduced, followed by a statistical evaluation of different models and their performance metrics. By means of Monte Carlo simulations, the different measurement scenarios are compared. The EKF-based algorithm is applied to both measurement cases of TOA-AOA measurements as well as AOA-only measurements. In addition, the performance of a single CSP is compared to two CSPs with and without clock offset.

---

**Algorithm 1** The extended Kalman filter (EKF) [15, 30]
 

---

```

 $\hat{\mathbf{x}}_0^+ \leftarrow \text{init.}$ 
 $\mathbf{P}_0^+ \leftarrow \text{init.}$ 
for  $k$  in  $K$  do
   $\mathbf{P}_k^- \leftarrow \mathbf{A}\mathbf{P}_{k-1}^+\mathbf{A}^\top + \mathbf{W}$ 
   $\hat{\mathbf{x}}_k^- \leftarrow \mathbf{A}\mathbf{x}_{k-1}$ 
   $\mathbf{H}_k \leftarrow \frac{\partial \mathbf{g}_k}{\partial \mathbf{x}} \Big|_{\hat{\mathbf{x}}_k^-}$ 
   $\mathbf{K}_k \leftarrow \mathbf{P}_k^- (\mathbf{H}_k^{\text{meas}})^\top (\mathbf{H}_k^{\text{meas}} \mathbf{P}_k^- (\mathbf{H}_k^{\text{meas}})^\top + \mathbf{V})^{-1}$ 
   $\hat{\mathbf{x}}_k^+ \leftarrow \hat{\mathbf{x}}_k^- + \mathbf{K}_k [\mathbf{y}_k - \mathbf{g}(\hat{\mathbf{x}}_k^-)]$ 
   $\mathbf{P}_k^+ \leftarrow (\mathbf{I} - \mathbf{K}_k \mathbf{H}_k^{\text{meas}}) \mathbf{P}_k^-$ 
end for

```

---

### Settings

In the simulation environment, two physically large antenna arrays, with  $(112 \times 75)$  antennas each, are generated and split up into  $(15 \times 15)$  sub-arrays, arranged regularly in a grid with a spacing of  $\lambda/2 = 2.158$  cm for a carrier frequency of  $f_c = 6$  GHz. Since the second wall-mounted array is added to improve the performance of the algorithm, the two arrays are orthogonal to each other, for a maximal improvement over the singular array case due to the reduction in the angular uncertainty. To generate noisy position estimates, the trajectory positions of the device to be tracked are corrupted by additive Gaussian noise. Fig. 4.5 depicts the used measurement setup and trajectory positions. To simulate a measurement setup that uses a small bandwidth value, it is possible to exclude the range measurements to also emulate scenarios with a lower available bandwidth as well as only use one of the two antenna arrays.

The parameters that are used for the simulations are introduced are summarized below and were chosen based on the analysis of the performance limits in terms of the CRLB performed in Chapter 3.

- $\sigma_{\text{AOA}} \in \{0.1^\circ, 1^\circ, 5^\circ\}$  – standard deviation of the Gaussian noise of both angular measurements ( $\varphi_k$  and  $\vartheta_k$ )
- $\sigma_{\text{TOA}} \in \{0\text{m}, 0.05\text{m}, 0.5\text{m}\}$  – standard deviation of the Gaussian noise of the range measurements ( $r_k$ )
- $u_{\text{clk}} \in \{0\text{m}, 0.2\text{m}\}$  – range of the uniformly distributed clock offsets per sub-array (i.e. they are bounded by  $|u_{\text{clk}}|$ )
- $\beta \in \{0\text{m/s}, 0.001\text{m/s}\}$  – amount of clock skew

If not stated otherwise, the standard settings used are  $\sigma_{\text{AOA}} = 1^\circ$ ,  $\sigma_{\text{TOA}} = 0.05\text{m}$ ,  $|u_{\text{clk}}| = 0.2\text{m}$ ,  $\beta = 0.001\text{m/s}$ . Additionally, the state covariance parameters are chosen as

$$\mathbf{U}_x = \text{diag}([0.1, 0.1, 0.1, 0.05, 0.05, 0.05]), \quad (4.40)$$

where the operator  $\text{diag}(\dots)$  denotes a diagonal matrix with the elements provided in the vector. For the clock offsets we use

$$\mathbf{U}_{\theta_{\text{clk}}} = \text{diag}([0.1, 0.05]) \quad (4.41)$$

which are then combined into

$$\mathbf{U} = \text{blkdiag}(\mathbf{U}_x, \mathbf{U}_{\theta_{\text{clk}}}) \quad (4.42)$$

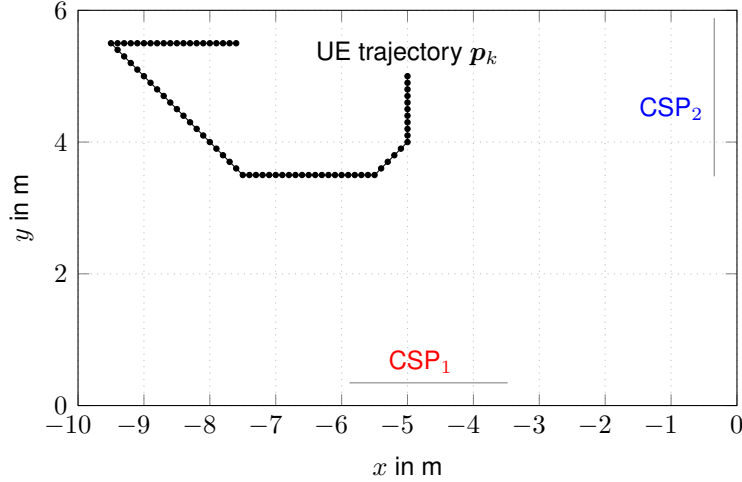


Figure 4.5: Setup with the trajectory of the agent and antenna array positions used in simulations.

Table 4.1: Color scheme used in the result plots.

color	abbr.	description
black	TOA-AOA	Predictions made using noisy data without clock offset errors with range and angular measurements available, representing the baseline case.
orange	AOA	Predictions made using noisy data (measurement noise) with only angular measurements available.
red	TOA-AOA w/o clk	Predictions made using noisy data (clock offset + measurement noise) with range and angular measurements available.
green	TOA-AOA clk	Predictions made using noisy data (clock offset + measurement noise) with range and angle measurements available where the clock offset has been compensated for in the model.

representing a block diagonal matrix. The measurement covariance matrix is set to

$$\mathbf{R} = \text{diag} \left( \left[ \frac{5\pi}{180}, \frac{5\pi}{180}, 0.2 \right] \right). \quad (4.43)$$

The state covariance matrix  $\mathbf{P}$  is initialized as an identity matrix, i.e.  $\mathbf{P}_0^+ = \mathbf{I}$  and the initial state  $\mathbf{x}_0^+$  is set to the true location of the UE.

The performance metric we use the root-mean-square error (RMSE) over a number of iterations  $R$ , which is defined as

$$\bar{e}_{\text{pos},k} = \sqrt{\frac{1}{R} \sum_{i=1}^R \|\mathbf{p}_k^{\text{true}} - \hat{\mathbf{p}}_k^{(i)}\|^2}. \quad (4.44)$$

with the  $\hat{\mathbf{p}}_k^{(i)}$  denoting the position estimate from the estimated state  $\hat{\mathbf{x}}_k$  at time step  $k$  for iteration  $i = 1, \dots, R$ . In the Monte Carlo analysis, the simulations are performed for  $R = 500$  realizations.

### 4.3.6 Simulation Results

This section presents the simulation results of the EKF-based algorithm for different parameter settings, comparing the performance of a single CSP ( $J = 1$ ) and two CSPs ( $J = 2$ ), and the

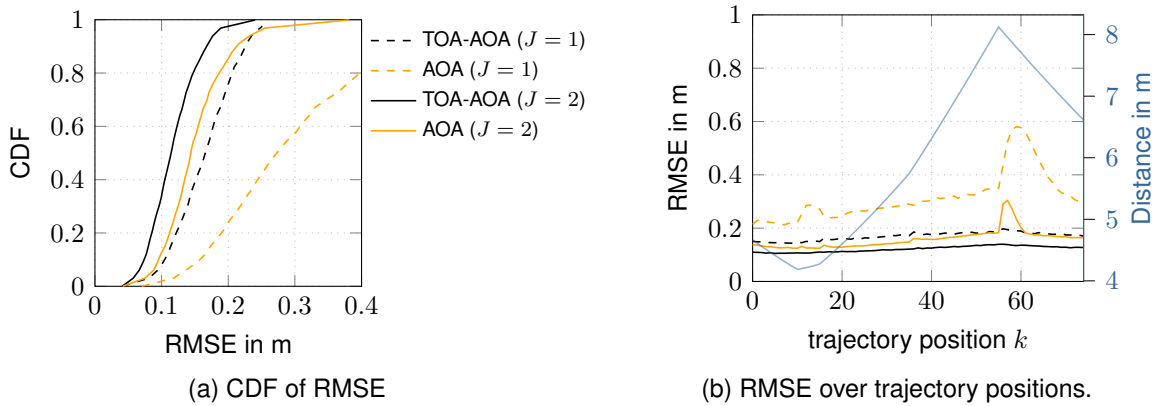


Figure 4.6: Comparison of error metrics for different measurement setups (only angular measurements versus angular and range measurements as well as one used array versus two CSPs).

error behavior along the trajectory positions. We compare the AOA-only case with the AOA-TOA case. For simulations with only one array, array one is used (see Fig. 4.5). The color scheme for the different configurations as used in the figures is described in Table 4.1. Simulation results where only one array has been used are shown as dashed lines.

### Baseline Case

As a baseline case, the algorithm is evaluated without clock offset, allowign to analyze the optimum performance of the scenario. Fig. 4.6 compares the use of one versus two CSPs for AOA-only measurements (orange) and AOA-TOA measurements (black) in terms of the cumulative distribution functions (CDFs) of each configuration. The performance improvement by exploiting the range measurements is visible in the CDF which approaches 1 for lower RMSE values. When using both CSPs with range and angle measurements available (black solid), the CDF reaches a value of 0.9 at 0.17m RMSE, at 0.21m when using only the angular component, at 0.22m when using only a single CSP with range measurements and at 0.47m for a single CSP without range measurements.

Figure 4.6b shows the RMSE along the trajectory, and the mean distance to the CSPs. Importantly the position error increases when the agent moves farther away from the array. This is due to the fact that the AOA information regarding the UE position decreases with distance as shown in Chapter 3. The configuration using both range and angular measurements performs best, while the using just the AOA measurement result in a larger RMSE. Abrupt changes in directions are not well represented by the motion model, which is visible as spikes in the RMSE curves at these trajectory positions (see Fig. 4.6b).

### Constant Clock Offset

When a time invariant clock offset between subarrays of the CSPs is included, the performance of the tracking algorithm suffers heavily and the RMSE increases when using both angle and range measurements, while the performance is not affected when using only angular measurements. This can be seen in Figure 4.7a showing the CDF of the RMSE and in Figure 4.7b showing mean RMSE over all trajectory positions. It is however possible to improve the results by tracking the clock offset in the system state alongside the UE position. Fig. 4.7b shows that by tracking

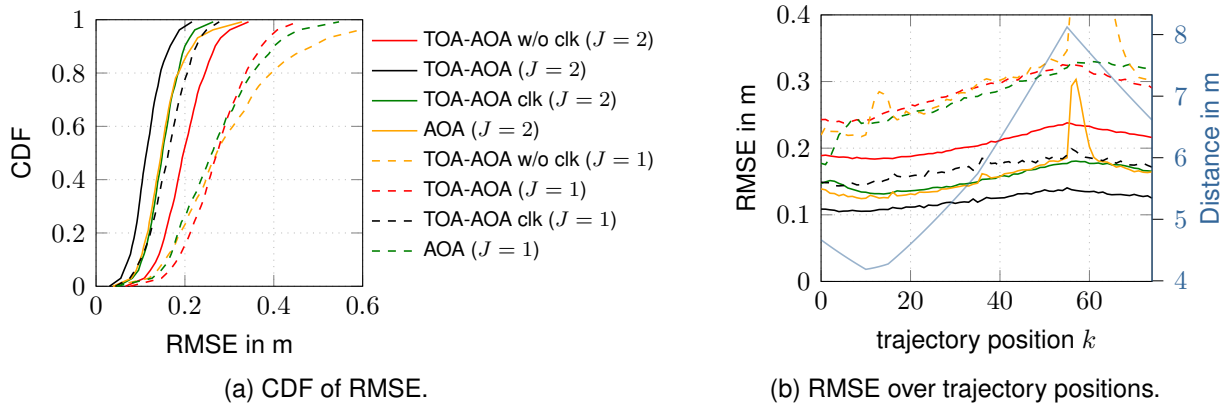


Figure 4.7: Comparison of error metrics for different measurement setups where a clock offset has been introduced (only angular measurements versus angular and range measurements as well as one used array versus two CSPs).

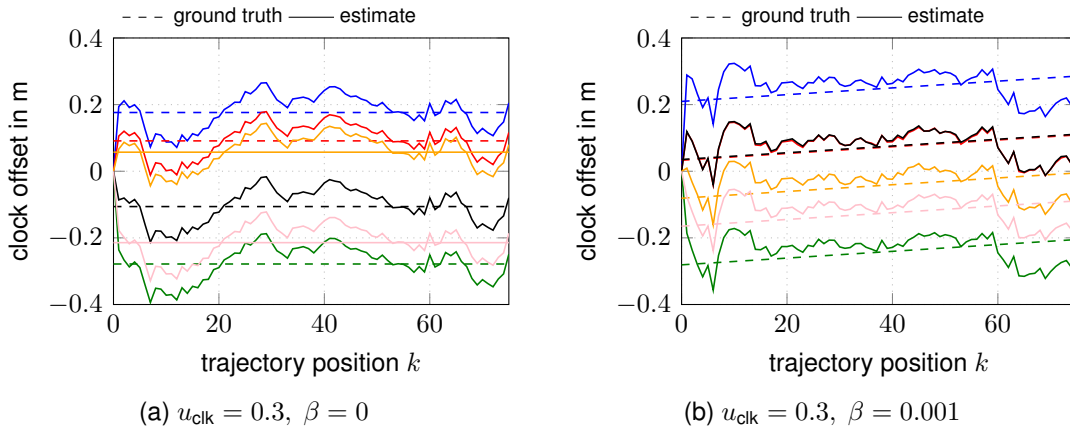


Figure 4.8: Offsets for the first 5 sub-arrays compared with the corresponding tracked values.

the offset (green) a higher accuracy and robustness can be achieved compared to angle-only measurements (orange) or when ignoring the clock offset (red).

### Time Varying Clock Offset

Adding the clock skew as state variable allows to account for time varying clock offset, e.g., tracking of slowly drifting clocks. Fig. 4.8 shows tracking results for the two used clock offset models, showing the tracking performance for a constant clock in Fig. 4.8a and the time varying clock in Fig. 4.8b. Due to the high range accuracy, it is however still possible to track the clock offset of each CSPs subarray (see Fig. 4.8 showing one exemplary realization). When included in the EKF state, tracking of the clock offset allows for higher accuracy, as shown by the CDF in Fig. 4.9a and the mean error over the trajectory in Fig. 4.9b, where the increasing clock offset results in an increasing RMSE in the uncompensated case (red). The compensation for the clock offset results in improved robustness of the algorithm using range and angle measurements (green) when compared to the case where only angular measurements are used (orange).

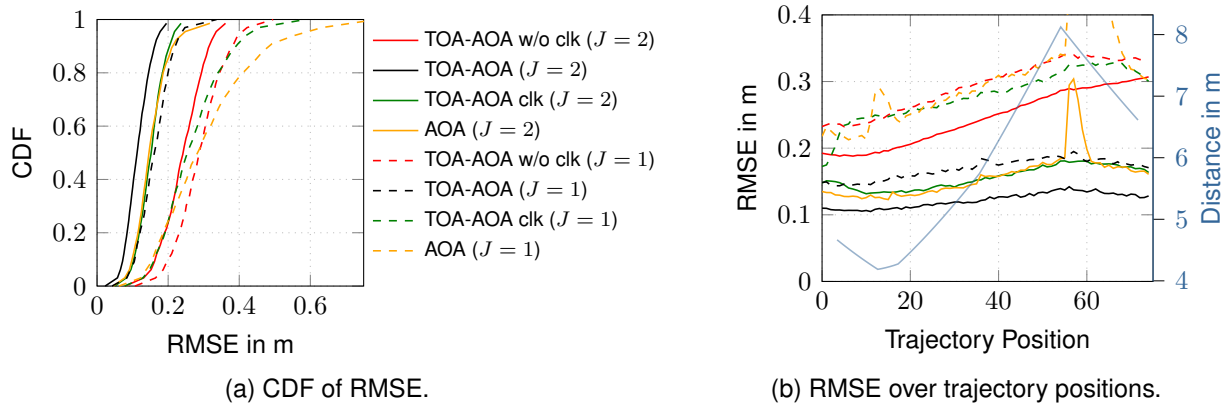


Figure 4.9: Comparison of error metrics for different measurement setups where an additional clock offset with skew is introduced (only angular measurements versus angular and range measurements as well as one CSP versus two CSPs).

### Simulation Parameter Comparison

To compare all different configurations of the simulations, the mean RMSE values for all runs are compared as error bar plots in Fig. 4.10. The top row shows results for high range and high angle accuracy, the middle row for medium range and high angle and the bottom row for low range and high angle accuracy.

While the performance with high range and angle accuracy is very similar for the case without clock offset and clock drift, simulating the clock offset shows the drastic effect when not including it in the tracked state vector (see NC in Figures 4.10a to 4.10c). In addition, the performance of the algorithm with clock offset compensation is close to the baseline approach (BL) and the angle-only approach (AO), see WC in Figures 4.10a to 4.10c. When decreasing the ranging accuracy, also the performance of the clock offset estimation degrades, while still showing similar performance as for the angle-only configuration, see in Figures 4.10d to 4.10e. For the lowest range accuracy of  $\sigma_{\text{TOA}} = 0.5$  m, the large range error overshadows the effect of the clock drift as well as of the clock offset (see Figures 4.10g to 4.10i).

### 4.3.7 Conclusion and Discussion

Considering the clock offset in the tracking of a mobile UE allows to apply the EKF-based algorithm in a realistic scenario, which can be extended to cope with slowly time-varying clock offset values [28]. The simulations have shown that the tracking algorithm heavily suffered from the effects of random time delays between the subarrays of CSPs, which can be overcome to achieve a more robust algorithm by tracking of the offset. Especially when the measurement resolution increases, e.g., due to higher bandwidth values, it becomes essential to compensate for synchronization issues to achieve a high performance. Another insight is that when the errors of the range measurements increase, tracking of the clock offset does not improve the accuracy above that of the angle-only positioning setup, as the estimation of the additional parameter introduces an additional cost.

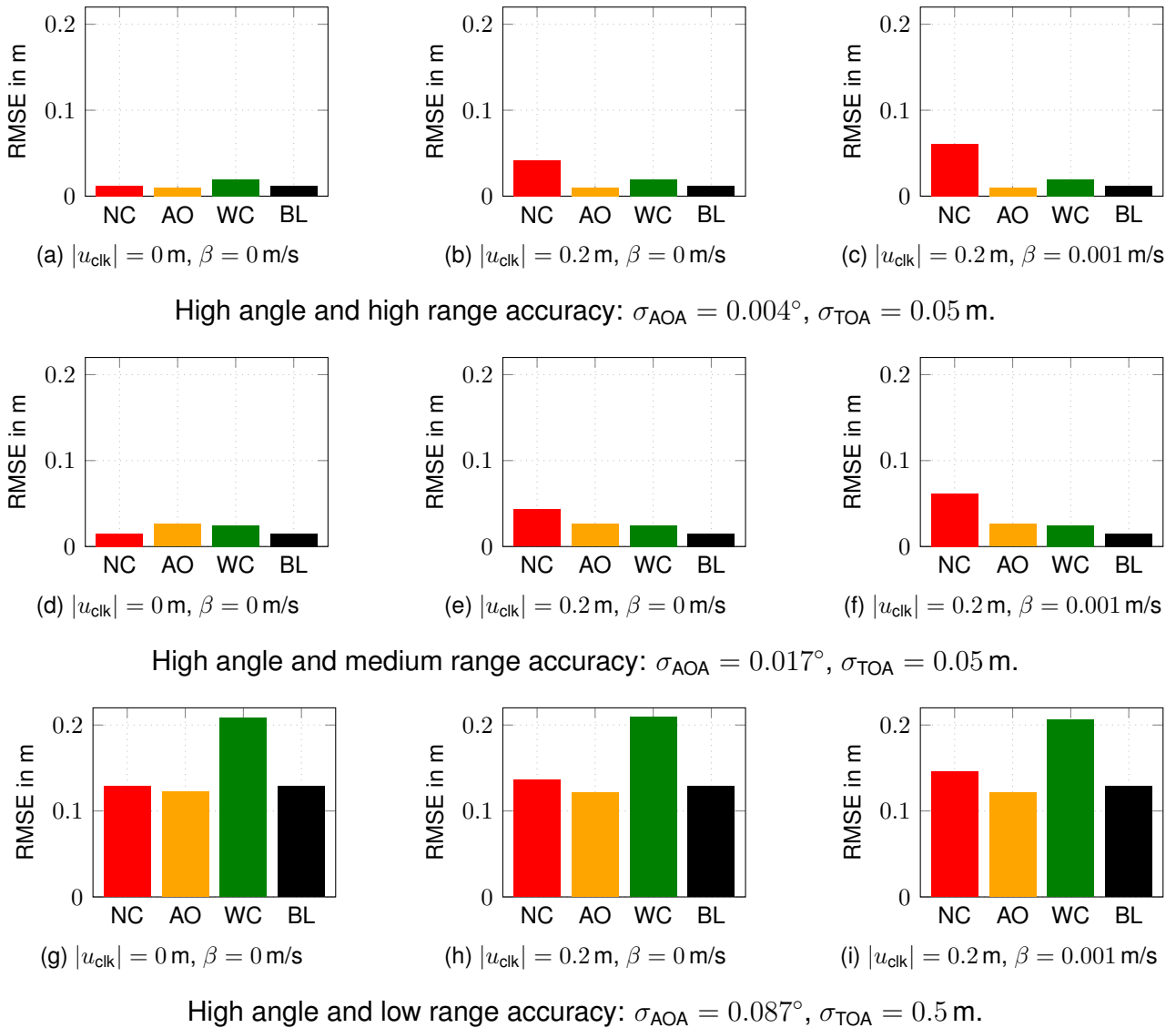


Figure 4.10: Comparison between the RMSE obtained for high, medium and low range and angle accuracy, showing the simulation results for different algorithm scenarios denoted as no correction (NC), angle-only (AO), with correction (WC), baseline case (BL).

# Chapter 5

## Joint Positioning, Learning and Sensing

This chapter introduces an algorithm capable of environment learning or sensing as well as positioning in a MIMO scenario, e.g., exploiting the possibility of using signals exchanged between CSPs, or between CSPs and UEs at known positions, or, in the most straightforward scenario in the context of RW, between a CSP and a single mobile device. The latter case can be expected to suffer from a reduced resolution. To this end, the mirror source model introduced in D1.2 [2], used to model multipath propagation, is exploited to localize reflecting surfaces. These reflecting surfaces can consequently be used to compute or calibrate the image source model from D1.2 [2]. Such a model is necessary to enable development of algorithms that rely on spatial consistency to learn specific environment features. In addition to the algorithmic approach, application examples fitting the context of the RW infrastructure are given.

### 5.1 MIMO Radar-based Environment Sensing

In the following, we describe a procedure to infer a geometric environment model from a distributed radio infrastructure based on a simple radar imaging scheme. The procedure presented below is published in [31] with the code and data accompanying the publication available in [32, 33].

#### 5.1.1 Channel Model

We use a geometry-based channel model for multiple-input single-output (MISO) systems, modeling the channel vector  $\mathbf{h}(\mathbf{p}, f) \in \mathbb{C}^{M \times 1}$  in the frequency domain, for a frequency  $f$ , and a specific UE device position  $\mathbf{p} = [p_x, p_y, p_z]^T$ . To highlight the direct dependency on the UE position, we briefly revisit the necessary modeling concepts from Chapter 2 in this section.

The  $m$ th element of the channel vector  $[\mathbf{h}(\mathbf{p}, f)]_m$  represents the channel from transmit antenna  $m \in \{1 \dots M\}$  to the UE device, equipped with a single antenna. The channel vector is modeled as the superposition of the channel vectors  $\mathbf{h}_k(\mathbf{p}, f)$  of  $K$  SMCs

$$\mathbf{h}(\mathbf{p}, f) = \sum_{k=1}^K \mathbf{h}_k(\mathbf{p}, f). \quad (5.1)$$

Each SMC  $k \in \{1 \dots K\}$  (including the LOS with  $k = 1$ ) is modeled by means of an image or mirror source, obtained by mirroring all  $M$  transmit antennas across the surface and computing

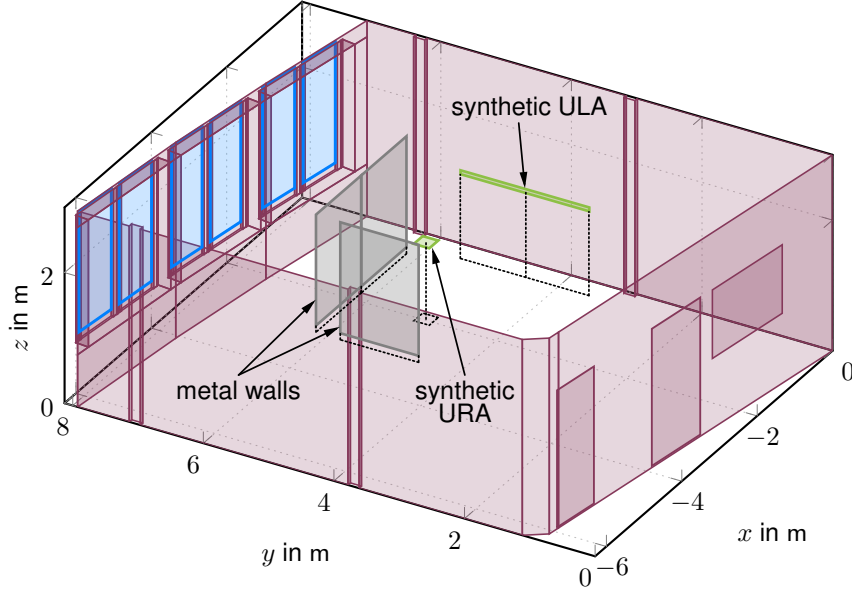


Figure 5.1: A three-dimensional (3D) model of the measurement scenario: Bistatic synchronization anchor (SA) measurements are conducted using one  $\frac{\lambda}{2}$ -ULA mounted on a wall and a  $\frac{\lambda}{4}$ -URA in the horizontal plane at  $f_c = 3.79$  GHz. Metal walls have been placed in the environment to introduce controlled specular reflections.

the corresponding distances from the position of the  $k^{\text{th}}$  mirror source at position  $\mathbf{p}_k$  to the energy neutral (EN) device position  $\mathbf{p}$ . For simplicity, we only model first-order specular reflections. The computation of the mirror sources is described in the appendix of [34]. The elements of each SMC channel vector are accordingly modeled as [35]

$$[\mathbf{h}_k(\mathbf{p}, f)]_m = \sqrt{G_{t,m}} \sqrt{G_r} \frac{\lambda}{4\pi \|\mathbf{r}_{k,m}\|} e^{-j\frac{2\pi}{\lambda} \|\mathbf{r}_{k,m}\|} \quad (5.2)$$

which represents the Friis transmission equation formulated for power wave amplitudes.  $G_{t,m}(\theta, \varphi)$  and  $G_r(\theta, \varphi)$  are the gain patterns of the respective antennas in azimuth and elevation direction  $(\theta, \varphi)$  of an incident wave in local spherical antenna coordinates, and  $\mathbf{r}_{k,m} = \mathbf{p} - \mathbf{p}_{k,m}$  is the vector from transmit antenna  $m$  of mirror source  $k$  at  $\mathbf{p}_{k,m}$  to the EN device position  $\mathbf{p}$ .

When transmitting with a total power  $P_t$ , the EN device receives complex baseband amplitude, i.e., a phasor,

$$\alpha(\mathbf{p}, f, \mathbf{w}) = \mathbf{h}^\top(\mathbf{p}, f) \mathbf{w} \sqrt{P_t} \quad (5.3)$$

where  $\mathbf{w} \in \mathbb{C}^{M \times 1}$  is a unit-vector of beamforming weights, i.e.,  $\|\mathbf{w}\| = 1$ . The efficiency of power transmission is represented by the path gain

$$PG(\mathbf{p}, f, \mathbf{w}) = \frac{P_r}{P_t} = \frac{|\alpha(\mathbf{p}, f, \mathbf{w})|^2}{P_t} \quad (5.4)$$

defined through the ratio of received power  $P_r$  to transmit power. We assume  $P_t = 1$  W for the remainder of this section.

### 5.1.2 Radar Imaging

We employ the radar imaging scheme proposed in [36], computing a reflectivity map

$$I(\mathbf{p}) = \sum_{i=1}^{N_f} \mathbf{w}_r^\top(\mathbf{p}, f_i) \mathbf{H}(f_i) \mathbf{w}_t(\mathbf{p}, f_i) \quad (5.5)$$

for every point  $\mathbf{p}$  in a specified two-dimensional (2D) spatial window of interest aligned with the height of the ULA. An important aspect is the straightforward adaption of (5.5) to a MIMO setup (i.e., using multiple CSPs or multiple UEs) or SIMO scenarios (i.e., using a single CSP and a single UE), simply by choosing a suitable dimension of the transmit (or receive) beamforming weights  $\mathbf{w}_r(\mathbf{p}, f_i)$  or  $\mathbf{w}_t(\mathbf{p}, f_i)$ .

The weight vectors for position-based beamforming  $\mathbf{w}_r(\mathbf{p}, f_i)$  and  $\mathbf{w}_t(\mathbf{p}, f_i)$ , for the receiving ULA and the transmitting URA, respectively, are computed by applying maximum ratio transmission (MRT), i.e.,

$$\mathbf{w}_r(\mathbf{p}, f) = \frac{\mathbf{h}_r^*(\mathbf{p}, f)}{\|\mathbf{h}_r(\mathbf{p}, f)\|} \quad \text{and} \quad \mathbf{w}_t(\mathbf{p}, f) = \frac{\mathbf{h}_t^*(\mathbf{p}, f)}{\|\mathbf{h}_t(\mathbf{p}, f)\|} \quad (5.6)$$

where the channel vectors  $\mathbf{h}_r(\mathbf{p}, f) \in \mathbb{C}^M$  and  $\mathbf{h}_t(\mathbf{p}, f) \in \mathbb{C}^N$  are given by (5.2), assuming isotropic gain patterns for simplicity and  $K = 1$ , i.e., LOS beamforming only. The definition in (5.2) inherently performs spherical wavefront beamforming (cf., [37, 38, 34]). Fig. 5.2 shows the imaging results we obtain by evaluating (5.5) for a grid of positions  $\mathbf{p}$  in the measurement scenario (see Fig. 5.1).

Note that  $|I(\mathbf{p})|^2$  is a measure of the power received by the ULA from position  $\mathbf{p}$  when simultaneously beamforming to the position  $\mathbf{p}$  with the URA, and coherently summing over the whole frequency band of 3-10 GHz. There is a peak visible in the LOS path between the two arrays that exhibits *smooth* edges. The power decreases in the vicinity of the URA because it is vertically located 10 cm below the evaluated window. The radar image shows *sharp* edges at the locations of the metal walls (i.e., the specularly reflecting surfaces) and a gradually decaying power “behind” the walls.

### 5.1.3 Edge Detection and Surface Estimation

The sharp edges in the radar image are well-suited for an edge detection algorithm. We run the Canny edge detector [39, Sec. 2.4] on the radar image and subsequently employ the Hough transform [39, p. 342 ff.] to transform the image into the Hough space. The peaks of the resulting Hough image are used to find the location, orientation, and extent of the detected edges. Both are well-established methods in image processing. We use the MATLAB<sup>®</sup> implementations of the Canny edge detector and Hough transform, with the chosen parameters given in [32]. Depending on the system setup, other methods may provide better estimates. The detected lines (dashed) are indicated in Fig. 5.2 alongside the resulting mirror sources (dotted). It is clearly visible that the main portion of power is concentrated at the intersection of the path between mirror sources of the ULA and the URA and thus the radar image does not capture the full extent of the walls.

However, the physically large extent of our ULA w.r.t. the propagation distances of interest covers a reasonably large portion of the walls in the resulting radar image in Fig. 5.2. This is a feature of the sub-10 GHz operating frequency range which allows to form physically large apertures.

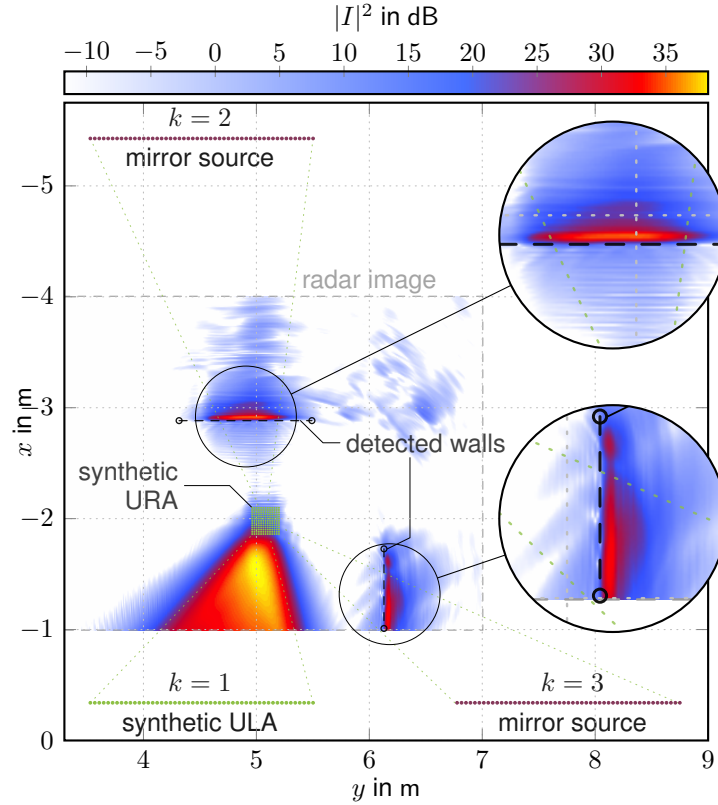


Figure 5.2: The obtained bistatic MIMO radar image shows the received power of the imaging method (see Section 5.1.2) with the positions of walls estimated through the methods described in Section 5.1.3. The corresponding positions of mirror sources  $k \in \{2, 3\}$  have been computed by mirroring the synthetic ULA ( $k = 1$ ) across the walls.

### 5.1.4 Synthetic Aperture Measurements

We employ the SA measurement testbed described in D1.2 [2] with two mechanical positioners to measure the channel vector elements  $[\mathbf{h}(\mathbf{p}_n, f)]_m$  between antenna  $m$  of a synthetic ULA and antenna  $n \in \{1 \dots N\}$  of a synthetic URA. The ULA and URA together form a MIMO system, with the MIMO channel matrix  $\mathbf{H}(f) = [\mathbf{h}(\mathbf{p}_1, f) \dots \mathbf{h}(\mathbf{p}_N, f)] \in \mathbb{C}^{M \times N}$  obtained by stacking the  $N$  MISO channel vectors for each receive antenna  $n$ . The scenario is illustrated in Fig. 5.1, where the URA is located between metal walls that generate strong SMCs.

We use a Rohde & Schwarz ZVA24 vector network analyzer (VNA) in a two-port configuration to measure the transmission coefficient  $S_{21}(f)$  between a transmit antenna  $m$  connected to Port 1 and a receiving antenna  $n$  connected to Port 2 (see [2] for a description of the measurement system). We measure at  $N_f = 1000$  linearly spaced frequencies  $f_i$  in a frequency band of spanning 3 – 10 GHz.

## 5.2 Application Examples

This section shows possibilities that arise when environment information is available, we give application examples and briefly outline the achievable performance gain. Examples include general geometry-based based beamforming towards a specific location, and the corresponding extension to increase the power received there, the exploitation of frequency diversity and multipath-based positioning.

### 5.2.1 Geometry-based Beamforming

In the following, instead of a URA we assume that a single-antenna UE device is placed at a location  $\mathbf{p}_{\text{ue}}$ , using the collected measurement data briefly discussed in Section 5.1.4 in a MISO configuration. We aim to transmit power to the UE device solely based on the assumed known geometric location of the UE device and the inferred locations of the  $K = 3$  sources, i.e., mirror sources and the LOS. We use a geometry-based beamformer at the chosen frequency of  $f_c = 3.79$  GHz and compute beamforming weights using MRT as

$$\mathbf{w} = \sum_{k=1}^K \mathbf{w}_k \quad \text{with} \quad \mathbf{w}_k = \frac{\tilde{\mathbf{h}}_k^*(\mathbf{p}_{\text{ue}}, f_c)}{\|\tilde{\mathbf{h}}(\mathbf{p}_{\text{ue}}, f_c)\|} \quad (5.7)$$

where the predicted channel vector  $\tilde{\mathbf{h}}(\mathbf{p}_{\text{ue}}, f_c)$  is the superposition of the  $K = 3$  predicted SMC channel vectors  $\tilde{\mathbf{h}}_k(\mathbf{p}_{\text{ue}}, f_c)$ , computed using (5.2) and the estimated mirror source locations. We can compute the phasors for each SMC  $k$  using (5.3)

$$\hat{\alpha}_k = \mathbf{h}^\top \mathbf{w}_k \sqrt{P_t} \quad (5.8)$$

using the assumed “true” (measured) channel vector  $\mathbf{h}$  to quantify the contribution of each mirror source on the sum-phasor  $\hat{\alpha} = \sum_{k=1}^K \hat{\alpha}_k$  received by the UE, e.g., considering it to be an END that needs to be supplied with power. Note that the channel vectors  $\mathbf{h}_k$  are not independent and thus the computed phasors  $\hat{\alpha}_k$  only approximate the amplitudes of the  $k$ th SMC. Fig. 5.3a shows that the SMC phasors  $\hat{\alpha}_2$  and  $\hat{\alpha}_3$  are not well aligned with the LOS phasor  $\hat{\alpha}_1$  as a result of uncertainty in the estimated mirror source locations. The SMC beams interfere destructively at the UE, resulting in a path gain  $PG \approx -35.3$  dB when using predicted weights in (5.7).

### 5.2.2 Beam Phase Optimization for WPT

To compensate for geometric uncertainties in the environment model, we employ an optimization of SMC beam phases that we proposed in [34, eq. (14)]. The objective is to find optimal phase shifts  $\tilde{\varphi}_k$  applied to the weights  $\mathbf{w}_k$  such that the path gain at the EN device is maximized. Note that the number of beam phases to be optimized is  $K - 1$ , i.e., the phase of one beam (e.g., the LOS beam) can be kept constant and all other beam phases are optimized. Fig. 5.3b shows the corresponding optimized phasors  $\tilde{\alpha}_k$ . After the optimization, the EN device receives a sum-phasor that translates to a path gain  $PG \approx -28.3$  dB using our predicted CSI, which gets reasonably close to the maximum path gain  $PG_{\text{MAX}} \approx -27.2$  dB achievable with full CSI. Fig. 5.4a shows the  $PG$  distribution evaluated across the aperture of the URA given the optimized beamforming weights  $\tilde{\mathbf{w}}$ .

A strong standing wave pattern is visible in Fig. 5.4a, originating from the wall *behind* the EN device, i.e., mirror sources  $k = 2$  and  $k = 1$  being located on opposite sides of the EN device.

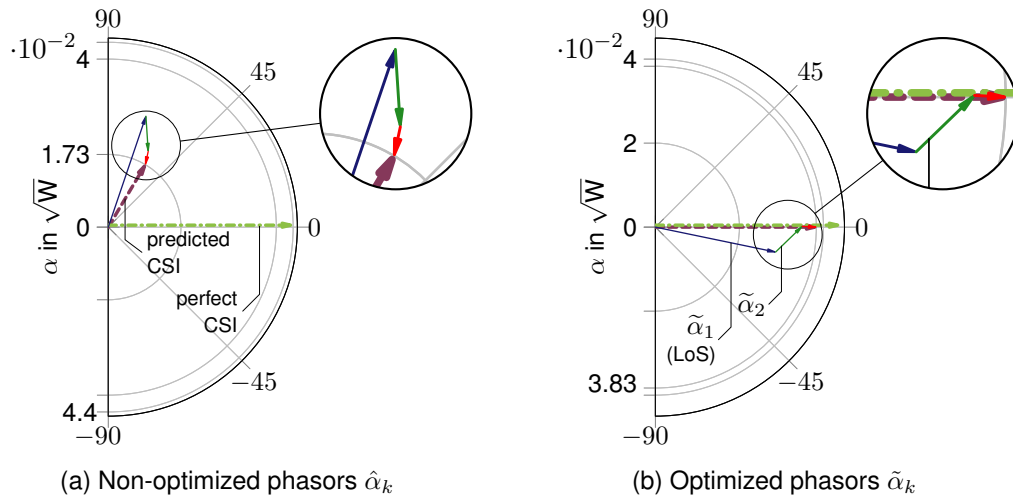


Figure 5.3: Phasors  $\alpha_k$  in the complex polar plane computed on the “true” (measured) channel vector  $\mathbf{h}$  (dash-dotted) with beamforming weights generated from the predicted SMC channel vectors  $\tilde{\mathbf{h}}_k$  (solid) and  $P_t = 1$  W. The phase optimization in Section 5.2.2 aligns the phases of SMC beams in the complex plane and thus maximizes the sum-phasor (dashed) received by the UE device.

This is a particular problem of performing WPT in indoor environments as we have demonstrated in [3].

Fig. 5.4b shows the resulting  $PG$  distribution when using the mirror source  $k = 3$  only, revealing how the geometric model uncertainty impacts the location of the resulting SMC beam. At the same time, it confirms that the reflection from the corresponding metal wall is reasonably specular as our SMC channel model results in a clearly visible beam originating from the location of the third mirror source  $k = 3$ .

### 5.2.3 Dual-band Operation

The distributed radio infrastructures of RW may not have a large frequency band of 3 GHz to 10 GHz available. However, a dual-band operation may be a suitable alternative to provide sufficient imaging results for inferring walls. To test the performance of a dual-band operation, we restrict the measured bandwidth to a 100 MHz band centered around 3.79 GHz and a 1.2 GHz band centered at 6.5 GHz (a frequency band designated for Wi-Fi 6E in the U.S., South Korea, Brazil, and Canada [40]) and repeat the imaging procedure. The resulting radar image is shown in Fig. 5.5. As can be observed from the figure, walls are inferred at “ripples” in the radar image at some distance from the previously estimated locations given the full bandwidth. However, Fig. 5.6 shows that the phase-optimization method still attains a reasonable efficiency of  $PG \approx -28.2$  dB for wireless power transfer. More sophisticated schemes may be better able to estimate wall locations and provide better results.

The dual-band operation performs worse in inferring the walls (see Fig. 5.5) but still showed a reasonable performance for the given application of WPT. Thus it may be a suitable approach for future distributed radio infrastructures, especially when being used with more elaborate estimation schemes.

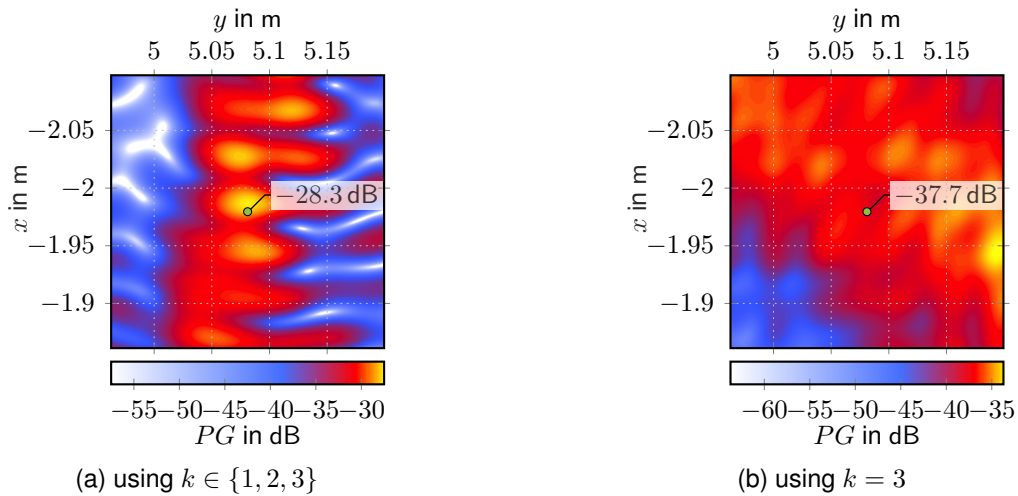


Figure 5.4: Measured  $PG$  distribution across the synthetic URA (interpolated) when applying geometry-based beamforming: Channel vectors  $\mathbf{h}_k$  are predicted using the estimated geometric environment information from Fig. 5.2.

## 5.2.4 Multipath-based positioning

Multipath-assisted or multipath-based positioning is one key application field where environment information can be exploited. Assuming that an environment model is available, e.g., estimated as described in Section 5.1.2, or as in [41, 4, 42], improvements regarding accuracy as well as robustness are expected for positioning approaches and model-based beamforming for communication and WPT are expected. The use of mirror sources as what are commonly termed virtual anchors, i.e., additional virtual CSPs, can be especially useful in NLOS scenarios where the direct path link is blocked, either by walls in the environment or by moving objects or the user itself, allowing to keep a limited-quality link available. These approaches can work directly on the information provided by the graph-based channel data fusion approach applied to subarrays, outlined in Section 4.2.

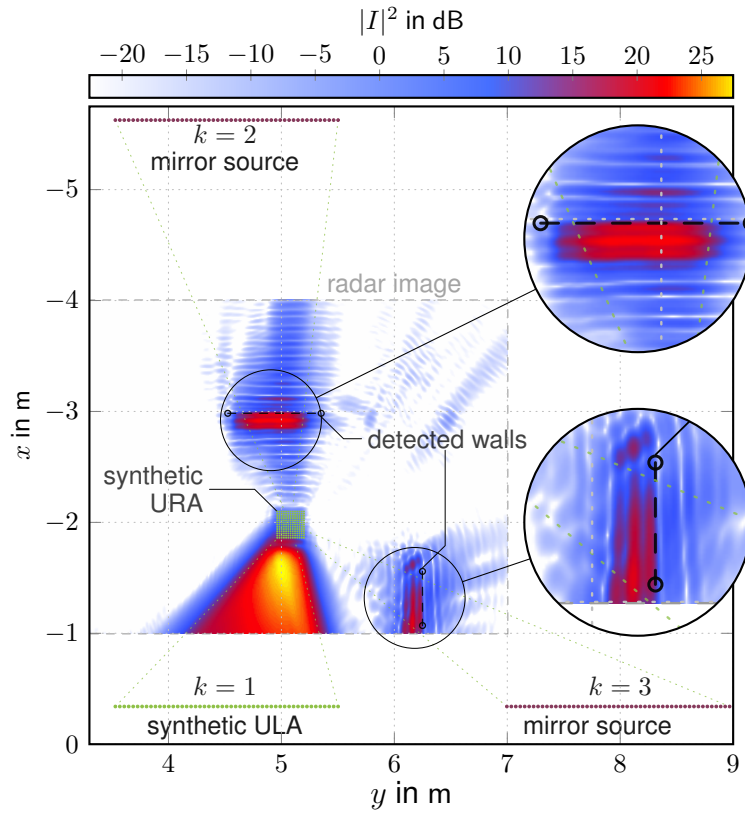


Figure 5.5: The obtained bistatic MIMO radar image generated with the dual-band operation. The walls are inferred at “ripples” in the radar image at some distance from the locations that would be estimated using the full bandwidth (see Fig. 5.2).

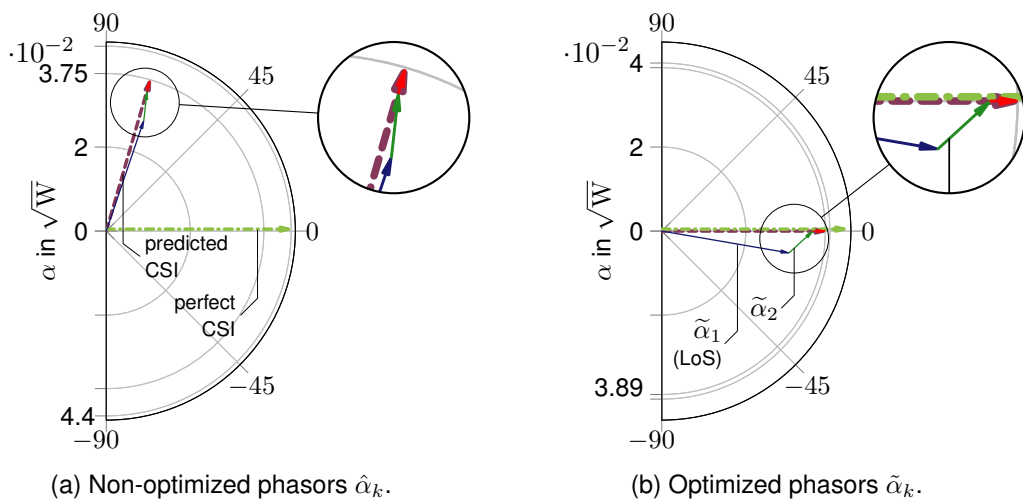


Figure 5.6: Phasors  $\alpha_k$  in the complex polar plane generated with the dual-band operation. A reasonable efficiency of  $PG \approx -28.2$  dB is attained after the phase optimization in Section 5.2.2, despite deviations in the estimated wall locations.

# Chapter 6

## Summary

This deliverable presents the results of algorithms for positioning-related applications, synchronization and distributed calibration as well as environment learning. The algorithms are investigated in the context of the RadioWeaves (RW) infrastructure, with the focus being on the algorithm performance, the system level performance and the system parameter dependency or system layout. The covered topics are the positioning and synchronization performance of an exemplary RW infrastructure. To this end we analyze the positioning performance by applying an extended Kalman filter (EKF)-based algorithm, allowing to track a mobile user equipment (UE) as well as system synchronization parameters, a system calibration method to enable reciprocity-based communication and dedicated positioning algorithms, distributed channel estimation in a graph-based algorithm, and environment learning exploiting the large aperture of the RW infrastructure.

We derive the fundamental performance limits for joint positioning and synchronization in a system consisting of Contact Service Points (CSPs) equipped with large arrays. To achieve the necessary system flexibility we investigate the performance in a subarray-based setup, as it combines advantages of compact arrays (avoiding spatial aliasing) and widely distributed arrays (diversity and favourable geometric dilution of precision). We show that the distribution of small subarrays with increased spacing leads to a favorable performance in position estimation in indoor environments experiencing diffuse multipath propagation. In addition, the performance loss in the bandwidth region of interest, that is introduced when performing joint positioning and synchronization, can be overcome by selecting suitable CSP position layouts, even when the size of the subarrays is small. On the other hand, this small subarray was shown to suffer from a performance degradation when the UE moves farther away from a specific CSP, which is a well known effect attributable to the fact that the contribution of angle-information to the overall positioning accuracy rapidly decreases with increasing distance. With the distributed, user-centric architecture, this effect is expected to be countered. Additionally, this effect favors the design of federations, by allowing to provide additional input to the formation process, e.g., in terms of metrics for the achievable positioning performance.

In the graph-based algorithm is investigated, we have shown that it is possible to deal with multipath environments, taking the non-stationarity of multipath components (MPCs) is actively into account. The algorithm shows promising results as it allows to track even low-signal-to-noise ratio (SNR) MPCs, which can be important in non-line-of-sight (NLOS) conditions and generally "noisy", and multipath or interference-rich environments. Furthermore, the algorithm also allows to obtain additional information in terms of the visibility of MPCs as outlined in the channel model

discussed in D1.2 [2], which can again serve as input to, e.g., the federation formation.

As a next step from the graph-based algorithm, we investigate an EKF-based algorithm for positioning. The EKF-based algorithm is able to cope with clock offset between a large number of CSPs and performs joint positioning and synchronization. The performance was analyzed with simulated data for different levels of measurement accuracy, showing the trade-off between angle and range accuracy. As it was shown to be possible to additionally track the clock drift, e.g., considering time varying clock offsets, additional information could be provided to synchronization algorithms should this be deemed necessary, e.g., by triggering a re-synchronization algorithm when at times decided upon due to the "speed" of the drift. While not yet fully investigated at this stage, the possibility to include environment information that can be fed back to algorithms to improve the robustness, e.g., in NLOS scenarios, is anticipated.

Maximum ratio transmission (MRT) schemes are known to yield high performance while requiring reciprocity calibration of the transceiver frontends, which is not always given. For this reason, a reciprocity calibration approach is investigated which enables to perform coherent communication in distributed multiple-input multiple-output (MIMO) systems. The proposed calibration approach is beneficial for all transceiver functions that require accurate channel state information, i.e. for communication, positioning, environment estimation, and wireless power transfer. In general, distributed MIMO represents an instantiation of the RW infrastructure consisting of distributed CSPs communicating with multiple UEs.

Environment sensing provides important information for algorithms that can exploit parametric environment information, for example when performing multipath-based positioning or position-based beamforming, where multipath components are used to improve positioning accuracy, or the amount of transmitted power or data. Especially in the MIMO radar approach discussed in this report, the large expected aperture of the distributed RW infrastructure will allow for a high accuracy imaging.

The algorithms presented in this deliverable have shown to be sufficiently flexible to allow application to the diverse use cases treated by the RW infrastructure. While environment learning has already been applied to real measurements, the testing of algorithms based on simulations allows to efficiently analyze performance under controlled conditions. The next step is algorithm testing based on the extensive set of measurement data collected in various environments and system configurations, e.g., in the course of the channel modeling work in D1.2 [2], with a selection of the measurement data presented there. Furthermore synergies between the algorithms will be leveraged, for instance using the channel parameter estimation algorithms to extract parametric channel models for model-based wireless power transfer.

In conclusion, a strong feature of RW is the envisioned wide distribution, allowing to exploit the large overall system aperture for positioning, but also position-*awareness* in other applications. As a direct result, a sufficiently high performance in terms of positioning accuracy is anticipated. Another key feature is the targeted system flexibility, allowing to obtain scalable algorithms. A subarray-based estimation of position-related parameters is expected to, on the one hand, improve the distribution of computational resources, but also to enable targeting a reduction of the power consumption by incorporating position information alongside environment information that is kept up to date constantly after the RW is set up.

## Appendix A

# Fisher Information Matrix for Channel Parameters

The elements of the Fisher information matrix (FIM)  $\mathbf{J}_{\text{ch}}^{(j)}$  in (3.11) are obtained by evaluating [15, Sec. 15.7]. Due to symmetry,  $[\mathbf{J}_{\text{ch}}^{(j)}]_{mn} = [\mathbf{J}_{\text{ch}}^{(j)}]_{nm}$  holds. For readability we will drop the CSP/subarray index  $j$  and denote  $\mathbf{x}(\boldsymbol{\theta}) = \mathbf{x}(\varphi, \vartheta, \tau) = [(\mathbf{x}_1(\varphi, \vartheta, \tau))^T, \dots, (\mathbf{x}_M(\varphi, \vartheta, \tau))^T]^T$ . At the example of the FIM elements for the azimuth angle, one can show that

$$[\mathbf{J}_{\text{ch}}]_{\varphi\varphi} = 2\mathbb{R} \left[ \alpha^2 \frac{\partial \mathbf{x}(\varphi, \vartheta, \tau)^H}{\partial \varphi} \mathbf{C}^{-1} \frac{\partial \mathbf{x}(\varphi, \vartheta, \tau)}{\partial \varphi} \right] \quad (\text{A.1})$$

$$= 2\mathbb{R} \left[ \alpha^2 \sum_m \frac{\partial \mathbf{x}_m(\varphi, \vartheta, \tau)^H}{\partial \varphi} \mathbf{C}_m^{-1} \frac{\partial \mathbf{x}_m(\varphi, \vartheta, \tau)}{\partial \varphi} \right] \quad (\text{A.2})$$

due to the independence assumptions between different array elements. From this it is furthermore possible to show that when choosing the array reference position as the center of gravity, all FIM entries containing one derivative w.r.t. azimuth or elevation and the other *not* w.r.t. azimuth or elevation will be come zero as this reference point selection will result in

$$\sum_m \frac{\partial \mathbf{g}_m(\varphi, \vartheta)}{\partial \varphi} = -i2\pi \mathbf{f} \left( \sum_m \frac{\partial \mathbf{u}(\varphi, \vartheta)^T}{\partial \varphi} \mathbf{a}_m \mathbf{g}_m(\varphi, \vartheta) \right) = 0 \quad (\text{A.3})$$

to vanish. The remaining FIM elements of the position-related as well as nuisance parameters are found to be

$$[\mathbf{J}_{\text{ch}}]_{\varphi\vartheta} = 2\mathbb{R} \left[ \alpha^2 \frac{\partial \mathbf{x}(\varphi, \vartheta, \tau)^H}{\partial \varphi} \mathbf{C}^{-1} \frac{\partial \mathbf{x}(\varphi, \vartheta, \tau)}{\partial \vartheta} \right] \quad (\text{A.4})$$

$$[\mathbf{J}_{\text{ch}}]_{\varphi\tau} = 2\mathbb{R} \left[ \alpha^2 \frac{\partial \mathbf{x}(\varphi, \vartheta, \tau)^H}{\partial \varphi} \mathbf{C}^{-1} \frac{\partial \mathbf{x}(\varphi, \vartheta, \tau)}{\partial \tau} \right] \stackrel{(\text{A.3})}{=} 0 \quad (\text{A.5})$$

$$[\mathbf{J}_{\text{ch}}]_{\vartheta\vartheta} = 2\mathbb{R} \left[ \alpha^2 \frac{\partial \mathbf{x}(\varphi, \vartheta, \tau)^H}{\partial \vartheta} \mathbf{C}^{-1} \frac{\partial \mathbf{x}(\varphi, \vartheta, \tau)}{\partial \vartheta} \right] \quad (\text{A.6})$$

$$[\mathbf{J}_{\text{ch}}]_{\vartheta\tau} = 2\mathbb{R} \left[ \alpha^2 \frac{\partial \mathbf{x}(\varphi, \vartheta, \tau)^H}{\partial \vartheta} \mathbf{C}^{-1} \frac{\partial \mathbf{x}(\varphi, \vartheta, \tau)}{\partial \tau} \right] \stackrel{(\text{A.3})}{=} 0 \quad (\text{A.7})$$

$$[\mathbf{J}_{\text{ch}}]_{\tau\tau} = 2\mathbb{R} \left[ \alpha^2 \frac{\partial \mathbf{x}(\varphi, \vartheta, \tau)^{\text{H}}}{\partial \tau} \mathbf{C}^{-1} \frac{\partial \mathbf{x}(\varphi, \vartheta, \tau)}{\partial \tau} \right] \quad (\text{A.8})$$

$$[\mathbf{J}_{\text{ch}}]_{\varphi\varphi} = 2\mathbb{R} \left[ \alpha^2 \frac{\partial \mathbf{x}(\varphi, \vartheta, \tau)^{\text{H}}}{\partial \varphi} \mathbf{C}^{-1} \frac{\partial \mathbf{x}(\varphi, \vartheta, \tau)}{\partial \varphi} \right] \quad (\text{A.9})$$

$$[\mathbf{J}_{\text{ch}}]_{\varphi\alpha} = 2\mathbb{R} \left[ \alpha \frac{\partial \mathbf{x}(\varphi, \vartheta, \tau)^{\text{H}}}{\partial \varphi} \mathbf{C}^{-1} \mathbf{x}(\varphi, \vartheta, \tau) \right] \stackrel{(\text{A.3})}{=} 0 \quad (\text{A.10})$$

$$[\mathbf{J}_{\text{ch}}]_{\varphi\tau} = 2\mathbb{R} \left[ \alpha^2 \frac{\partial \mathbf{x}(\varphi, \vartheta, \tau)^{\text{H}}}{\partial \varphi} \mathbf{C}^{-1} \frac{\partial \mathbf{x}(\varphi, \vartheta, \tau)}{\partial \tau} \right] \stackrel{(\text{A.3})}{=} 0 \quad (\text{A.11})$$

$$[\mathbf{J}_{\text{ch}}]_{\vartheta\vartheta} = 2\mathbb{R} \left[ \alpha^2 \frac{\partial \mathbf{x}(\varphi, \vartheta, \tau)^{\text{H}}}{\partial \vartheta} \mathbf{C}^{-1} \frac{\partial \mathbf{x}(\varphi, \vartheta, \tau)}{\partial \vartheta} \right] \quad (\text{A.12})$$

$$[\mathbf{J}_{\text{ch}}]_{\vartheta\alpha} = 2\mathbb{R} \left[ \alpha \frac{\partial \mathbf{x}(\varphi, \vartheta, \tau)^{\text{H}}}{\partial \vartheta} \mathbf{C}^{-1} \mathbf{x}(\varphi, \vartheta, \tau) \right] \stackrel{(\text{A.3})}{=} 0 \quad (\text{A.13})$$

$$[\mathbf{J}_{\text{ch}}]_{\tau\alpha} = 2\mathbb{R} \left[ \alpha^2 \frac{\partial \mathbf{x}(\varphi, \vartheta, \tau)^{\text{H}}}{\partial \tau} \mathbf{C}^{-1} \frac{\partial \mathbf{x}(\varphi, \vartheta, \tau)}{\partial \tau} \right] \quad (\text{A.14})$$

$$[\mathbf{J}_{\text{ch}}]_{\phi\phi} = 2\mathbb{R} \left[ \alpha^2 \mathbf{x}(\varphi, \vartheta, \tau)^{\text{H}} \mathbf{C}^{-1} \mathbf{x}(\varphi, \vartheta, \tau) \right] \quad (\text{A.15})$$

$$[\mathbf{J}_{\text{ch}}]_{\alpha\alpha} = 2\mathbb{R} \left[ \mathbf{x}(\varphi, \vartheta, \tau)^{\text{H}} \mathbf{C}^{-1} \mathbf{x}(\varphi, \vartheta, \tau) \right]. \quad (\text{A.16})$$

The corresponding derivatives of the separate steering vectors contained in  $\mathbf{x}(\boldsymbol{\theta})$  and consequently  $\mathbf{x}_m(\varphi, \vartheta, \tau)$  are given as

$$\frac{\partial \mathbf{g}_m(\varphi, \vartheta)}{\partial \varphi} = -i2\pi \mathbf{f} \left( \frac{\partial \mathbf{u}(\varphi, \vartheta)^{\text{T}}}{\partial \varphi} \mathbf{a}_m \right) \mathbf{g}_m(\varphi, \vartheta) \quad (\text{A.17})$$

$$\frac{\partial \mathbf{b}(\tau)}{\partial \tau} = \mathbf{f} \circ \mathbf{b}(\tau) \quad (\text{A.18})$$

with  $\mathbf{f} = [f_1, \dots, f_N]^{\text{T}}$  and with derivatives w.r.t. angles of the direction vector  $\mathbf{u}(\varphi, \vartheta)$

$$\frac{\partial \mathbf{u}(\varphi, \vartheta)}{\partial \varphi} = \sin \vartheta \mathbf{e}_{\varphi} \quad (\text{A.19})$$

$$\frac{\partial \mathbf{u}(\varphi, \vartheta)}{\partial \vartheta} = \mathbf{e}_{\vartheta} \quad (\text{A.20})$$

where  $\mathbf{e}_{\varphi}$  and  $\mathbf{e}_{\vartheta}$  are unit vectors defined as (see Figure 2.1b)

$$\mathbf{e}_r = \mathbf{u}(\varphi, \vartheta) \quad \mathbf{e}_{\vartheta} = [\cos \varphi \cos \vartheta, \sin \varphi \cos \vartheta, \sin \vartheta]^{\text{T}} \quad \mathbf{e}_{\varphi} = [-\sin \varphi, \cos \varphi, 0]^{\text{T}}.$$

## Bibliography

- [1] O. Edfors, R. Brazil, H. Petautschnig, G. Callebaut, T. Feys, L. V. der Perre, E. G. Larsson, O. Edfors, E. Fitzgerald, L. Liu, J. R. Sanchez, W. Tärneberg, P. Frenger, B. Deutschmann, T. Wilding, and K. Witrisal, "Initial assessment of architectures and hardware resources for a RadioWeaves infrastructure, Reindeer deliverable D2.1," Tech. Rep., Jan. 2022. [Online]. Available: <https://doi.org/10.5281/zenodo.5938909>
- [2] REINDEER Project, "Propagation characteristics and channel models for RadioWeaves including reflectarrays," Deliverable ICT-52-2020 / D1.2, 2023 (unpublished).
- [3] B. J. B. Deutschmann, T. Wilding, E. G. Larsson, and K. Witrisal, "Location-based initial access for wireless power transfer with physically large arrays," in *WS08 IEEE ICC 2022 Workshop on Synergies of communication, localization, and sensing towards 6G (WS08 ICC'22 Workshop - ComLS-6G)*, Seoul, Korea (South), May 2022.
- [4] E. Leitinger, P. Meissner, C. Rudisser, G. Dumphart, and K. Witrisal, "Evaluation of position-related information in multipath components for indoor positioning," *IEEE J. Sel. Areas Commun.*, vol. 33, no. 11, pp. 2313–2328, Nov. 2015.
- [5] J. F. Esteban and M. Truskaller, "Use case-driven specifications and technical requirements and initial channel model," REINDEER project, Deliverable ICT-52-2020 / D1.1, Sep 2021.
- [6] D. H. Johnson and D. E. Dudgeon, *Array signal processing: Concepts and techniques*. Simon & Schuster, Inc., 1992.
- [7] H. L. Van Trees, *Optimum Array Processing: Part IV of Detection, Estimation, and Modulation Theory*, ser. Detection, Estimation, and Modulation Theory. John Wiley & Sons, Inc., 2002.
- [8] H. Krim and M. Viberg, "Two decades of array signal processing research: The parametric approach," *IEEE Signal Process. Mag.*, vol. 13, no. 4, pp. 67–94, Jul. 1996.
- [9] Y. R. Faizulkhakov, "Time synchronization methods for wireless sensor networks: A survey," *Programming and Computer Software*, vol. 33, pp. 214–226, 2007.
- [10] M. Koivisto, M. Costa, J. Werner, K. Heiska, J. Talvitie, K. Leppänen, V. Koivunen, and M. Valkama, "Joint device positioning and clock synchronization in 5G ultra-dense networks," *IEEE Trans. Wireless Commun.*, vol. 16, no. 5, pp. 2866–2881, 2017.
- [11] A. Richter, "Estimation of Radio Channel Parameters: Models and Algorithms," Ph.D. dissertation, Ilmenau University of Technology, 2005.

- [12] J. Salmi, A. Richter, and V. Koivunen, "Detection and tracking of MIMO propagation path parameters using state-space approach," *IEEE Trans. Signal Process.*, vol. 57, no. 4, pp. 1538–1550, Apr. 2009.
- [13] A. Fascista, B. J. B. Deutschmann, M. F. Keskin, T. Wilding, A. Coluccia, K. Witrisal, E. Leitinger, G. Seco-Granados, and H. Wymeersch, "Uplink joint positioning and synchronization in cell-free deployments with radio stripes." arXiv, 2023. [Online]. Available: <https://doi.org/10.48550/arXiv.2302.03387>
- [14] T. Wilding, S. Grebien, E. Leitinger, U. Mühlmann, and K. Witrisal, "Single-anchor, multipath-assisted indoor positioning with aliased antenna arrays (invited paper)," in *2018 52nd Asilomar Conference on Signals, Systems, and Computers*, 2018, pp. 525–531.
- [15] S. M. Kay, *Fundamentals of Statistical Signal Processing: Estimation Theory*. Upper Saddle River, NJ: Prentice-Hall PTR, 1993.
- [16] A. Guerra, F. Guidi, and D. Dardari, "Single-anchor localization and orientation performance limits using massive arrays: MIMO vs. beamforming," *IEEE Trans. Wireless Commun.*, vol. 17, no. 8, pp. 5241–5255, 2018.
- [17] Y. Shen and M. Z. Win, "Fundamental limits of wideband localization—Part I: A general framework," *IEEE Trans. Inf. Theory*, vol. 56, no. 10, pp. 4956–4980, 2010.
- [18] Y. Han, Y. Shen, X.-P. Zhang, M. Z. Win, and H. Meng, "Performance limits and geometric properties of array localization," *IEEE Trans. Inf. Theory*, vol. 62, no. 2, pp. 1054–1075, 2016.
- [19] X. Li, E. Leitinger, A. Venus, and F. Tufvesson, "Sequential detection and estimation of multipath channel parameters using belief propagation," *IEEE Trans. Wireless Commun.*, vol. 21, no. 10, pp. 8385–8402, 2022.
- [20] G. Interdonato, E. Björnson, H. Quoc Ngo, P. Frenger, and E. G. Larsson, "Ubiquitous cell-free massive MIMO communications," *EURASIP Journal on Wireless Communications and Networking*, vol. 2019, no. 1, pp. 1–13, 2019.
- [21] L. Van der Perre, E. G. Larsson, F. Tufvesson, L. De Strycker, E. Björnson, and O. Edfors, "Radioweaves for efficient connectivity: analysis and impact of constraints in actual deployments," in *2019 53rd Asilomar Conference on Signals, Systems, and Computers*. IEEE, 2019, pp. 15–22.
- [22] J. Vieira, F. Rusek, O. Edfors, S. Malkowsky, L. Liu, and F. Tufvesson, "Reciprocity calibration for massive MIMO: Proposal, modeling, and validation," *IEEE Trans. Wireless Commun.*, vol. 16, no. 5, pp. 3042–3056, 2017.
- [23] R. Rogalin, O. Y. Bursalioglu, H. Papadopoulos, G. Caire, A. F. Molisch, A. Michaloliakos, V. Balan, and K. Psounis, "Scalable synchronization and reciprocity calibration for distributed multiuser MIMO," *IEEE Trans. Wireless Commun.*, vol. 13, no. 4, pp. 1815–1831, 2014.
- [24] J. Vieira and E. G. Larsson, "Reciprocity calibration of distributed massive MIMO access points for coherent operation," in *2021 IEEE 32nd Annual International Symposium on Personal, Indoor and Mobile Radio Communications (PIMRC)*, 2021, pp. 783–787.
- [25] C. Nelson, X. Li, T. Wilding, B. J. B. Deutschmann, K. Witrisal, and F. Tufvesson, "Large intelligent surface measurements for joint communication and sensing." arXiv, 2023. [Online]. Available: <https://doi.org/10.48550/arXiv.2304.12457>

- [26] T. Wilding, B. J. B. Deutschmann, C. Nelson, X. Li, F. Tufvesson, and K. Witrissal, "Propagation modeling for physically large arrays: Measurements and multipath component visibility." arXiv, 2023. [Online]. Available: <https://doi.org/10.48550/arXiv.2305.05958>
- [27] D. Schuhmacher, B.-T. Vo, and B.-N. Vo, "A consistent metric for performance evaluation of multi-object filters," *IEEE Trans. Signal Process.*, vol. 56, no. 8, pp. 3447–3457, Aug. 2008.
- [28] M. Koivisto, M. Costa, J. Werner, K. Heiska, J. Talvitie, K. Leppanen, V. Koivunen, and M. Valkama, "Joint Device Positioning and Clock Synchronization in 5G Ultra-Dense Networks," *IEEE Trans. Wireless Commun.*, vol. 16, no. 5, pp. 2866–2881, May 2017.
- [29] M. Koivisto, J. Talvitie, M. Costa, K. Leppanen, and M. Valkama, "Joint cmWave-based multiuser positioning and network synchronization in dense 5G networks," in *2018 IEEE Wireless Communications and Networking Conference (WCNC)*. Barcelona: IEEE, Apr. 2018, pp. 1–6.
- [30] D. Simon, *Optimal state estimation: Kalman, H [infinity] and nonlinear approaches*. Hoboken, N.J.: Wiley-Interscience, 2006, oCLC: ocm64084871.
- [31] B. J. B. Deutschmann, M. Graber, T. Wilding, and K. Witrissal, "Bistatic MIMO radar sensing of specularly reflecting surfaces for wireless power transfer." arXiv, 2023. [Online]. Available: <https://doi.org/10.48550/arXiv.2305.05002>
- [32] —, "Bistatic MIMO radar sensing," <https://gitlab.com/baenshy/bistatic-mimo-radar-sensing>, 2023. [Online]. Available: <https://gitlab.com/baenshy/bistatic-mimo-radar-sensing>
- [33] —, "Bistatic MIMO radar sensing of specularly reflecting surfaces for wireless power transfer," 2023. [Online]. Available: <https://dx.doi.org/10.21227/pagk-a077>
- [34] B. J. B. Deutschmann, T. Wilding, M. Graber, and K. Witrissal, "XL-MIMO channel modeling and prediction for wireless power transfer." arXiv, 2023. [Online]. Available: <https://arxiv.org/abs/2302.11969>
- [35] C. Buyle, B. Cox, D. Delabie, B. Deutschmann, T. Wilding, M. Graber, K. Witrissal, and U. Mühlmann, "System design study for energy-neutral devices interacting with the RadioWeaves infrastructure," REINDEER project, Deliverable ICT-52-2020 / D4.1, 2022.
- [36] T. Spreng, U. Prechtel, B. Schönlinner, V. Ziegler, A. Meusling, and U. Siart, "UWB near-field MIMO radar: Calibration, measurements and image reconstruction," in *European Radar Conference*, 2013, pp. 33–36.
- [37] P. Vouras, M. K. Hany, S. Perera, C. Nogueira, R. Candell, and K. A. Remley, "Wideband synthetic aperture test bed for intelligent reflecting surfaces," in *2022 56th Asilomar Conference on Signals, Systems, and Computers*, 2022, pp. 785–789.
- [38] M. Aladsani, A. Alkhateeb, and G. C. Trichopoulos, "Leveraging mmWave imaging and communications for simultaneous localization and mapping," in *ICASSP 2019 - IEEE International Conference on Acoustics, Speech and Signal Processing (ICASSP)*, 2019, pp. 4539–4543.
- [39] J. R. Parker, *Algorithms for Image Processing and Computer Vision*, 2nd ed. Indianapolis: Wiley Publishing, 2010.
- [40] M. Mehrnoush, C. Hu, and C. Aldana, "AR/VR spectrum requirement for Wi-Fi 6E and beyond," *IEEE Access*, vol. 10, pp. 133 016–133 026, 2022.

- [41] P. Meissner, "Multipath-Assisted Indoor Positioning," Ph.D. dissertation, Graz University of Technology, Oct. 2014.
- [42] A. Kakkavas, H. Wymeersch, G. Seco-Granados, M. H. C. García, R. A. Stirling-Gallacher, and J. A. Nossek, "Power allocation and parameter estimation for multipath-based 5G positioning," *IEEE Trans. Wireless Commun.*, vol. 20, no. 11, pp. 7302–7316, 2021.